Non-Isothermal Sloshing for Space Applications

Experimental Characterisation

Francisco Manuel Fernandes Monteiro

Dissertação para obtenção do Grau de Mestre em

Engenharia Aeronáutica

(mestrado integrado)

Orientador: Prof. Doutor André Resende Rodrigues da Silva

Co-orientador: Prof. Doutor Miguel Alfonso Mendez

Janeiro de 2023

Non-Isothermal Sloshing for Space Applications

Declaração de Integridade

Eu, Francisco Manuel Fernandes Monteiro, que abaixo assino, estudante com o número de inscrição 39264 do Mestrado Integrado em Engenharia Aeronáutica da Faculdade de Engenharia, declaro ter desenvolvido o presente trabalho e elaborado o presente texto em total consonância com o **Código de Integridades da Universidade da Beira Interior**.

Mais concretamente afirmo não ter incorrido em qualquer das variedades de Fraude Académica, e que aqui declaro conhecer, que em particular atendi à exigida referenciação de frases, extratos, imagens e outras formas de trabalho intelectual, e assumindo assim na íntegra as responsabilidades da autoria.

Universidade da Beira Interior, Covilhã 30/12/2022

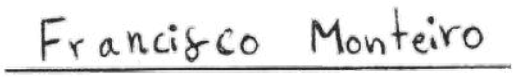

Dedicatória

Dedico esta tese de mestrado à minha família, pela sua incansável crença e incessante apoio. Um sentimento de gratidão aos meus queridos pais, à minha avó, ao meu irmão e namorada pelas palavras de encorajamento e de tenacidade nos bons e maus momentos, desta longa caminhada.

"*It's not about where you come from, it's about heart*."

Agradecimentos

A parte final desta caminhada que compreendeu os últimos cinco anos não poderia deixar de ficar definida como um dos períodos mais desafiadores da minha vida. Foram seis meses fantásticos de superação, acompanhado de mentes brilhantes que em tudo contribuíram para o sucesso deste projeto. Contudo, não poderia de deixar de começar por agradecer a todos os que caminharam comigo desde o primeiro dia deste trajeto.

Em primeiro lugar ao meu pai, mãe, avó e irmão os grandes impulsionadores desta jornada. Pelo seu incessante apoio e paciência nos momentos de derrota e vitória. Onde na distância encontrámos modos de nos superar, lutar e unir. Carrego comigo o vosso sonho para o resto da vida. Muito obrigado.

Um obrigado à minha namorada que comigo caminhou ao longo destes anos desafiadores. Pela sua crença, confiança e acima de tudo por estar presente nos momentos mais difíceis e stressantes. O seu apoio e paciência para me ouvir nesta reta final foram cruciais para ultrapassar todos os obstáculos que o trabalho experimental me interpôs.

Aos amigos da terra, pela relação que criámos e onde na distância sempre me apoiaram. Aos amigos que fiz na Covilhã, pelos fantásticos anos que passámos juntos e ao fim dos quais partimos, em diferentes direções, atrás dos nossos sonhos. E por último, aos companheiros do instituto que cruzaram o meu caminho durante os meus passados estágios.

Aos intervenientes diretos desta dissertação, gostaria de começar por agradecer ao meu conselheiro Pedro Marques. O seu apoio, otimismo e disponibilidade foram vitais para levar este projeto a bom porto. Enquanto o seu primeiro e pior estudante partilhámos ensinamentos que nunca esquecerei. Por último, gostaria de agradecer aos meus supervisores Prof. André Silva e Prof. Miguel Mendez pelo apoio e orientação durante os passados meses. Para além disso, agradeço à Alessia Simonini e ao Mathieu Delsipée pela ajuda e extraordinárias discussões durante o desenvolvimento da experiência, bem como a toda a equipa do instituto Von Karman.

Resumo

Considerando aplicações espaciais, nenhum fator limita mais o desenvolvimento de um veículo espacial do que o sistema de propulsão. Aqui, os propelentes criogénicos líquidos prevalecem devido ao seu ótimo compromisso entre desempenho e peso. No entanto, com os propelentes líquidos a totalizar até 90% da massa do veículo, surge a preocupação central de sloshing.

Sloshing é definido como o movimento de líquidos dentro de um reservatório e é responsável por misturar o gás e o líquido. Como tal, promove a evaporação ou condensação o que resulta em grandes flutuações de pressão no tanque.

Neste contexto, o projeto atual visa investigar experimentalmente as alterações termodinâmicas em tanques pressurizados devido ao sloshing, através do desenvolvimento de uma experiência inovadora. Consequentemente, as questões de investigação procuraram compreender o impacto dos parâmetros de excitação e de inicialização na evolução termodinâmica do sistema sob sloshing lateral.

A instalação experimental desenvolvida funciona em condições de espécie única através de líquido não criogénico HFE-7200 e é pressurizada através de um tanque externo. As medições foram realizadas numa célula de acrílico com uma altura de 120 mm e um raio de 40.5 mm com uma relação de enchimento de $h/R = 1.44$. A campanha experimental foi efetuada na mesa de sloshing SHAKESPEARE no VKI.

Na campanha experimental, diferentes procedimentos e regimes de sloshing foram investigados. As medições de particle image velocimetry demonstraram a capacidade de mistura do sloshing. Além disso, as imagens capturadas mostram a natureza violenta e a mistura superior de sloshing instável. As medições de pressão corroboraram esta conclusão, onde a queda de pressão devido ao sloshing foi avaliada sob distintas escalas de tempo experimental e condições de excitação.

Palavras-chave

Sloshing, pressure drop, thermal stratification, sloshing induced-mixing, experimental setup.

Abstract

Regarding space applications, no single factor constrains the design of a space vehicle more than the propulsion system. Here, liquid cryogenic propellants prevail due to their optimal trade-off between performance and weight. However, with liquid propellants totalling up to as much as 90% of the vehicle's mass, the central concern of propellant sloshing emerges.

Sloshing is defined as the motion of the free liquid surface within a reservoir and enhances the thermal mixing of the gas and the liquid. This promotes evaporation and condensation, leading to large fluctuations in the tank pressure.

In this context, the current project aimed to experimentally investigate and quantify the thermodynamic changes in pressurised vessels under sloshing conditions by developing a novel reduced-scale laboratory setup. Therefore, the research questions sought to understand the impact of the excitation and initialisation parameters in the system for lateral sloshing.

The designed experimental setup operates in single-species conditions with non-cryogenic liquid HFE-7200 and is pressurised through an external tank. The measurements were carried out in a plexiglass cell with a height of 120 mm and a radius of 40.5 mm at an initial fill ratio of $h/R = 1.44$. The experimental campaign was performed in the SHAKESPEARE sloshing table at VKI.

Throughout the experimental campaign, different procedures and sloshing regimes were investigated. Particle image velocimetry measurements outlined the sloshing-induced mixing capability. Moreover, the captured footage showcased the violent nature and superior mixing of unstable sloshing motions. The pressure measurements further proved this, where the pressure fluctuations were evaluated under distinct experimental time scales and excitation conditions.

Keywords

Sloshing, pressure drop, thermal stratification, sloshing induced-mixing, experimental setup.

Contents

List of Figures

List of Tables

Nomenclature

Latin Symbols

A_f	Forcing motion amplitude	[m]
b	Wave amplitude	[m]
B	Constant value	-
C	Constant value	-
c_p	Specific heat at constant pressure	[J/kg K]
c_v	Specific heat at constant volume	[J/kg K]
D	Diameter	[m]
f	Friction factor	-
g	Gravitational acceleration	[m/s^2]
h	Liquid fill height	[m]
$\hat{h}$	Specific enthalpy	[J/kg]
$\bar{h}$	Heat transfer coefficient	[W/m^2 K]
H	Tank inner height	[m]
J	Area-specific net mass phase change	[kg/m^2 s]
J_{mn}	First kind Bessel function	-
J'_{mn}	First kind Bessel function derivative	-
k	Thermal conductivity	[W/m K]
k_b	Boltzmann constant	-
L_c	Characteristic length	[m]
$\dot{m}''_\delta$	Area-specific net mass phase change	[kg/m^2 s]
M	Molar mass	[kg/mol]
p	Pressure	[Pa]
$\dot{q}$	Area-specific heat flux	[W/m^2]
$\dot{Q}$	Heat flux	[W]
R	Tank radius	[m]
R_I	Radii of curvature	[m]
R_{II}	Radii of curvature	[m]
R_s	Specific gas constant	[J/kg K]
$\bar{R}$	Universal gas constant	[J/kg mol]
S	Standard error	-

t	Time	[s]
T	Temperature	[K]
T_ω	Oscillation period	[s]
$T_{mn}(t)$	Velocity potential time-dependent function	-
$\hat{u}$	Specific internal energy	[J/kg]
v	Specific volume	[m^3/kg]
V	Volume	[m^3]
$\dot{W}$	Work	[W]
$X(t)$	Excitation function	[m]

Greek Symbols

α	Thermal diffusivity	[m^2/s]
α_e	Effective thermal diffusivity	[m^2/s]
β	Thermal expansion coefficient	[1/K]
β_i	Frequency offset	-
γ	Viscous damping	-
ε	Small parameter	-
η	Free surface displacement	[m]
λ_{sf}	Scaling factor	-
μ	Dynamic viscosity	[Pa s]
ν	Kinematic viscosity	[m^2/s]
ξ	Minor losses	-
ξ_{mn}	Bessel function derivative root	-
ρ	Density	[kg/m^3]
σ	Surface tension	[N/m]
$\bar{\sigma}$	Accommodation coefficient	-
τ	Shear stress	[N/m^2]
$\bar{\tau}$	Generic time-scale	[s]
ω	Forcing frequency	[rad/s]
ω_{mn}	Sloshing mode natural frequency	[rad/s]
δ	Damping ratio	-
δ_T	Thermal boundary layer thickness	[m]
Δh_v	Latent heat of vaporisation	[J/kg]

Δt	Time interval	[s]
Φ	Velocity potential	[m^2/s]

Subscript

0	Reference condition
i	Interface
init	Initialisation
L	Liquid
m	Mode number
min	Minimum
n	Wave number
p	Constant pressure
press	Pressurisation phase
ref	Reference
relax	Relaxation phase
s	Sloshing
sat	Saturation
sf	Scaling factor
slosh	Sloshing phase
strat	Thermal stratification phase
U	Ullage
v	Constant volume
w	Wall

Vectors

g	Gravitational acceleration vector	[m/s^2]
n	Normal vector	-
V	Flow velocity vector	[m/s]

List of Abbreviations

0D	Zero dimensional
2D	Two dimensional
CL	Cylindrical lens
CV	Control Volume
DA	Dimensional Analysis
ELGRA	European Low Gravity Research Association
ESA	European Space Agency
ESC-A	Étage Supérieur Cryogénique A
ESC-B	Étage Supérieur Cryogénique B
FFT	Fast Fourier Transform
GH_2	Gaseous Hydrogen
GHe	Gaseous Helium
GN_2	Gaseous Nitrogen
H_2	Hydrogen
IVP	Initial Value Problem
LH_2	Liquid Hydrogen
LLPM	Lower Liquid Propulsion Module
LN_2	Liquid Nitrogen
LOx	Liquid Oxygen
N_2	Nitrogen
PIV	Particle Image Velocimetry
RHS	Right Hand Side
ROI	Region of Interest
ROM	Reduced Order Model
RQ	Research Question
SE	Scaling of Equations
SL	Spherical lens
UBI	Universidade da Beira Interior
ULPM	Upper Liquid Propulsion Module
VKI	von Karman Institute for Fluid Dynamics
ZARM	Centre of Applied Space Technology and Microgravity

Chapter 1

Introduction

Orbital launch vehicles have been used since the early 1950s, and up until today, they remain the only feasible technological solution to convey a payload from the Earth's surface to space [1]. To accomplish such, their mission rests upon escaping from the Earth's atmosphere and gravity, to which a large fuel load is imperative.

Therefore, one can foresee from their fundamental mission, may it be low Earth orbit or deep space expeditions, that no single factor constrains the design of a space vehicle more than the propulsion technology. Commonly, this subsystem relies on the combustion of chemical propellants, more specifically liquid propellants, due to their high thrust-to-weight ratio and nearly altitude-independent thrust [2]. These rocket engines use fuel and oxidisers fed under pressure from tanks into a high-pressure combustion chamber by the propellant feed system.

While most modern propulsion systems employ liquid oxygen (LOx) as the oxidiser and liquid hydrogen (LH_2) as the fuel, significant drawbacks arise from their cryogenic nature: (a) their low saturation temperature results in significant boil-off, leading to pressure buildup, abnormal propellant conditions for engine usage and propellant loss (e.g. hydrogen saturation temperature $T_{\text{sat}} \approx 20$ K at ambient conditions) [3, 4]; (b) they cool the tank wall far below the ambient temperature, instigating ice buildup during and prior to launch, which increases vehicle's inert mass and may damage the launcher once it breaks during the initial flight phase [2]; (c) cryogenic hydrogen offers a much lower energy density per volume than kerosene, resulting in bulky tanks and airframe designs.

The next European expendable launch vehicle on behalf of the European Space Agency (ESA), Ariane 6, is depicted in Figure 1.1 and has been in development since the early 2010s, with the maiden launch scheduled for 2023 [5]. The Ariane 6 resorts to hybrid staging and comprises three stages: two (A62) or four strap-on boosters (A64) and a lower and upper stage (central core) [6]. The strap-on boosters are P120C solid rocket boosters (SRBs) with a propellant mass of 142.000 kg individually. The central core lower stage, with an expected diameter of 5.4 m, entitled the Lower Liquid Propulsion Module (LLPM),

Figure 1.1: Artist's view of the Ariane 6 configuration A64: four strap-on boosters, Upper Liquid Propulsion Module (ULPM) and the Lower Liquid Propulsion Module (LLPM) [6].

is propelled by burning liquid hydrogen (LH_2) with liquid oxygen (LOx) by a single Vulcain 2.1 engine carrying up to 150.000 kg of propellant. The upper stage ignited outside the atmosphere, known as the Upper Liquid Propulsion Module (ULPM), employs the same hydrolox system with a propellant mass of 31.000 kg through a reignitable Vinci engine ensuring atmospheric re-entry from the upper stage [7, 8].

Hereupon, resorting to Figure 1.1 and Table 1.1 in which a mass breakdown of orbital space launchers is displayed, it is evident that the propulsion system heavily constrains the design as most of the launcher's volume is occupied by the liquid propellant.

Table 1.1: Propellant mass fractions of existing and outdated LH_2/LOx upper and core stages as a ratio of the total usable propellant mass and vehicle's gross liftoff mass [9]. The usable propellant mass accounts for reserves, liquid residuals, engine restart, purges and boil-off of cryogenic propellants[10].

		Usable propellant mass [t]	Gross lift-off mass [t]	Propellant mass fraction [-]
Upper stages	SS-L9-5E	10.1	11.2	0.902
	SS-ESC-B	28.2	32.2	0.878
	Atlas V SS	20.8	22.9	0.908
	Delta IV-H SS	27.2	30.7	0.886
Core stages	H158 Ariane 5G	158.1	170.3	0.928
	Shuttle ET	721.1	748.1	0.964
	Delta IV-H CS	199.6	226.4	0.882
	Ares V CS	1587.6	1760.9	0.902

1.1 Motivation and objectives

Liquid sloshing is defined as the movement of the free liquid surface within a reservoir [11] and is induced by dynamic perturbations (e.g. booster separation or aerodynamic loads) during propelled flight phases [12]. Sloshing is responsible for inducing two types

of undesirable side effects:

- **Dynamical phenomenon** where the displacement of the fuel tank's centre of mass causes undesired forces and undermines the stability and manoeuvrability of the spacecraft;
- **Thermodynamical phenomenon** where thermal mixing between the pressurised ullage and subcooled liquid may cause large fluctuations in the tank pressure coupled with thermal variations, leading to structural instabilities and thrust oscillations in the propulsive system.

Prior to launch, the propellant tanks are pressurised according to the optimal operating conditions for the propellant feed system, typically in the order of 300 kPa for a pump-fed system [13, 14, 15]. As such, if the holding time is large enough, a vertical thermal stratification develops in the liquid due to natural convection and conduction. As depicted in Figure 1.2a, the liquid's thermal field features a warmer region extending from the interface until a depth δ_T and a subcooled region defined by a quasi-homogeneous condition. If side accelerations induce sloshing, the warmer liquid in the thermal boundary layer mixes with the subcooled liquid from the bulk, lowering the temperature at the free surface. The destratification (depicted in Figure 1.2b) results in the cooling of the ullage gas, as well as condensation. Consequently, the pressure within the tank drops, altering the propellant flow to the combustion chamber [2]. The magnitude of this drop depends on (a) the sloshing regime, (b) the pressurisation technique, (c) the pressurant type and (d) the ullage volume [14, 16].

The above-mentioned characteristic pressure drop has been reported to occur in ESA (European Space Agency) flights at the Ariane's 5 upper stage during the ascent phase, and sloshing was identified as the most likely source [17]. Thereby, pinpointing the relevance of studying the thermodynamics of closed containers carrying cryogenic liquids, which can be further extended to long-term storage, and propellant loading scenarios of cryogenics [18].

The current research framework focuses on evaluating the thermodynamic evolution of a closed container, characterised by the enhancement of the heat and mass transfer between the liquid and surroundings due to its dynamic behaviour. The research questions we seek to answer in this master's thesis project are:

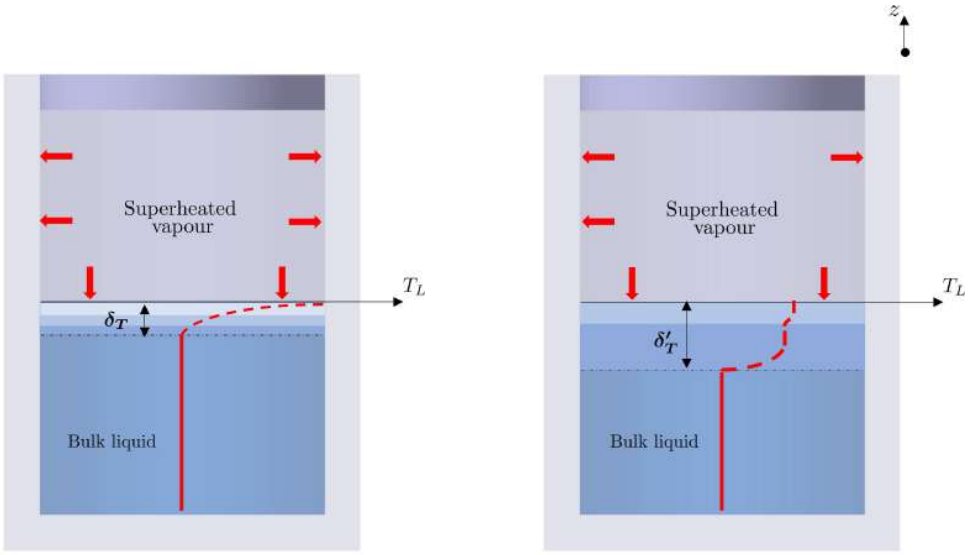

(a) Thermal profile before sloshing initialisation. (b) Thermal profile after sloshing induced mixing.

Figure 1.2: Schematic representation of the evolution of vertical temperature profiles and the thickness of thermal boundary layers in the liquid's uppermost region adapted from Lacapere et al. (2009) [19].

1. **RQ1:** What is the sloshing excitation condition's impact on the thermodynamic evolution of the system?

2. **RQ2:** What is the impact of different initial thermodynamic conditions (e.g., tank pressure, ullage temperature and thermal boundary layer thickness) on the evolution of the system under lateral sloshing conditions?

To do so, this study aims to develop a reduced-scale experiment using non-cryogenic replacement fluids such as HFE-7200 and HFE-7000 to characterise the heat and mass transfer due to sloshing-induced mixing in orbital launch vehicles during the propelled flight phase [20]. Here the quantities to measure are ullage pressure, gas and liquid temperature, and external wall temperature. Furthermore, optical measurements must be used for sloshing condition's characterisation.

In addition, the resulting small-scale experiment developed for ground-based characterisation represents the first iteration of the VKI (von Karman Institute for Fluid Dynamics) experimental campaign under reduced gravity conditions, which will take place in 2023 onboard the 80th European Space Agency (ESA) parabolic flight [21]. The facility's operational learning outcomes will translate the results on-ground into an improved design for the parabolic flight campaign.

1.2 State of the art

Even though substantial information is available on liquid sloshing dynamics [11, 22, 23, 24, 25], the coupling with thermodynamic phenomena present during the sloshing of cryogenic liquid propellants is yet a field with many open questions. The most relevant works done up to date are hereafter briefly exhibited.

Moran et al. [26] resorted to a 1750 litre spherical tank instrumented with silicon diodes for temperature and pressure transducers. They experimentally characterised liquid hydrogen sloshing by varying the following parameters: (a) slosh frequency and amplitude; (b) pressurant type; (c) ramp pressure; (d) ullage volume. This work still prevails as one of the most complete experimental parametric studies on non-isothermal sloshing. Here the test series revealed that the nature of the sloshing regime has dramatic effects, where under unstable chaotic sloshing ($\omega = 0.74$ Hz and $A_f = 0.0381$ m), the pressure dropped about 50% while for stable planar sloshing ($\omega = 0.74$ Hz and $A_f = 0.0127$ m) the pressure dropped by 15%. Additionally, through sensitivity analysis for 51%, 33% and 13% ullage volumes, it was concluded that with reduced volumes, the tank pressure was more susceptible to interfacial condensation. Hence, the sloshing regime and fill level significantly impact the system's thermodynamic response.

Das and Hopfinger [20] conducted experimental work using non-cryogenic replacement fluids FC-72 and HFE-7000. The experiments were conducted in a 0.9 litre flat-bottom circular cylindrical tank, instrumented with thermocouples and a pressure transducer in the tank lid. The experimental procedure ensured a single-species system by vacuuming and pressurising the cell with vapour. Even though the system was not cryogenic, the thermodynamic condition was such that a pressure drop could be achieved. Das and Hopfinger studied the sloshing regime's impact on the heat and mass transfer enhancement at the liquid-gas interface by vertically oscillating tank. Moreover, an empirical correlation was derived for the pressure drop as a function of an effective diffusion coefficient. This effective diffusion coefficient model was later extended by Ludwig et al. [27] to a forced convection empirical Nusselt correlation.

Lacapere et al. [19] evaluated the sloshing thermal destratification phenomenon through an experimental and numerical approach. The sloshing experiments were performed with liquid nitrogen (LN_2) and liquid oxygen (LOx) using a cryostat with radius $R = 0.091$ m and height $H = 0.8$ m, instrumented with ten temperature sensors to measure thermal

stratification. Two pressure sensors were added at the bottom and the top of the cryostat. The dewar was filled to 55% of its total volume and pressurised to about 2.5 bar, after which chaotic sloshing was induced ($\omega = 2.1$ Hz and $A_f = 0.003$ m). Here a pressure drop of around 40% was measured for experiments with LN_2 after GN_2 pressurisation.

At ZARM, pressure fluctuations induced by lateral sloshing were experimentally explored in a cylindrical dewar with a spherical bottom holding LN_2. The tank pressure was measured with a pressure sensor located in the tank lid, and the temperature was monitored by silicium diodes. The results of such research are described across the works of Arndt [14], Ludwig [27] and Van Foreest [16]. Arndt [14] applying three different methods to pressurise the system self-pressurisation, external nitrogen (GN_2) pressurisation, and external helium (GHe) pressurisation evaluated the characteristic pressure drop for stable planar sloshing ($\omega = 1.4$ Hz and $A_f = 0.01$ m). From this experimental campaign, he concluded that using a non-condensable inert gas (GHe) decreases the impact of the pressure drop. Moreover, this effect could be entirely eradicated for high helium pressurant gas concentrations, which is in agreement with the results acquired by Moran et al. [26]. Van Foreest [16] using Arndt [14] experiments as a reference, developed a 1D engineering model for the simulation of thermal stratification in the liquid and heat and mass transfer during sloshing [28]. Ludwig et al. [27] studied the impact of different sloshing conditions for GN_2 pressurisation and performed pressurisation and relaxation tests [13, 29] to parametrically characterise the active pressurisation system behaviour.

1.3 Outline

The remainder of this master's thesis is structured as follows:

- Chapter 2, the fundamentals of liquid sloshing dynamics are introduced by describing the potential and Miles' weakly nonlinear theories. Besides, thermal stratification and sloshing-induced mixing are overviewed ahead of defining the characteristic pressure drop phenomenon. This chapter showcases modelling equations and a complete problem characterisation by resorting to previous research in the field.

- Chapter 3, a scaling analysis for the current gravity-dominated non-isothermal sloshing problem is developed where similarity between the full-size facility Ariane 6 and

the reduced-scale laboratory experiment is assessed, resorting to characteristic experimental conditions and distinct working fluids.

- Chapter 4 introduces the experimental setup and methods used throughout the experimental campaign. The design approach is set here, and the active-pressurisation system 0D ROM (Reduced Order Model) is derived and parameterised. Lastly, the procedure is described and the experimental matrix defined.
- Chapter 5 showcases the results acquired from the facility troubleshooting and operational tests. Furthermore, the overall results that answer to the proposed research questions are presented and scrutinised.
- Chapter 6 closes the thesis by summarising the main findings derived from this work and proposes improvements to the small-scale laboratory facility that will embark on board the 2023 ESA parabolic flight campaign.

Chapter 2

Theoretical background

The present chapter establishes the theoretical foundations of sloshing. It starts with an introduction to sloshing dynamics, described through potential flow theory (section 2.1.1). Likewise, Miles' weakly nonlinear theory couples the amplitude-frequency response of the tank to the sloshing regime (section 2.1.2). Furthermore, as the focus of the research turns into the thermodynamical phenomena during sloshing, thermal stratification (section 2.2), as a significant contributor to pressure drop effects, is brought to light before diving into the coupling between heat transfer and sloshing (section 2.3). Subsequently, the physics behind pressure fluctuations in liquid propellant tanks (section 2.4) are scrutinised, and emphasis is given to the liquid-vapour phase change (section 2.4.1).

2.1 Liquid sloshing dynamics

Liquid sloshing dynamics research became of significant interest in the early 1960s, with the ongoing space race and the central concern of propellant sloshing in launch vehicles. The major linear and nonlinear theories that describe this phenomenon were derived in this decade and to the present day, the work developed by Abramson [11] is still one of the most complete compendiums that highlight the fundamentals of liquid sloshing.

The response of liquids enclosed in a container is determined by its geometry, as well as the frequency and amplitude of the excitation. Therefore, the analysis must be tailored to a given tank shape and external disturbance to proceed further. Figure 2.1 showcases an illustration of a flat-bottom circular cylindrical reservoir, which is the configuration in analysis for the present research. Furthermore, experimental testing at VKI is performed in a sloshing cell with the aforementioned characteristics (section 4.1.2). On the other hand, a sinusoidal lateral excitation is the external input that most accurately describes the circumstances a full-size facility would stand for [14, 16].

The cylindrical tank has a radius R and is filled up to a height denoted by h, representing

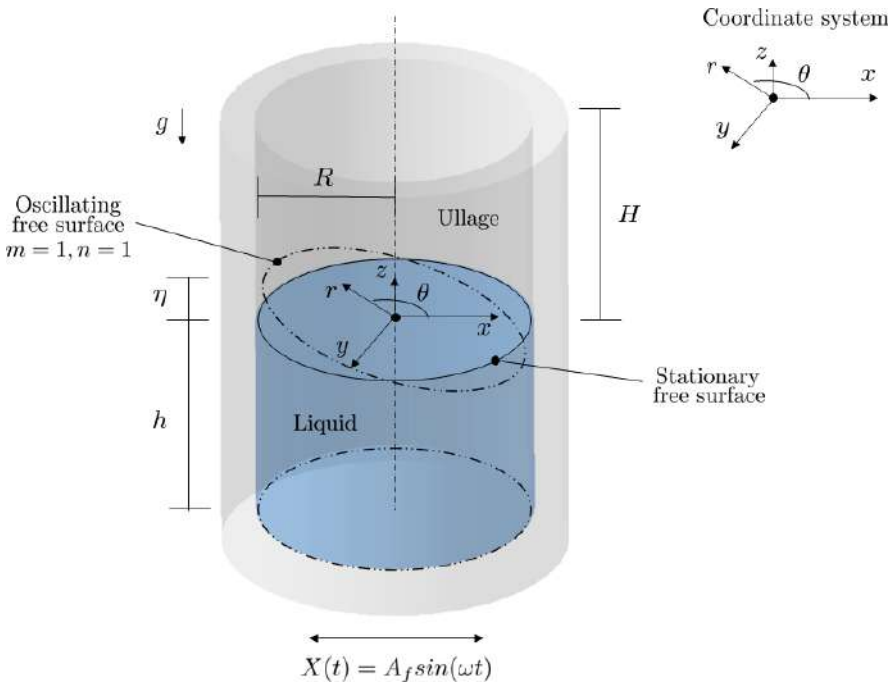

Figure 2.1: Schematic illustration of the tank consisting of a liquid and an ullage phase. The axes are defined in cylindrical and cartesian coordinates, with the stationary free surface acting as the origin.

the vertical position of the liquid free surface from the bottom of the tank. Due to an external sinusoidal excitation in the x direction, with an imposed amplitude of A_f and forcing frequency ω, the free surface will oscillate and be vertically displaced as much as η, relative to the stationary reference.

2.1.1 Linear sloshing theory

This section introduces the linear sloshing theory, in which analytical expressions for the velocity potential function, fluid free surface motion and natural frequencies, and mode shapes are derived. Even though this analysis does not consider complex free surface phenomena near resonance conditions, it is still the predominant theory behind the study of sloshing dynamics with the following set of assumptions [11, 22]:

1. The pressure vessel is rigid;
2. Inviscid fluid ($\mu = 0$);
3. Incompressible fluid ($\nabla \cdot \mathbf{V} = 0$);
4. Homogeneous fluid;
5. Small displacements, velocities, and slopes of the liquid-free surface;

6. Irrotational flow field ($\nabla \times \mathbf{V} = 0$);
7. No sinks or sources;
8. Gravity-dominated flow (**Bo**$\gg 1$);
9. Harmonic forced excitation: $X(t) = A_f \sin(\omega t)$.

Resorting to assumption (6), which is compatible with the assumption (2) of zero viscosity, it is possible to ensure a single velocity potential function, $\Phi(r, \theta, z, t)$, exists and its gradient derives the velocity field (equation 2.1).

$$\mathbf{V} = \nabla \Phi \tag{2.1}$$

The solution to the field equation that satisfies the boundary conditions for a cylindrical reservoir is expressed for individual wave modes and wave numbers by equation 2.2 (for full derivation resort to [22, 23]).

$$\Phi_{mn}(r, \theta, z, t) = \underbrace{J_m\left(\lambda_{mn} r\right)}_{f_1(r)} \underbrace{\cos(m\theta)}_{f_2(\theta)} \underbrace{\frac{\cosh\left[\lambda_{mn}(z+h)\right]}{\cosh\left(\lambda_{mn} h\right)}}_{f_3(z)} \underbrace{T_{mn}(t)}_{f(t)} \tag{2.2}$$

Where $T_{mn}(t)$ is a time-dependent function determined from the imposed forcing conditions, m is the mode number and n is the wave number which describe the number of wave peaks in the circumferential direction and the number of wave peaks in the radial direction, respectively. J_m is the first kind Bessel function of the m^{th} order and $\lambda_{mn} = \xi_{mn}/R$, in which ξ_{mn} is given by the n^{th} root of the derivative of the Bessel function ($J'_m\left(\xi_{mn}\right) = 0$).

For the free-oscillations solution the time function, in equation 2.2, was assumed by Abramson [11] to be of the form $\mathrm{e}^{i\omega_{mn}t}$, leading to the following solution for the velocity potential,

$$\Phi_{mn}(r, \theta, z, t) = \underbrace{J_m\left(\lambda_{mn} r\right)}_{f_1(r)} \underbrace{\cos(m\theta)}_{f_2(\theta)} \underbrace{\frac{\cosh\left[\lambda_{mn}(z+h)\right]}{\cosh\left(\lambda_{mn} h\right)}}_{f_3(z)} \underbrace{\mathrm{e}^{i\omega_{mn}t}}_{f(t)} \tag{2.3}$$

where ω_{mn} defines the natural frequency of a given mode frequency, as described in section 2.1.1.1. Figure 2.2 showcases the first kind of Bessel function of m^{th} order, and Table 2.1 displays the derivative roots of the first order Bessel function.

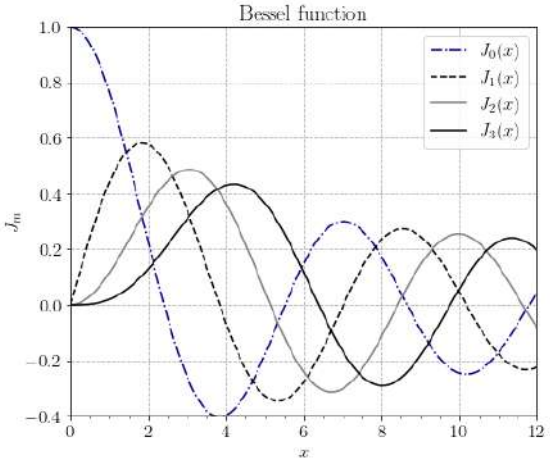

Figure 2.2: First kind Bessel function of the m^{th} order.

Table 2.1: Roots of the derivative of the Bessel function of the first order $J'_m(\xi_{mn}) = 0$.

ξ_{mn}		J'_0	J'_1	J'_2	J'_3
	1	3.831	1.841	3.054	4.201
n	2	7.016	5.331	6.706	8.015
	3	10.173	8.536	9.969	11.346

2.1.1.1 Normal modes frequency

Liquid slosh inside a finite domain leads to the reflection of the waves at the container boundaries. Under a specific frequency, superposition between the waves reflected back and forth takes place. This coupling develops a normal mode, creating a standing wave with a given spatial pattern. Understandably, modal analysis is of vital importance to determine the liquid-slosh natural frequencies since one must ensure the control system natural frequencies, the elastic body frequencies and any of the dominant slosh frequencies are widely separated [11, 22].

Resorting to the velocity potential, equation 2.3, one can obtain the following expression.

$$\omega_{mn}^2 = \frac{g\xi_{mn}}{R} \tanh\left(\frac{\xi_{mn}h}{R}\right) \tag{2.4}$$

The equation reveals that the natural frequency of propellant motion is dependent on tank dimensions, vertical acceleration magnitude, and fluid depth but not on fluid properties. This is a consequence of assumption (8), which leads to a properties independent free surface boundary condition [22]. Additionally, equation 2.4 might be simplified by neglecting the influence from the tank bottom, under the consideration of high fill ratios (h/R) in which $h/R \geq 1$ [14, 30]. Figure 2.3 depicts the plot of dimensionless natural frequencies $\omega_{mn}(g/R)^{-1/2}$ versus fill ratios for various asymmetric modes, showcasing the validity of this premise.

As such, the natural frequency for high fill ratios might be computed through equation 2.5.

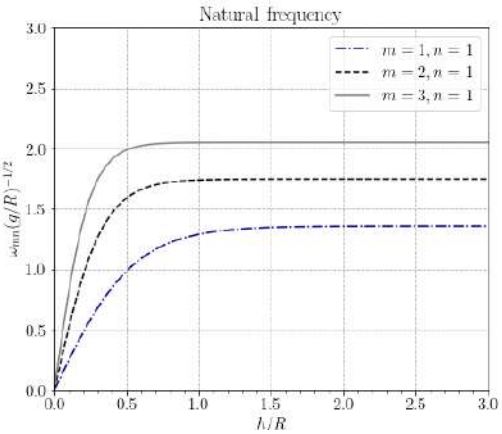

Figure 2.3: Dimensionless natural angular frequencies of the asymmetric sloshing modes as a function of the fill ratio h/R.

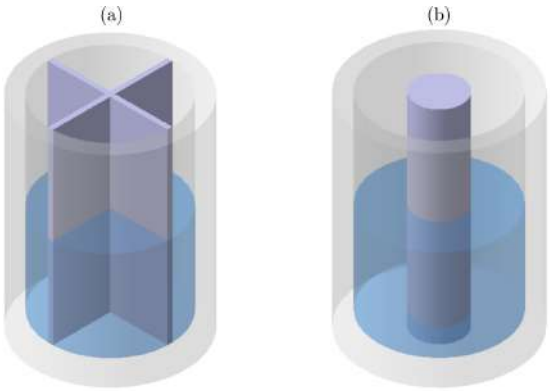

Figure 2.4: Representation of tanks compartmentalisation's (a) sectored tank and (b) annular tank.

It shows that for high Bond number (**Bo**) flows, the natural frequency of a given mode is only a function of the tank radius and its axial acceleration [22, 24].

$$\omega_{mn} = \sqrt{\frac{g\xi_{mn}}{R}} \tag{2.5}$$

As a result, if a shift in the sloshing frequency range is required, the most effective strategy is to modify the pressure vessel geometry. Baffles are fairly ineffective, and partitioning the tank into sub-tanks or compartments by radial or concentric walls is better [24]. Figure 2.4 displays an example of two compartmented tanks. Despite this, one should note that radial compartmentation is less effective than ring baffles in lowering the amplitude of slosh forces and torques [11].

2.1.1.2 Normal modes

To characterise a sloshing mode it is fundamental to formulate the resulting surface shape under the respective natural frequency.

The resulting surface shapes for $0 \leq m \leq 3$ and $1 \leq n \leq 3$ are displayed in Figure 2.5, in which two kinds of modes are observed: (a) asymmetric modes which are related to horizontal oscillations of the centre of mass; (b) symmetrical modes along the vertical axis that do not cause any resultant forces and are often difficult to generate and thus rarely observed [24]. Hereupon, the frequencies of major relevance in symmetric cross-section tanks are the lowest few, corresponding to the first few anti-symmetric sloshing modes.

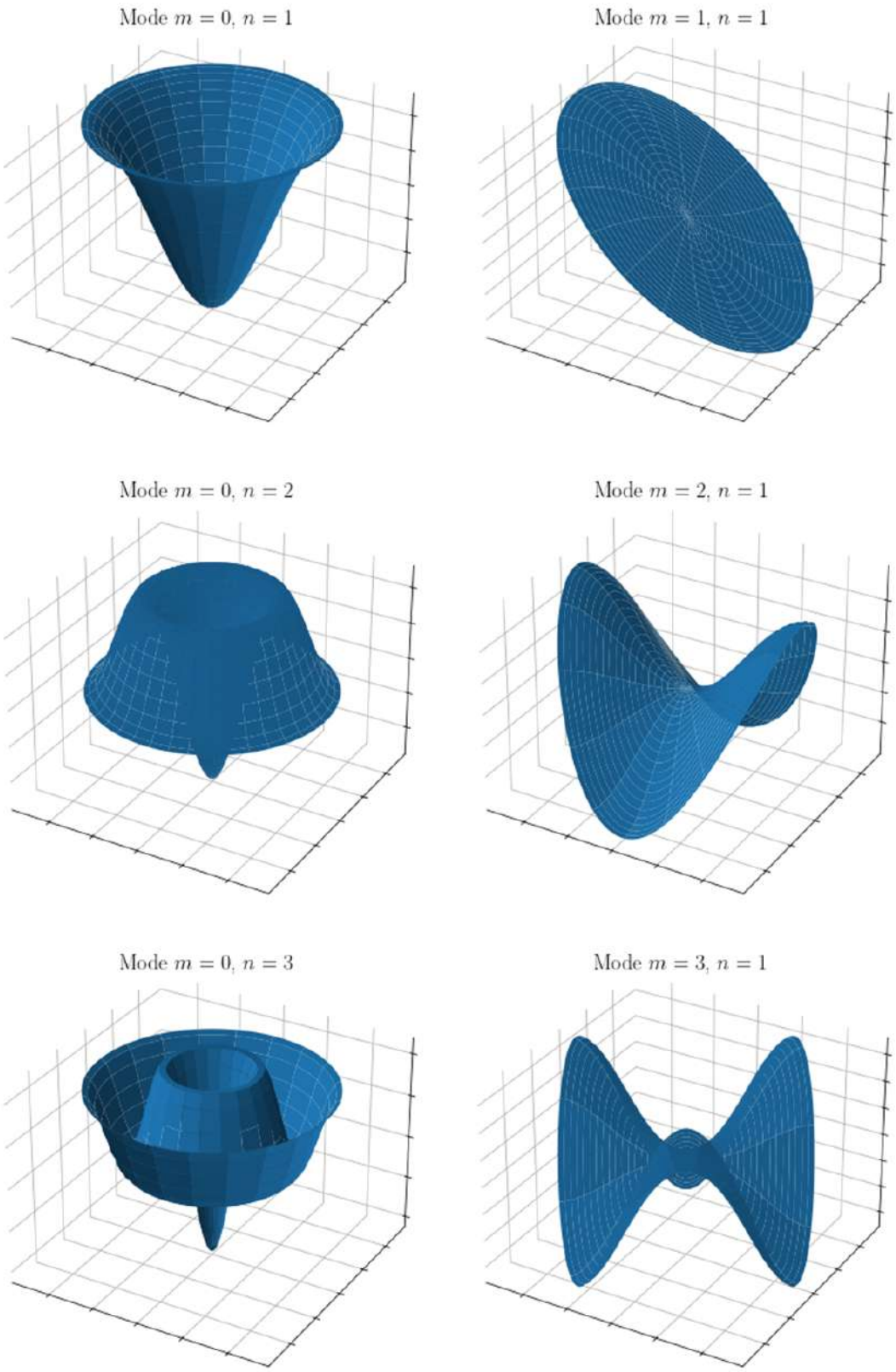

Figure 2.5: Different sloshing modes of excited liquid in a cylindrical tank. The surface contour of the sloshing liquid is depicted.

Mode $m = n = 1$, characterised by a slosh wave with one peak and one valley, generating approximately a flat disk, is the fundamental wave since it is defined by the lowest eigenfrequency as depicted in Figure 2.3 [23]. Consequently, this mode is usually found in space launcher tanks during the ascent phase [16, 31].

2.1.2 Weakly nonlinear sloshing theory

In the previous section 2.1.1 the linear sloshing theory was introduced, considering the amplitude of the sloshing wave is sufficiently small that the wave responses are linear. Nonetheless, it does not take into account non-linearities that can arise from three classes: (a) the geometry of the pressure vessel; (b) as a result of high wave amplitudes; (c) those involving fundamentally distinct types of sloshing regimes as a result of instabilities near resonance [11, 24]. For the present study case, it is critical to define the nonlinear behaviour of liquid sloshing that leads to distinct sloshing regimes since, as analysed in section 1.2, different regimes lead to distinct interface heat and mass transfer behaviours.

Experimentally observed [25, 32], these free surface instabilities develop into non-planar unstable motion linked with rotation of the nodal diameter (rotary sloshing) and chaotic sloshing beyond the stable planar motion. Consequently, the sloshing characteristics for the different regimes are as follows:

1. **Stable planar waves** are a harmonic steady-state liquid motion, defined through the linear theory, depicted in section 2.1.1, with a fixed peak wave height and a single nodal diameter that is stationary and perpendicular to the direction of excitation. This planar motion is observed far off the neighbourhood of the natural frequency of a given mode [33]. The maximum wave amplitudes, b, of the stable, planar wave motions can be estimated from equation 2.6 [27].

$$\frac{b}{A_f} \approx 2 \left[\frac{\left(\frac{\omega}{\omega_{11}}\right)^2}{1 - \left(\frac{\omega}{\omega_{11}}\right)^2} \right] \tag{2.6}$$

2. **Chaotic sloshing** is a non-planar unstable motion close to the natural frequency. Under a chaotic regime, wave breaking might arise, provided that the maximum downward acceleration ($b\omega^2$) exerted on a liquid particle at the free surface is equal to the gravitational acceleration. This phenomenon takes place when the amplitude

reaches a maximum of approximately 25% of the tank diameter [24]. Eventually, the wave collapses, and a new cycle starts. One must notice that wave breaking causes substantial surface disturbances with plunging jets that produce surface layer mixing. The wave amplitude rises linearly in time and is almost proportional to the forcing amplitude, as defined in equation 2.7 [27], where t defines the time instant and T_ω the oscillation period.

$$\frac{b}{R} \approx \pi \frac{A_f}{R} \frac{t}{T_\omega} \tag{2.7}$$

3. **Rotary sloshing** is defined as rotational non-planar motion about the normal axis, arising near and above the resonance conditions of a given mode. The swirl motion is characterised by local breaking near the wave top, but once established, is very stable and transfers angular momentum to the whole liquid [25]. This regime yields what is referred to as a "beating" by Abramson (1966) [11], since the rotational motion increases in angular velocity in one direction (e.g. counterclockwise) until reaching a maximum and collapsing to nearly zero. Afterwards, it reverses direction and re-gains angular momentum. The average swirl wave amplitude is approximately 35% of the tank diameter [27].

Figure 2.6 displays experimental observations performed at VKI for the aforementioned sloshing regimes.

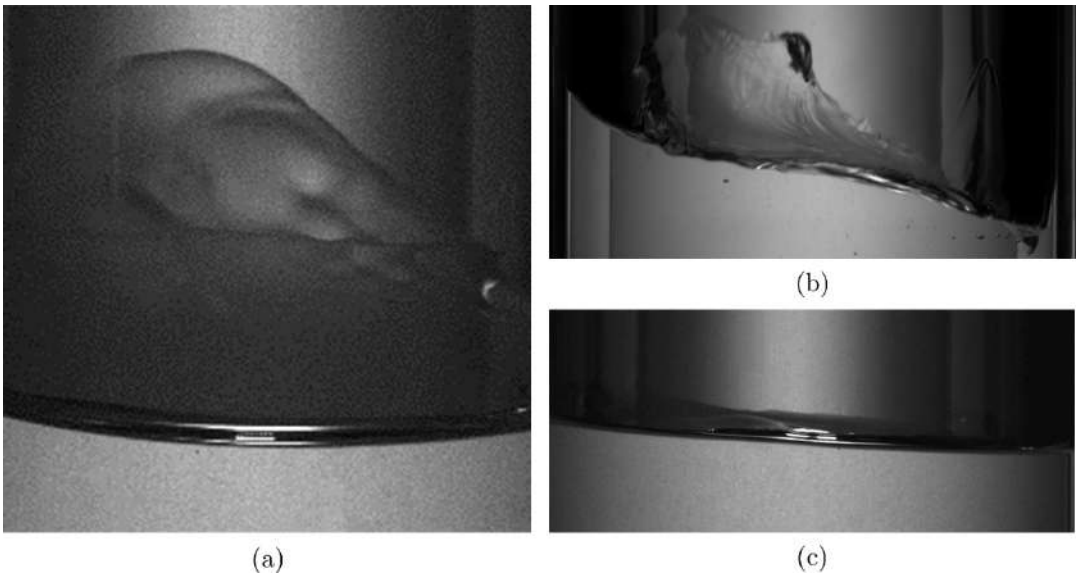

Figure 2.6: Images of (a) swirl wave mode with breaking near the top, (b) chaotic sloshing near wave breaking conditions, and (c) stable first asymmetric wave mode [34].

These free surface instabilities can be investigated by resorting to Miles' weakly nonlinear theory [33], from which it is possible to extract the bounds between regimes depending on three parameters. The first parameter is the viscous damping, γ, defined in equation 2.8, where δ represents the damping ratio and ε a small parameter [25].

$$\gamma = \frac{2\delta}{\varepsilon^2} \tag{2.8}$$

Considering the damping occurs mainly at the side-wall boundary layers, the damping ratio is defined through equation 2.9, for the lowest asymmetric mode [35]. Additionally, the small parameter is obtained by equation 2.10 as a function of the dimensionless forcing amplitude, A_f/R.

$$\delta = \left(\frac{\nu^2}{R^3 g}\right)^{1/4} \tag{2.9}$$

$$\varepsilon = \left(1.684\frac{A_f}{R}\right)^{1/3} \tag{2.10}$$

The current theory is only valid provided low damping conditions are met, where $\gamma^2 \ll 1$, which implies the use of low-viscosity liquids [25]. Likewise, experiments show that the theory remains valid as long as $\varepsilon \leq 0.5$ [35].

The second parameter is the frequency offset, β_i, detailed in equation 2.11, for the lowest asymmetric mode. It relates the driving frequency and amplitude to the mode natural frequency [33].

$$\beta_i = \frac{\omega^2 - \omega_{11}^2}{\varepsilon^2 \omega_{11}^2} \tag{2.11}$$

The third and last parameter is the fill ratio since one must ensure the requirement of deep-water conditions is met (section 2.1.1.1). Otherwise, the non-linearity changes and different sloshing regimes arise under the same forcing conditions [33].

Under these parameters and respective restrictions, Miles determined the bounds between the distinct regimes through the definition of specific frequency offsets: $\beta_2 = -0.36$,

$\beta_3 = -1.55$, and $\beta_4 = 0.735$. The graphical representation of the relation between dimensionless forcing amplitude, A_f/R, as a function of ω/ω_{11} depicted in Figure 2.7 is formulated through equation 2.12.

$$\frac{A_f}{R} = \frac{1}{1.684}\left[\frac{(\omega/\omega_{11})^2 - 1}{\beta_i}\right]^{3/2} \tag{2.12}$$

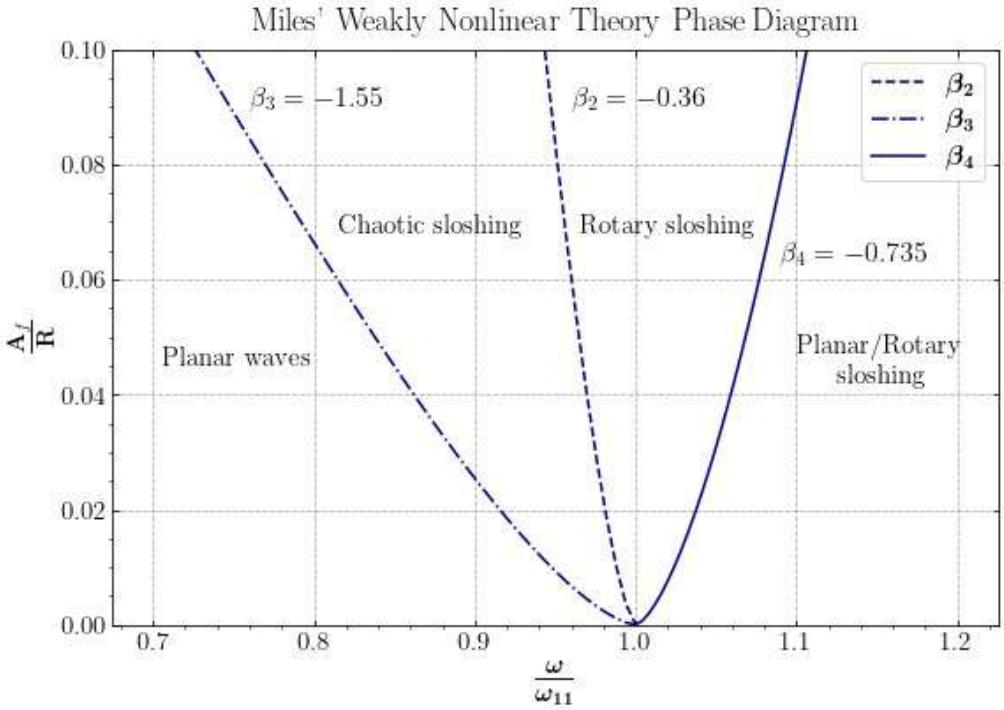

Figure 2.7: Dimensionless forcing amplitude-phase diagram as a function of frequency ratio according to Miles' weakly nonlinear theory [33].

From Figure 2.7, it is possible to assess that at small values of dimensionless forcing amplitude, and at forcing frequencies away from the natural frequency, planar motion arises as predominant sloshing regime. As one increases the frequency to near resonance conditions, it reaches a critical value, where bifurcation to chaotic sloshing occurs. It should be noted that wave breaking conditions are predominant near the boundary β_3 while adjacent to β_2 chaotic wave motion endures without wave breaking. Between $\beta_2 < \beta_i < \beta_4$ the motion is dominated by rotary sloshing that due to its robustness, it is possible to prevail up to $\omega/\omega_{11} \approx 1.3$ [25]. All in all, as one starts by forcing frequencies away from the natural frequency, dominated by planar motion, and approaches resonance, the sloshing regime will bifurcate to swirling motion if $\omega > \omega_{11}$ or too chaotic motion if $\omega < \omega_{11}$.

2.2 Thermal stratification

Thermal stratification refers to the formation of a growing layer of thermally stratified liquid that is hotter than the bulk. This is the primary phenomenon behind the characteristic pressure drops that take place in pressure vessels under sloshing conditions [19, 27, 31]. As such, it is critical to develop a complete picture of the problem related to the heat transfer mechanisms. In the current analysis, heat transfer inside the reservoir is considered to be dominated by convection and conduction, while external heating arises mainly from radiation.

While considering cryogenic propellant tanks, one must understand that outside temperature control is difficult to achieve, unlike storable propellant tanks. Thus, cryogenic propellants may be up to $38°$C below the outer wall temperature, mainly due to solar heating [11, 36]. Therefore, unavoidable external heat leaks develop convective flows that, due to buoyancy effects, transport the warmer liquid to the tank interface, leading to the formation of a warm liquid ”pocket” that evolves over time [37, 38].

On the other hand, conduction mechanisms across the walls and the ullage also have an impactful role in increasing the thermal stratification. From the warm ullage vapour, heat is conducted to the interface mainly by two mechanisms: (a) tangentially through the tank walls; (b) direct interaction between the vapour and the cold liquid at the free surface.

The wall tangential heat flux develops due to the much higher wall temperature in the warmer ullage region. This heat is conducted across the ullage walls and enters the liquid near the free surface [16, 28, 29]. Additionally, since the quiescent superheated gas is in direct contact with the subcooled liquid, a conductive heat flux across the free surface will also coexist. It should be noted that heat transfer at the interface might be enhanced with vapour bulk motion.

A schematic representation of the aforementioned heat fluxes across a closed reservoir with a liquid height h and the respective development of a thermal boundary layer δ_T, as a time function t near the liquid-gas interface, is represented in Figure 2.8.

To evaluate the growth rate of the stratified region due to liquid natural convection, one must develop an integral boundary layer analysis by assessing mass flow rate and energy exchanges [36]. Levy et al. [11] developed this analysis for a constant wall heat flux, and

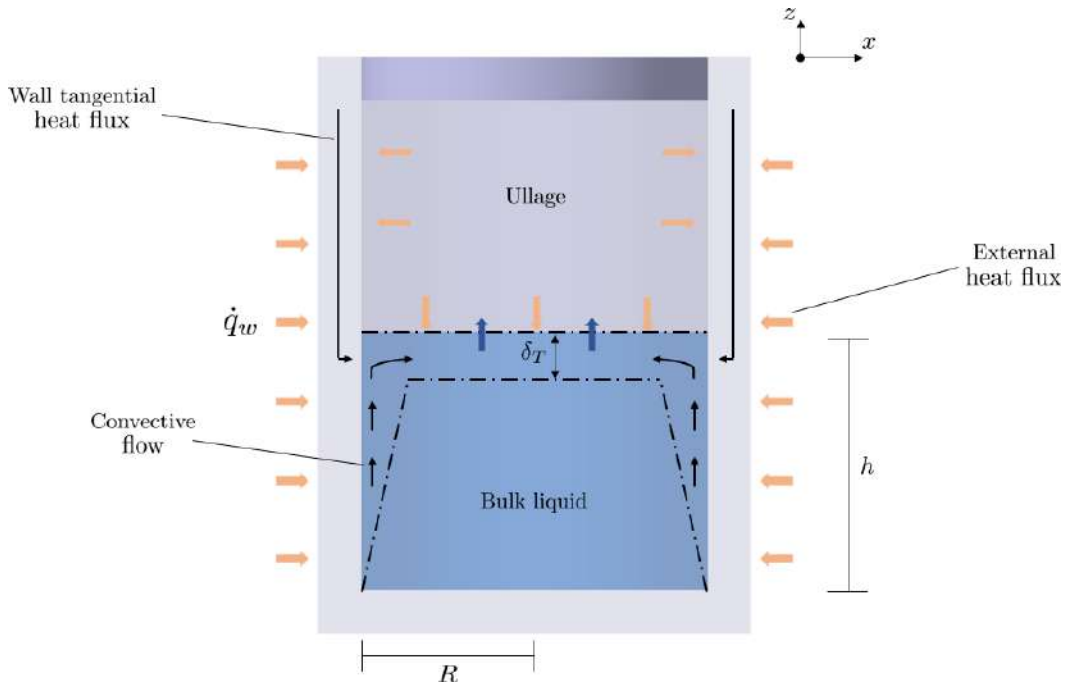

Figure 2.8: Formation of thermal stratification in a liquid due to natural convection and conduction for a closed reservoir.

concerning a laminar natural convection boundary, the following equation was derived.

$$\delta_T(t) = h - h\left(1 - 0.62\frac{\nu t}{Rh}\frac{\mathrm{Gr}^{*1/5}}{\mathrm{Pr}^{0.388}}\right)^5 \tag{2.13}$$

Where $\nu = \mu/\rho$ is the liquid kinematic viscosity given by the ratio of dynamic viscosity to density and $\mathbf{Gr}^*$, depicted in equation 2.14, represents the modified Grashof number which defines the ratio of buoyancy to viscous force.

$$\mathrm{Gr}^* = \frac{g\beta\dot{q}_w R^4}{k\nu^2} \tag{2.14}$$

The modified Grashof number takes into account the area-specific external heat flux, $\dot{q}_w$, and the liquid thermal conductivity k, for the characteristic length R. Furthermore, it considers the liquid thermal expansion coefficient β defined by the following equation,

$$\beta = \frac{1}{v}\left(\frac{\partial v}{\partial T}\right)\bigg|_p = -\frac{1}{\rho}\left(\frac{\partial \rho}{\partial T}\right)\bigg|_p \tag{2.15}$$

where v stands for the specific volume and the derivative's subscript p denotes that the pressure remains constant during the expansion. Moreover, the β coefficient is of paramount importance for the derivation of the liquid's momentum equation under the Boussinesq

approximation (section 3.1).

Equation 2.13 is only valid if the liquid Prandtl number (equation 2.16) is between $1 < \mathbf{Pr} < 30$. This number depends only on fluid properties, where c_p is the specific heat capacity at constant pressure, and defines the ratio of momentum diffusivity to thermal diffusivity.

$$\mathrm{Pr} = \frac{c_p \mu}{k} \tag{2.16}$$

For a turbulent boundary layer, Levy et al. [11] derived equation 2.17.

$$\delta_T(t) = h - h\left(1 + 0.092\frac{\nu t}{Rh}\frac{1}{\mathrm{Pr}^{2/3}}\left(\frac{\mathrm{Gr}^*}{1 + 0.443\,\mathrm{Pr}^{2/3}}\right)^{2/7}\right)^{-7} \tag{2.17}$$

The turbulent relation should be employed for the case $\mathrm{Gr}^*\mathrm{Pr} > 10^{11}$, which is generally the scenario when the launcher is standing on the launch pad. This means that under gravity dominated flows, the growth rate of the fluid thermal stratified layer is achieved faster than under orbit coasting conditions, where capillarity prevails, and the stratified layer evolves accordingly to the laminar formulation [11, 36].

Concerning the energy exchange between the superheated ullage vapour and the subcooled liquid through conduction, one may resort to the formulation of a semi-infinite body, employed by Das and Hopfinger [20], and Ludwig et al. [27]. A semi-infinite solid is an idealised body having a single planar surface that extends to infinity in all directions. This idealised body is used to demonstrate that temperature changes in the region near the surface are produced by thermal conditions on a single surface [37, 39]. This formulation allows evaluating the transient evolution of the temperature near the free surface (Figure 2.8) from the one-dimensional heat conduction equation 2.18 with no heat generation and constant thermal conductivity.

$$\frac{\partial T}{\partial t} = \alpha \frac{\partial^2 T}{\partial z^2} \tag{2.18}$$

The property α defined by equation 2.19 is the thermal diffusivity of the liquid and repre-

sents a measure of how fast heat propagates through the medium.

$$\alpha = \frac{k}{\rho c_p} \tag{2.19}$$

The semi-infinite body assumption solution is given by equation 2.20, for the case in which the semi-infinite media is at T_i and its surface is brought to the temperature T_s and maintained at that value at all times. With erfc as the complementary error function, defined as $\mathrm{erfc}(z) = 1 - \mathrm{erf}(z)$ [37].

$$\frac{T(z,t) - T_i}{T_s - T_i} = \mathrm{erfc}\left(\frac{z}{2\sqrt{\alpha t}}\right) \tag{2.20}$$

Due to conduction, the thickness of the stratified layer is evaluated through the semi-infinite body assumption and determined analytically by the following equation,

$$\delta_T(t) = C\sqrt{\alpha t} \tag{2.21}$$

where C is a constant acquired by evaluating where the erfc function tends to zero in equation 2.20 and for the present research considered to be $C = 4$. Bear in mind that different correlations may be found in the literature contingent on the applied analogy [16, 20, 27].

To summarise, the strong thermal gradient near the free surface combines natural convection and conduction. Convective flows are dominant in cryogenic fluids and the evolution of the thermal boundary layer is defined by equations 2.13 and 2.17 [31]. For non-cryogenic fluids, where both walls and liquid are nearly at the same temperature, conduction between the ullage gas and the liquid surface takes a predominant role, and the time progression of the thermal boundary layer is defined by equation 2.21.

2.3 Sloshing induced thermal destratification

In the previous section 2.2 the fundamentals that describe the settlement of a thermal stratified layer near the interface in orbital launch vehicles tanks was introduced. The mechanisms that transport heat to the interface were clarified, but no coupling with the sloshing dynamics was made. Critically, free surface slosh motion enhances these mech-

anisms, and its impact must be evaluated.

Initially, a thermal stratified layer characterised by a very steep thermal gradient settles near the interface by means of natural convection and conduction. Therefore, the liquid is branched into a warm area extending from the interface until a depth δ_T and a subcooled section defined by a quasi-homogeneous condition. Sloshing, due to dynamic perturbations, induces thermal destratification, forcing the liquid in the thermal boundary layer to be efficiently mixed with subcooled liquid from the bulk, lowering the temperature at the free surface. Once sloshing comes to an end, a thicker boundary layer δ'_T characterised by a smoother temperature gradient arises.

The sloshing induced thermal destratification can be visualised by extracting the temperature profiles previous to sloshing initialisation and once sloshing stops. Thus, a schematic representation of the profiles from the experiments of Lacapere et al. [19] is depicted in Figure 1.2.

Hereupon, it is clear that sloshing induces a bulk motion to the liquid, which augments the heat transfer. Hence, in contrast to the mechanisms that create the thermal stratification, this is defined as forced convection since the fluid is compelled to flow inside the tank by external means [37].

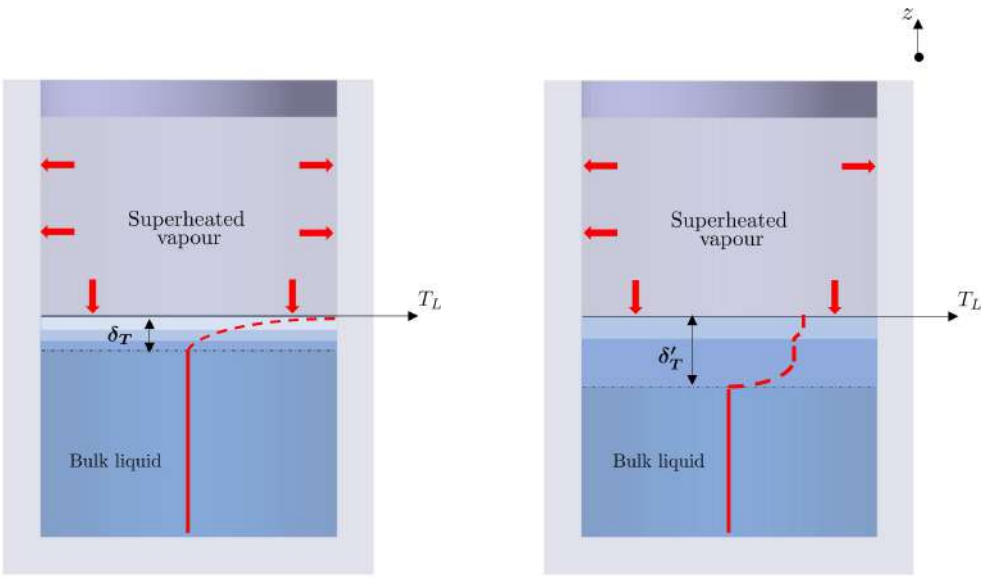

(a) Thermal profile before sloshing initialisation. (b) Thermal profile after sloshing induced mixing.

Figure 1.2: Schematic representation of the evolution of vertical temperature profiles and the thickness of thermal boundary layers in the liquid's uppermost region adapted from Lacapere et al. (2009) [19].
(repeated from page 4)

It is quite challenging to obtain simple analytical solutions for convection phenomenon from the governing equations. Thus heat transfer relations are based on empirical correlations built from experimental studies via the Nusselt number. This dimensionless parameter defines the ratio of convective to conductive heat transfer and is usually represented with reasonable accuracy by a simple power-law relation of the following form:

$$\mathrm{Nu} = B\left(\mathrm{Re}^{n}\,\mathrm{Pr}^{m}\right) \tag{2.22}$$

The B parameter is a constant, m and n are constant exponents (usually between 0 and 1) and **Re** is the Reynolds number, which defines the ratio of inertial forces to viscous forces and characterises the flow regime. Ludwig et al. [27], following the power-law equation 2.22, defined an empirical correlation from experimental data [20, 26] for the thermal destratification given by equation 2.23.

$$\mathrm{Nu}_s = \frac{\mathrm{Re}_s^{0.69}\,\mathrm{Pr}^{1/3}}{\left(\mathrm{Re}_{s_c}\right)^{0.69}} \tag{2.23}$$

The $\mathbf{Re}_s$ defines the sloshing Reynolds number obtained from equation 2.24, and $\left(\mathrm{Re}_S\right)_c = 4.0{\cdot}10^3 \pm 20\%$ is the critical Reynolds number below which sloshing does not induce significant thermal destratification. As such, for this correlation $B = 1/\mathrm{Re}_{s_c}^{0.69}$ and b represents the wave amplitude.

$$\mathrm{Re}_s = \frac{\omega}{\omega_{11}}\left(\frac{b}{R}\right)^2 \frac{\left(gR^3\right)^{1/2}}{\nu}\sqrt{\xi_{11}} \tag{2.24}$$

The Nusselt number definition can be further extended by introducing it as a ratio between the effective diffusion coefficient α_e and the liquid thermal diffusivity α without losing its meaning [20]. This relation is showcased in equation 2.25.

$$\mathrm{Nu}_s = \frac{\alpha_e}{\alpha} \tag{2.25}$$

All in all, by resorting to the empirical equation 2.23 and introducing the former definition one arrives to equation 2.26.

$$\alpha_e = \alpha\frac{\mathrm{Re}_s^{0.69}\,\mathrm{Pr}^{1/3}}{\left(\mathrm{Re}_{s_c}\right)^{0.69}} \tag{2.26}$$

Consequently, considering that the penetration length of the thermal stratified layer under sloshing may still be defined through equation 2.21, the overall thickness for the thermal boundary layer is set by the following formulation, accounting for the contributions of the initial thermal stratification and the sloshing-induced mixing phenomenon.

$$\delta_T'(t) = C\sqrt{\alpha \Delta t_{\text{init}} + \alpha_e \Delta t_{\text{s}}} \tag{2.27}$$

Where Δt_{init} represents the time at which sloshing is introduced, or more generally, the pressurisation/ramp and hold time for a laboratory experiment. Additionally, Δt_{s} depicts the sloshing excitation period until the maximum rate of pressure drop is reached [27].

2.4 Pressure drop

The pressure drop effect is a thermodynamic phenomenon in orbital launch vehicle tanks. It arises from the coupling between sloshing dynamics and heat and mass transfer mechanisms amid the superheated ullage vapour and the subcooled liquid at the free surface. This section aims to develop on this topic, which is the main objective of the present research.

Briefly stating from the results of previous research performed on the topic [16, 19, 26], the main trigger behind pressure fluctuations inside orbital launch vehicles tanks is the enhancement of heat and mass transfer mechanisms across the interface due to sloshing. As the launcher ascents to orbit, it will overcome distinct external perturbations that arise mainly from aerodynamic forces (e.g. wind gusts), generating sloshing. This slosh motion will break the equilibrium state at the interface since it enhances the mixing between the cold bulk liquid and the warmer liquid at the free surface that is in direct contact with the hot ullage vapour. Once this equilibrium is broken, the system will seek a new stable state, and due to the cooling effect, vapour will condensate. Likewise, contingent on the thermal stratification, a temperature decrease across the ullage will occur. Thus, the two premises behind the observation of the characteristic pressure drop are: (a) effective pressurisation of the tank to develop a thermal stratified liquid layer near the interface (section 2.2); (b) external perturbation that induces the liquid to slosh, leading to a thermal destratification (section 2.3).

Hereupon, the general variables that define the extent of the pressure drop when a pressurised vessel is subjected to sloshing are as follows [19, 26]:

1. **Sloshing regime** is defined by a given frequency and amplitude of slosh excitation, accordingly to Miles' weekly nonlinear theory (section 2.1.2). Understandably, chaotic and swirl regimes outlined by high amplitude free surface responses, compared to a planar motion, lead to enhanced thermal mixing and, consequently a more considerable pressure drop.

2. **Pressurisation technique and pressurant type:**

   - *Self-pressurisation* is whenever the tank is pressurised by the parasitic heat flow that continually seeps into the system. Heat is introduced into the liquid and leads to evaporation at the liquid's surface and, as a result, a rise in tank pressure. It leads to a more homogeneous temperature distribution across the liquid and, consequently, a reduced pressure drop. It is worthy to note that this method is highly time-consuming, especially for non-cryogenic experiments where the liquid is nearly at the ambient temperature.
   - *Active pressurisation* is when the working fluid, in its gaseous form, is injected in the pressure vessel through an external system. This method allows to quickly attain the desired pressure in the ullage, and build a sharp thermal gradient near the interface, leading to a more significant pressure drop.
   - *Non-condensable gas active pressurisation* employs active pressurisation principles but resorts to a non-condensable gas, such as helium. Since the pressurant does not condensate, the pressure drop phenomenon is minimised in such systems.

3. **Ullage volume** is defined by the amount of free liquid space in the dewar. The most significant pressure drop occurs at the smallest ullage volume because there is less ullage mass to maintain tank pressure. In other words, ullage pressure is more susceptible to interfacial condensation at smaller ullage volumes.

To model the pressure drop effect one may resort to the ideal gas approximation to describe the behaviour of the ullage vapour. The ideal gas model assumption, equation 2.28, is valid as long the gas pressure is small relative to the critical pressure p_c and/or the tem-

perature is large relative to the critical temperature T_c [39].

$$p_{_U} = \rho R_s T \tag{2.28}$$

In equation 2.28 vapour pressure p_U is a function of density ρ and temperature T. Additionally, R_s outlines the specific gas constant defined as $R_s = \bar{R}/M$ where $\bar{R}$ is the universal gas constant, and M is the molar mass of the gas. Therefore, the pressure drop in a gas arises from a gas temperature decrease, a gas density decrease, or both. Thus, the rate of pressure change in the system, defined by equation 2.29, may be obtained by applying the chain rule to equation 2.28 since $p_{_U} = f(\rho, T)$.

$$\frac{dp_{_U}}{dt} = \underbrace{\frac{d\rho}{dt} R_s T}_{\rho(t)} + \underbrace{\rho R_s \frac{dT}{dt}}_{T(t)} \tag{2.29}$$

Consequently, the pressure drop may be computed as a combination between $\rho(t)$ and $T(t)$. For a closed system, $\rho(t)$ represents the pressure drop fraction produced by condensation, while $T(t)$ describes the pressure drop fraction generated by sloshing cooling the ullage.

As initially introduced, the primary mechanism behind the characteristic pressure drop arises from condensation at the liquid-vapour interface due to the large amplitude waves, meaning the $T(t)$ term in equation 2.29 has a marginal impact in the overall phenomenon. This conclusion was retrieved from the analysis developed by Van Foreest [16], in which both self-pressurisation and active pressurisation tests with LN_2 were assessed. In self-pressurisation test cases, the rate of temperature change at the point of maximum pressure drop rate was zero, meaning condensation is the main mechanism to describe pressure drop. On the other hand, in the active pressurisation test cases, the contribution of the temperature change on the pressure drop rate was in the order of $10-20\,\%$, depending on the pressure of the ullage at sloshing initialisation.

The vapour condensation phenomenon might be modelled by assuming that the free surface is at saturation conditions. This is because fluid can undergo phase change in such conditions where liquid and vapour coexist. Under these conditions, the free surface temperature is equal to the saturation temperature, $T_L = T_U = T_i = T_{\text{sat}}$, which is coupled to

the vapour partial pressure p_U (equation 2.30).

$$T_i = T_{\text{sat}}\left(p_U\right) \tag{2.30}$$

The coupling between the saturation temperature T_{sat} and the pressure of the ullage vapour is defined by the Clausius-Clapeyron equation 2.31.

$$\ln\left(\frac{p}{p_{\text{ref}}}\right) = \frac{\Delta h_v}{R_s}\left(\frac{1}{T_{\text{sat,ref}}} - \frac{1}{T_{\text{sat}}}\right) \tag{2.31}$$

It provides the temperature T dependence of a fluid's saturation pressure p along the liquid–vapour coexistence curve, considering the vapour behaves as an ideal gas (equation 2.28) and the latent heat of vaporisation Δh_v is constant [40]. In the Clausius-Clapeyron law p_{ref} and $T_{\text{sat,ref}}$ define a reference known point in the saturation curve, for example the state after pressurisation [14], while p and T_{sat} specify a new point of interest.

Figure 2.9 displays a qualitative representation of a saturation curve under equation 2.31. After pressurisation, point (a) is reached where the liquid-vapour interface is in a saturation state defined by the pressure p_{ref} and temperature $T_{\text{sat,ref}}$. The liquid bulk is subcooled, and the vapour is superheated, except at the free surface. As sloshing unfolds, the subcooled bulk liquid will reach the interface and cool it down, breaking the thermodynamic equilibrium. Ergo, the temperature at the interface decreases, meaning, ac-

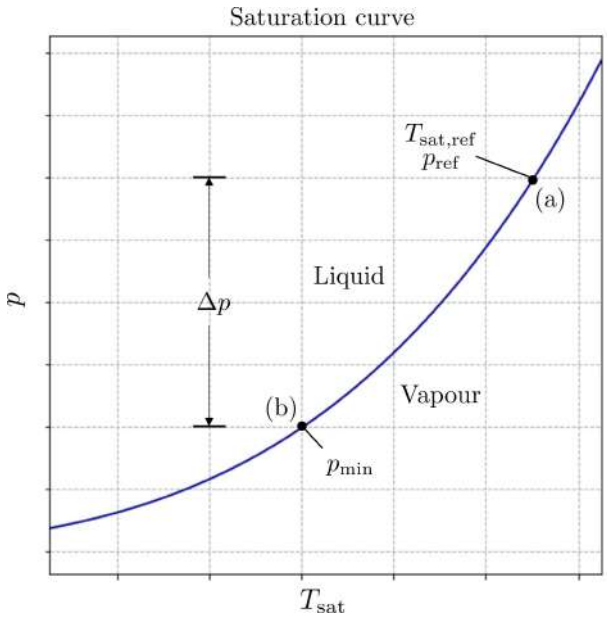

Figure 2.9: Qualitative saturation curve generated by the Clausius-Clapeyron law for the equilibrium at the free liquid surface.

cording to equation 2.31, that for the new saturation temperature, the pressure must decrease as well, and point (b) is reached. Nevertheless, the ullage pressure is superior to the saturation pressure corresponding to the new temperature at the free surface. Consequently, ullage vapour condensation takes place, leading to the characteristic pressure drop $\Delta p = p_{\text{ref}} - p_{\text{min}}$.

2.4.1 Liquid-vapour phase change

To evaluate the phase change rate at the liquid-vapour interface and characterise condensation and evaporation, one might resort to the classical kinetic theory of gases [41]. This theory is a statistical description of gas behaviour and has served as the foundation for simulating liquid-vapour phase transition in non-isothermal cryogenic sloshing [42]. It considers that the vapour near the liquid-vapour interface may be approximated as an ideal gas (equation 2.28), and the vapour molecules' velocity distribution follows a Maxwell Boltzmann distribution. Therefore, the mass flux can be expressed by the following equation,

$$j_U = \rho_U \sqrt{\frac{k_b T_U}{2\pi M}} \tag{2.32}$$

where ρ_U, k_b, M, and T_U are vapour density, Boltzmann constant, molar mass, and vapour temperature, respectively, and the subscript U denotes the vapour phase.

In equilibrium, the condensation flux equals the evaporation flux, $j_U = j_L$. The liquid-vapour system is saturated (equation 2.30), and there is no temperature jump across the interface. The equilibrium vapour density equals the vapour saturation density at the associated saturation temperature. Hence, when sloshing unfolds and breaks the equilibrium, a net phase change is defined as a difference between the condensation and evaporation fluxes.

Considering that across the vapour phase, the changes in temperature and density are negligible and resorting to the ideal gas assumption, the area-specific net phase change J may be approximated by the Hertz-Knudsen equation 2.33.

$$J = \bar{\sigma} \sqrt{\frac{M}{2\pi \bar{R}}} \left(\frac{p_i}{\sqrt{T_i}} - \frac{p_U}{\sqrt{T_U}} \right) \tag{2.33}$$

Where p_i and T_i are the pressure and temperature at the liquid interface, p_U and T_U are the vapour pressure and temperature, and $\bar{\sigma}$ represents the accommodation coefficient, which specifies the frequency at which the liquid/vapour phase transition occurs. This parameter is a multiplier on the kinetic theory phase change rate that takes into account the deviation from the theoretical maximum, due to reflection of the vapour molecules at the interface which do not undergo phase change.

Applying equation 2.33 to the characteristic pressure drop that takes place due to condensation, as described by Figure 2.30, under point (a), there is no net phase change. However, once the thermal equilibrium is broken, the vapour pressure p_U is superior to the saturation pressure at the interface p_i, meaning a negative net mass flux J will arise until equilibrium is reached as defined by point (b).

Chapter 3

Scaling analysis for gravity dominated non-isothermal sloshing

Up until now, the fundamental theoretical background of gravity dominated non-isothermal sloshing has been described. From sloshing dynamics to heat and mass transfer, one can picture throughout sections 2.1.1 to 2.4.1 that the problem in our hands is reasonably complex to scrutinise and analytical solutions impractical to be achieved. Therefore, the present section aims to develop a scaling analysis from which the dimensionless numbers (section 3.5) that characterise the problem are retrieved. This analysis is a premise for the similarity study conducted in section 3.6.

A scaling analysis is the most convenient method to scale the actual quantities, in this case, a full-size orbital launch vehicle cryogenic fuel tank, into laboratory size experiments. Developing a ground-test facility geometrically identical to the actual tank is not feasible. Thus, for the present research, a small scale model (section 4.1.2) is used to study the thermodynamic side effects of sloshing. Additionally, safety constraints do not allow to use the legitimate fuels, and oxidisers [2] meaning the experimental working fluid must attain properties that would enable the similarity analysis to converge.

From this study, the output is a set of dimensionless numbers that minimise the amount of variables required for problem description and reveal which ratios dominate the problem. Furthermore, they reduce the amount of experimental data, support the development of empirical correlations and allow to establish an order of magnitude comparison between both facilities by similarity. Hence, there are two possible approaches [43]: (a) dimensional analysis (DA) through the Buckingham Pi-theorem; (b) scaling of equations (SE) by defining the governing equations of the problem. The scaling of equations (SE) method was selected for the present research. It starts with the definition of the basic equations and boundary conditions that govern the problem, from which the relevant quantities are directly extracted [44]. Critically, if one is unable to do such, the DA approach must be chosen, where the relevant quantities are picked in the place of establishing the governing equations.

As depicted by Figure 2.1 the present problem is defined by a liquid and a vapour phase. Therefore, the governing equations for the liquid and vapour are set in section 3.1 and 3.2, respectively, and defined by the three classical transport equations for a single-species system. Moreover, since it is a two-phase problem, an interface exists, and appropriate boundary conditions must be defined. Therefore, a mass, momentum, and energy balance at a non-flat liquid-vapour interface is defined in section 3.3. Finally, the boundary conditions that account for heat transfer at the walls and a sloshing external sinusoidal disturbance are presented in section 3.4.

3.1 Governing equations for the liquid phase

The liquid phase is considered to be a single-species system and modelled as an incompressible fluid, where density is deemed to be constant ($\rho_L = \rho_{\text{ref}}$) [44]. These assumptions yield equation 3.1 for the mass conservation,

$$\nabla \cdot \mathbf{V}_L = 0 \tag{3.1}$$

where $\mathbf{V} = (u_x, v_y, w_z)$ is the flow velocity vector and $\nabla = \left(\frac{\partial}{\partial r}, \frac{1}{r}\frac{\partial}{\partial \theta}, \frac{\partial}{\partial z}\right)$ is the nabla operator in cylindrical coordinates. For the linear momentum balance, the fluid is assumed to be Newtonian. Thus, viscous stresses are proportional to the element strain rates and viscosity coefficient. The Boussinesq approximation was employed, considering the temperature and density variations occurring in this thermal convection problem are processed at practically constant pressure, consequently manifesting, in Navier-Stokes equation 3.2, only through the mass forces term [45]. As such, $\rho_L = \rho_{\text{ref}}$ except in the buoyancy term of the momentum balance where $\rho = \rho_{\text{ref}} - \rho_{\text{ref}}\,\beta\,(T_L - T_{\text{ref}})$.

$$\rho_{\text{ref},L}\left(\frac{\partial \mathbf{V}_L}{\partial t} + (\mathbf{V}_L \cdot \nabla)\mathbf{V}_L\right) = -\nabla p_L + \mu_L \nabla^2 \mathbf{V}_L + \rho_{\text{ref},L}\mathbf{g} - \rho_{\text{ref},L}\beta\,(T_L - T_{\text{ref},L})\,\mathbf{g} \tag{3.2}$$

Concerning the conservation of energy, it is assumed that there is no radiation heat transfer and heat flow follows Fourier's law of heat conduction [39]. The kinetic energy contribution is neglected, and the total energy balance turns into the internal energy $\hat{u}_L$ equation 3.4. Additionally, the internal specific energy is expressed by the heat capacity for

constant pressure c_p, by the following equation.

$$d\hat{u}_{_L} \approx c_p dT \tag{3.3}$$

It takes into account the limited, but not negligible, compressibility of liquids (for complete derivation resort to [16]).

$$\rho_{\mathrm{ref},L} c_{p,L} \left(\frac{\partial T_L}{\partial t} + \mathbf{V}_L \cdot \nabla T_L \right) = k_L \nabla^2 T_L \tag{3.4}$$

3.2 Governing equations for the gas phase

For the vapour phase, the general compressible flow formulation is employed, and the vapour was considered to behave as an ideal gas (equation 2.28). The compressible mass balance for this phase is given by equation 3.5 and the compressible linear momentum through equation 3.6. The vapour phase was assumed to be a Newtonian fluid with constant dynamic viscosity μ. Moreover, Stokes' hypothesis was introduced where the bulk viscosity is set to zero [46]. This interpretation is usually employed in the study of low Mach-number, variable-density flows and renders the mathematical treatment of compressible flows considerably easier [47].

$$\frac{\partial \rho_U}{\partial t} + \nabla \cdot (\rho_U \mathbf{V}_U) = 0 \tag{3.5}$$

$$\frac{\partial (\rho_U \mathbf{V}_U)}{\partial t} + \nabla \cdot (\rho_U \mathbf{V}_U \mathbf{V}_U) = -\nabla p_U + \mu_U \nabla^2 \mathbf{V}_U + \frac{1}{3} \mu_U \nabla (\nabla \cdot \mathbf{V}_U) + \rho_U \mathbf{g} \tag{3.6}$$

For energy conservation, the kinetic energy contribution was neglected. Consequently, as for the liquid phase in equation 3.4, the balance illustrates the conservation of internal energy $\hat{u}_{_U}$ instead of total energy. Additionally, by introducing the ideal gas idealisation of equation 2.28 the relation between internal energy and temperature is given by the following approximation,

$$d\hat{u}_{_U} \approx c_v dT \tag{3.7}$$

where c_v represents the heat capacity for constant volume [39, 48]. Moreover, viscous

dissipation was considered limited and neglected, resulting in the final equation 3.8 for the internal energy.

$$\frac{\partial}{\partial t}\left(\rho_U c_{v,U} T_U\right) + \nabla \cdot \left(\rho_U c_{v,U} \mathbf{V}_U T_U\right) = \nabla \cdot \left(k_U \nabla T_U\right) - \nabla \cdot \left(p_U \mathbf{V}_U\right) \tag{3.8}$$

3.3 Governing equations for the interface

The above-mentioned phase equations can be applied within each phase and up to an interface. However, they are not valid across the interface, where there are dramatic changes in several properties. In order to solve the governing equations for heat, mass, and momentum transfer in the two neighbouring phases, appropriate boundary conditions at the interface must be supplied. These must be derived through integral relations for a control volume, and the complete derivation may be found in Faghri and Zhang [49] and Dreyer [50].

At a liquid-vapour interface, the mass balance is given by the following equation,

$$\dot{m}''_\delta = \rho_L \left(\mathbf{V}_L - \mathbf{V}_i\right) \cdot \mathbf{n} = \rho_U \left(\mathbf{V}_U - \mathbf{V}_i\right) \cdot \mathbf{n} \tag{3.9}$$

where $\dot{m}''_\delta$ is the area-specific mass flux at the interface due to phase change. $\mathbf{V} \cdot \mathbf{n}$ denotes the velocity in the free surface normal direction. $\mathbf{V}_i$, $\mathbf{V}_L$ and $\mathbf{V}_U$ define the velocity of the interface, liquid and gas phase, respectively.

The integral momentum equation for a control volume containing two phases separated by an interface is given by equation 3.10. The surface tension σ is constant, the liquid and vapour phases are considered inviscid ($\boldsymbol{\tau}_L = \boldsymbol{\tau}_U = 0$), and the evaporation or condensation rate is neglected. The result is known as the Young-Laplace equation,

$$p_U - p_L = \Delta p_i = -\sigma \left(\frac{1}{R_I} + \frac{1}{R_{II}}\right) \tag{3.10}$$

where R_I and R_{II} specify two radii of curvature to describe an arbitrarily-curved surface and Δp_i the pressure difference across the interface.

The energy conservation at the liquid-vapour interface is expressed by equation 3.11, con-

sidering that the change in the kinetic energy across the interface is negligible.

$$(k_U \nabla T_U - k_L \nabla T_L) \cdot \mathbf{n} = \dot{m}''_\delta \Delta h_v \tag{3.11}$$

3.4 Boundary conditions

Until now, the main governing equations of the problem have been overviewed. Nevertheless, it is mandatory for the scaling of equations approach to non-dimensionalise the boundary conditions. Additionally, for the sake of completeness, other relevant phenomenons that have a direct impact on the research are here introduced.

The external disturbance that induces forced sloshing motion to the free surface is harmonic and given by the following equation.

$$X(t) = A_f \sin(\omega t) \tag{3.12}$$

The container walls are solid and impermeable. Therefore the no-slip condition applies (equation 3.13). Additionally, the normal component of the fluid's velocity w at the free surface η equals the normal component of the free surface velocity (equation 3.14) so that no holes appear between liquid and gas [44].

$$\mathbf{V}_L = \mathbf{V}_U = \mathbf{V}_{\text{wall}} \tag{3.13}$$

$$w_{z_L} = w_{z_U} = \frac{d\eta}{dt} \tag{3.14}$$

The liquid and vapour temperatures at the interface must be the same, a condition required by equation 2.30, which is directly correlated with the Clausius-Clapeyron law 2.31, considering the vapour behaves as an ideal gas.

Because of the no-slip and no temperature jump conditions at the walls, heat transfer between solid and fluid at the solid surface occurs via pure conduction. This results in equations 3.15 and 3.16 by setting the Fourier's law equal to Newton's law of cooling for the liquid and vapour phases, respectively.

$$\dot{q}_{L,w} = -\, k_L \frac{\partial T_L}{\partial r}\bigg|_{r=R} = \bar{h}_L \left(T_w - \bar{T}_L\right) \tag{3.15}$$

$$\dot{q}_{U,w} = -\, k_U \frac{\partial T_U}{\partial r}\bigg|_{r=R} = \bar{h}_U \left(T_w - \bar{T}_U\right) \tag{3.16}$$

$\bar{h}$ is the experimentally measured convection heat transfer coefficient, T_w is the temperature of the solid surface, and $\bar{T}$ is the temperature of the fluid sufficiently far from the surface. For the liquid $\bar{T}_L$ corresponds to the bulk temperature.

Lastly, heat conduction across the walls arises as one of the most critical factors during the initial thermal stratification, as analysed in section 2.2. Hereupon, one must consider the heat conduction equation 3.17:

$$\frac{\partial T}{\partial t} = \alpha \nabla^2 T \tag{3.17}$$

where α defined by equation 2.19 is the thermal diffusivity of the reservoir walls material.

3.5 Dimensionless numbers

Throughout sections, 3.1 to 3.4, the governing equations of the gravity-dominated non-isothermal sloshing problem have been formulated, and the boundary conditions and relevant phenomenons are introduced. Therefore, to extract the dimensionless numbers through the scaling of equations method, the following four steps approach should be employed:

1. Identify variables and constants, then define the generic non-dimensional quantities, focusing on variables only;
2. Incorporate the non-dimensional values into the governing equations and boundary conditions;
3. Develop the equations until the non-dimensional format is attained and the dimensionless numbers are extracted;
4. Appoint reference parameters that characterise the problem and correlate the final numbers with existing dimensionless numbers.

For the incompressible liquid phase (section 3.1), the relevant variables are the spacial coordinates, velocity, time, pressure, temperature and acceleration. These variables, in

the following equation 3.18, are made dimensionless by dividing through the relevant parameters and indicated by hat symbols:

$$\hat{\nabla} = L_c \nabla, \quad \hat{\mathbf{V}} = \frac{\mathbf{V}}{b\omega}, \quad \hat{t} = \frac{tb\omega}{L_c}, \quad \hat{p} = \frac{p}{\rho_{\text{ref}}(b\omega)^2}, \quad \hat{T} = \frac{T - T_{\text{ref}}}{\Delta T}, \quad \hat{\mathbf{g}} = \frac{\mathbf{g}}{g}. \tag{3.18}$$

The characteristic length scale is L_c, and the spatial derivatives are hidden in the nabla operator ∇. The characteristic velocity is $b\omega$, in which b defines the sloshing wave amplitude and ω the imposed frequency or angular velocity. The characteristic acceleration is the gravitational acceleration g, the characteristic temperature difference is ΔT, and the pressure scale is described by the dynamic pressure $\rho_{\text{ref}}(b\omega)^2$ since sloshing is a purely dynamic effect.

According to the expressions in equations 3.1 to 3.4, and the former scaling factors from equation 3.18 the corresponding characteristic numbers for the liquid phase are summarised in Table 3.1.

Table 3.1: Liquid phase governing equations dimensionless numbers.

Reference	Dimensionless number	Expression	Definition	Equation
Π_1	$\mathbf{Fr}_L$	$\frac{(b\omega)^2}{gL_c}$	$\frac{\text{Inertia}}{\text{Gravity}}$	3.2
Π_2	$\mathbf{Re}_L$	$\frac{\rho_{\text{ref},L}(b\omega)L_c}{\mu_L}$	$\frac{\text{Inertia}}{\text{Viscosity}}$	3.2
Π_3	$\frac{\mathbf{Gr}}{\mathbf{Re}^2}\,L$	$\frac{g\beta\Delta T L_c}{(b\omega)^2}$	$\frac{\text{Buoyancy}}{\text{Inertia}}$	3.2
Π_4	$\mathbf{Pe}_L$	$\frac{L_c(b\omega)}{\alpha_L}$	$\frac{\text{Advection}}{\text{Diffusion}}$	3.4

From the gravity force term in equation 3.2 the Froude number (Π_1) arises and denotes the ratio between the flow inertia and the external acceleration field, for this case, expressed by gravity. $\mathbf{Fr}_L$ defines an essential effect in free surface flows and can be neglected when there is no free surface [44]. Additionally, due to the employment of the Boussinesq approximation, the Π_3 parameter, which defines a ratio between buoyancy and inertial forces, emerges. $\mathbf{Gr}_L$ / $\mathbf{Re}_L^2$ introduces the effects of combined natural and forced convection, and their relative importance [51]. Likewise, from the viscous force term in equation 3.2, the Reynolds number (Π_2) appears, defining the ratio of the inertia to viscous forces in the fluid. $\mathbf{Re}_L$ is an essential element in sloshing applications because it is directly related to the dissipated energy at the walls and free surface due to viscous boundary layers and in the liquid bulk due to viscous strains. Through equation 3.4 the Péclet number (Π_4) surfaces from the net heat flux term, and it compares the advective

heat transport rate and the molecular diffusion of heat, in other words, the ratio of heat transfer by the motion of fluid to heat transfer by thermal conduction.

For the compressible gas phase (section 3.2), the former adimensional quantities still hold, but density and thermal conductivity now arise as new variables:

$$\hat{\rho}_U = \frac{\rho_U}{\rho_{\text{ref},U}}, \quad \hat{k}_U = \frac{k_U}{k_{\text{ref},U}} \tag{3.19}$$

where the reference density is $\rho_{\text{ref},U}$ and the characteristic thermal conductivity is $k_{\text{ref},U}$. Table 3.2 summarises the gas phase characteristic numbers.

Table 3.2: Gas phase governing equations dimensionless numbers.

Reference	Dimensionless number	Expression	Definition	Equation
Π_5	$\mathbf{Fr}_U$	$\frac{(b\omega)^2}{gL_c}$	$\frac{\text{Inertia}}{\text{Gravity}}$	3.6
Π_6	$\mathbf{Re}_U$	$\frac{\rho_{\text{ref},U}(b\omega)L_c}{\mu}$	$\frac{\text{Inertia}}{\text{Viscosity}}$	3.6
Π_7	$\mathbf{Pe}_U$	$\frac{\rho_{\text{ref},U}c_{v,U}(b\omega)L_c}{k_{\text{ref}}}$	$\frac{\text{Advection}}{\text{Diffusion}}$	3.8
Π_8	$\mathbf{Ec}_U$	$\frac{(b\omega)^2}{c_{v,U}\Delta T}$	$\frac{\text{Advection kinetic energy}}{\text{Enthalpy}}$	3.8

By resorting to the compressible formulation of the momentum equation 3.6, direct buoyancy effects are now accounted in the density variable (equation 3.19) and the Grashof number (**Gr**) vanish. Additionally, from the gas internal energy equation 3.8 the Eckert number (Π_8) appears from the pressure work term and compares the kinetic energy of the flow relative to the boundary layer enthalpy difference. $\mathbf{Ec}_U$ is crucial in high-speed flows where viscous dissipation is significant, meaning for sloshing applications may be neglected [38].

Concerning the interface boundary conditions (section 3.3), the mass flux is divided by the characteristic mass flux J and the radii of curvature by L_c:

$$\hat{\dot{m}''_\delta} = \frac{\dot{m}''_\delta}{J}, \quad \hat{R}_I = \frac{R_I}{L_c}, \quad \hat{R}_{II} = \frac{R_{II}}{L_c}. \tag{3.20}$$

The extracted dimensionless numbers from the interface describe both the behaviour of the liquid and the vapour phase and are showcased in Table 3.3.

The conservation balances in the interface (section 3.3) are inherently a function of both liquid and vapour phases, as such, special care must be taken to properly identify the dif-

Table 3.3: Interface governing equations dimensionless numbers.

Reference	Dimensionless number	Expression	Definition	Equation
Π_9	$\mathbf{D}$	$\frac{\rho_{\text{ref},U}}{\rho_{\text{ref},L}}$	$\frac{\text{Vapour density}}{\text{Liquid density}}$	3.9
Π_{10}	$\frac{\mathbf{RePr}}{\mathbf{JaEv}}L$	$\frac{\rho_{\text{ref},L}(b\omega)}{J}$	$\frac{\text{Advective transport rate}}{\text{Diffusive transport rate}}$	3.9
Π_{11}	$\frac{\mathbf{RePr}}{\mathbf{JaEv}}U$	$\frac{\rho_{\text{ref},U}(b\omega)}{J}$	$\frac{\text{Advective transport rate}}{\text{Diffusive transport rate}}$	3.9
Π_{12}	$\mathbf{We}_L$	$\frac{\rho_{\text{ref},L}(b\omega)^2 L_c}{\sigma}$	$\frac{\text{Inertia}}{\text{Surface Tension}}$	3.10
Π_{13}	$\mathbf{Ev}_L$	$\frac{\Delta h_v L_c J}{k_L \Delta T}$	$\frac{\text{Released or absorbed heat}}{\text{Conductive heat transfer}}$	3.11
Π_{14}	$\mathbf{Ev}_U$	$\frac{\Delta h_v L_c J}{k_U \Delta T}$	$\frac{\text{Released or absorbed heat}}{\text{Conductive heat transfer}}$	3.11

ferent properties through the subscripts L and U. The interfacial mass balance equation 3.9 yields a total of three dimensionless numbers: the density ratio (**D**) and the Π_{10} and Π_{11} parameters, which are equal but depend on liquid and gas properties, respectively. The **RePr/JaEv** number is a function of four numbers where **Ja**=$\frac{c_p \Delta T}{\Delta h_v}$ is the Jacob number. Light can be shed in its definition by resorting to Fick's law of diffusion [37], where the diffusion coefficient is used to describe the mass flux J at the interface. Consequently, Π_{10} and Π_{11} resemble a mass transfer Péclet number at the interface, which define a comparison between the advective and diffusive transport rates.

From the Young-Laplace equation 3.10 the Weber number (**We**) is retrieved. It defines a ratio of inertia to surface tension forces. The Weber is only significant when it is of order unity or smaller, meaning the surface curvature is comparable in size to the liquid depth (e.g. in droplets and capillary flows) [11, 44]. Regarding the energy equation 3.11 the evaporation number (**Ev**) for the liquid and vapour arise [13, 14]. It compares the released/absorbed heat due to condensation or evaporation to the heat conducted across the interface due to thermal gradients.

Concerning the boundary conditions defined in section 3.4, only the harmonic sloshing excitation, the saturation condition at the interface and the consideration of the heat transfer across the walls raise dimensionless numbers, which are summarised in Table 3.4.

The amplitude ratio ($\mathbf{A}_s$) and the wave amplitude number ($\mathbf{W}_s$), which is a function of the forcing frequency ratio ω/ω_{11} in the wave amplitude b term, are of paramount importance to define the sloshing regime and are well characterised through Miles' weekly nonlinear theory defined in section 2.1.2. Concerning the Clausius-Clapeyron number ($\mathbf{Cl}_i$), it is purely a function of the saturation properties of the fluid and retrieved from the RHS of

Table 3.4: Boundary conditions dimensionless numbers.

Reference	Dimensionless number	Expression	Definition	Equation
Π_{15}	$\mathbf{A}_s$	$\frac{A_f}{L_c}$	$\frac{\text{Forcing amplitude}}{\text{Characteristic length}}$	3.12
Π_{16}	$\mathbf{W}_s$	$\frac{b}{L_c}$	$\frac{\text{Wave amplitude}}{\text{Characteristic length}}$	3.12
Π_{17}	$\mathbf{Cl}_i$	$\frac{\Delta h_v}{R_s}\left(\frac{1}{T_{\text{sat,ref}}}-\frac{1}{T_{\text{sat}}}\right)$	Clausius-Clapeyron law	2.31
Π_{18}	$\mathbf{Nu}_L$	$\frac{\bar{h}_L L_c}{k_L}$	$\frac{\text{Convective heat transfer}}{\text{Conductive heat transfer}}$	3.15
Π_{19}	$\mathbf{Nu}_U$	$\frac{\bar{h}_U L_c}{k_U}$	$\frac{\text{Convective heat transfer}}{\text{Conductive heat transfer}}$	3.16
Π_{20}	$\mathbf{Fo}_w$	$\frac{\alpha\bar{\tau}}{L_c^2}$	$\frac{\text{Diffusive transport rate}}{\text{Storage rate}}$	3.17

the non-dimensional Clausius-Clapeyron law. From the fluid-solid interaction the Nusselt number (**Nu**) appears and introduces the convection phenomenon discussed across sections 2.2 and 2.3. Lastly, the Fourier number ($\mathbf{Fo}_w$) yielding the ratio of the conductive transport rate to the quantity storage rate specifies the heat transport across the tank walls by employing a generic time scale defined as $\bar{\tau}$.

3.6 Similarity analysis

The similarity analysis can be performed with the dimensionless numbers retrieved from the governing equations and boundary conditions of our non-isothermal two-phase flow problem. The main objective of such a study is to ensure our laboratory setup (chapter 4), where HFE-7200 was used as the working fluid, can be translated to a full-size prototype, in which experiments would be unfeasible. Through similarity, the model and prototype are described by the following formal statement:

"*Flow conditions for a model test are completely similar if all relevant dimensionless parameters have the same corresponding values for the model and the prototype*" (Frank White, 1999 [44]).

Thus, in this section, the most important dimensionless numbers characterising the research are considered and depicted in Figure 3.1. As one could foresee, some numbers lose their meaning when picturing the overall sloshing dynamics problem and are hereafter disregarded. Moreover, the similarity approach was simplified into four types: geometric, kinematic, dynamic, and heat and mass transfer processes. Each is investigated

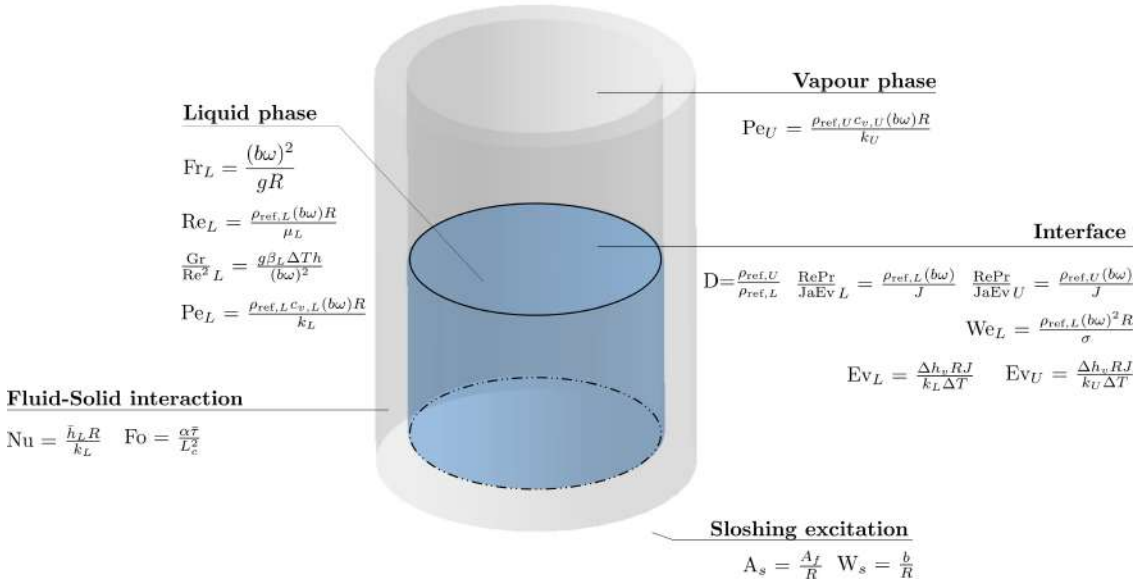

Figure 3.1: Summary of the relevant dimensionless numbers in non-isothermal sloshing applications.

separately and to compute the dimensionless numbers for dynamic (section 3.6) and heat and mass transfer (section 3.6), the planar waves sloshing excitation condition $A_f/R = 0.025, \omega/\omega_{11} = 0.80$ was fixed for the batch of working fluids: HFE-7200, HFE-7000, nitrogen (N_2) and hydrogen (H_2).

3.6.1 Geometric similarity

Geometric similarity has the primary purpose of ensuring all the body dimensions are linearly related through a geometrical scaling factor λ_{sf}. It is the first step of the similarity analysis and must be ensured ahead of any experimental testing. Any deviations from this consideration must be well evaluated and duly substantiated.

Sloshing small-scale experiments are commonly performed in circular cylindrical reservoirs, as this is the most renowned shape for orbital launch vehicle tanks [2, 52]. Consequently, the geometric similarity is accomplished based on two dimensions: radius R and height H. At VKI, sloshing experiments are carried out in a flat bottom plexiglass cell, with the full dimensions described in section 4.1.2 and here summarised in Table 3.5. The quartz cell has a radius $R = 40.5$ mm, and a total available height $H = 120$ mm. Hereupon, since no new tank will be developed for the present research, geometric similarity was employed by taking the tank's most relevant characteristic length scale (L_c), its radius R [22].

The full-size facility was established as Europe's new Ariane 6 launch vehicle, expected to attain a radius $R = 2700$ mm for the core and upper stage's cryogenic propellant tanks. This dimension follows the previous version, the Ariane 5. Therefore, from the radius ratio a scaling factor $\lambda_{\text{sf}} = 66.7$ was extracted through equation 3.21.

$$\frac{R_{\text{Ariane}}}{R_{\text{VKI}}} = \frac{H_{\text{Ariane}}}{H_{\text{VKI}}} = \lambda_{\text{scaling factor}} \tag{3.21}$$

Therefore the full-size tank must be $H = 8000$ mm. Although this is generally not true for the core stage cryogenic liquid hydrogen tanks, it is in excellent agreement with the core stage's oxidiser, and upper stage's tanks [14, 16].

Table 3.5: Laboratory model and full-size cryogenic tank dimensions.

	Radius R (m)	Height H (m)	Fill level (%)
VKI sloshing cell	0.0405	0.120	h/R>1.0
Full size facility (Ariane 6)	2.70	8.10	

Moreover, the shape of the tank bottom was also a critical element to consider under geometric similarity since most orbital launcher tanks employ concave and convex geometries for sloshing damping [30, 53]. For this reason, as discussed in section 2.1.1.1, high fill ratios $h/R \geq 1.0$ must be ensured to neglect the tank bottom geometry.

3.6.2 Kinematic similarity

Kinematic similarity demands that the model and prototype have the same length-scale and time-scale ratios. As a result, it implies that geometric similarity is met, and the velocity-scale ratio is the same for both. Frictionless flows with a free surface are kinematically similar by ensuring the wave-motion is scaled, which is achievable through the Froude number since it introduces length and time scales [44]. Hereupon, equation 3.22 establishes the kinematic similarity condition,

$$\text{Fr}_{\text{ VKI}} = \frac{(b\omega)^2_{\text{VKI}}}{gR_{\text{VKI}}} = \frac{(b\omega)^2_{\text{Ariane}}}{gR_{\text{Ariane}}} = \text{Fr}_{\text{ Ariane}} \tag{3.22}$$

where the characteristic length is the tank radius $L_c = R$. Therefore, this condition is met by establishing the same sloshing regime in both facilities, which is defined through Miles' weekly nonlinear theory (section 2.1.2). Thus, the free surface motion is fixed at the hand of dimensionless forcing amplitude A_f/R and dimensionless forcing frequency

ω/ω_{11} similarity [25, 54].

The characteristic velocity in the Froude number numerator can be expanded to equation 3.23, by introducing equation 2.6 for the wave amplitude b. Ergo, the velocity scale may be rewritten using equation 2.5 for the natural frequency ω_{11} and by fixing the dimensionless forcing frequency:

$$b\omega = 2\underbrace{\left[\frac{\left(\frac{\omega}{\omega_{11}}\right)^2}{1-\left(\frac{\omega}{\omega_{11}}\right)^2}\right]\left[\frac{\omega}{\omega_{11}}\right]}_{cte.}\omega_{11}A_f \quad (3.23) \qquad b\omega \propto \sqrt{\frac{g}{R}}A_f. \quad (3.24)$$

The retrieved characteristic velocity from equation 3.24 may be introduced in equation 3.22 leading to the following formulation for the Froude number:

$$\mathrm{Fr}_{\text{VKI}} = \mathrm{Fr}_{\text{Ariane}} \propto \left(\frac{A_f}{R}\right)^2. \quad (3.25)$$

Consequently, fixing the forcing amplitude A_f/R and the dimensionless forcing frequency ω/ω_{11} ensures kinematic similarity where the inertia and gravity effects have the same relative importance in both facilities. Moreover, this approach ensures that the amplitude ratio number ($\mathbf{A}_s$) and wave amplitude number ($\mathbf{W}_s$) are equal. Since viscosity and surface tension effects are crucial in our problem, kinematic similarity will be inherently dependent on dynamic similarity [44].

3.6.3 Dynamic similarity

Dynamic similarity is attainable when the model and prototype showcase identical force-scale or mass-scale ratios. Here the premise that the gas phase does not significantly affect the sloshing motion is employed [22]. This is due to the tremendous difference in inertia between the gas and the liquid. Therefore, the dynamic similarity of the problem is established in terms of liquid Reynolds number ($\mathbf{Re}_L$) and Weber number ($\mathbf{We}_L$).

From Figure 3.2, a difference in Reynolds number that ranges over three orders of magnitude between the experiment and the full-size application is showcased. The viscous forces have higher relative strength in the small-scale model than in the full-size facil-

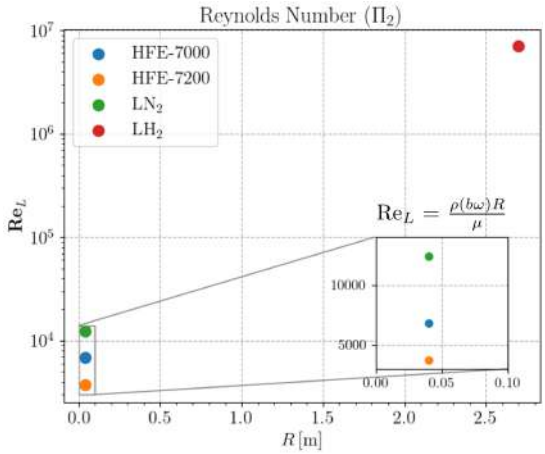

Figure 3.2: Π_2 similarity versus tank radius.

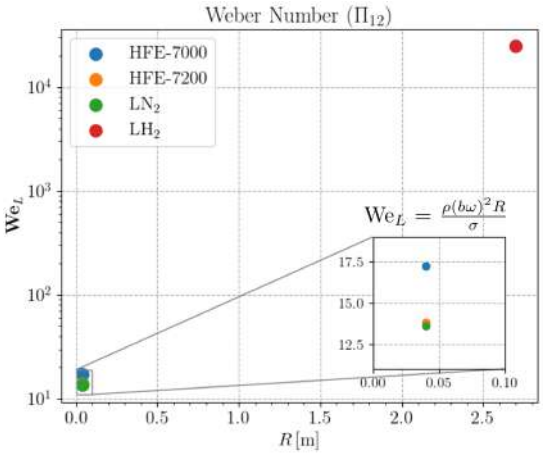

Figure 3.3: Π_{12} similarity versus tank radius.

ity. This translates into superior sloshing damping due to energy dissipation at the walls, attributable to the cell radius difference. Additionally, in Figure 3.3 the Weber number scaling demonstrates that surface tension prevails relative to inertia in the model, which is not the case for the full-size facility. Once again, due to a radius difference in the order of 10^2. However, for both cases, $\mathbf{We} \gg 1$ indicating the system is relatively unaffected by surface tension effects, and the equilibrium liquid surface is reasonably flat [55].

3.6.4 Heat and mass transfer similarity

Lastly, the heat and mass transfer similarity describes the scaling of the dimensionless numbers that define heat transfer processes and integral quantities of heat and mass transfer.

The Π_3 parameter characterises the forces that govern sloshing thermal destratification and is displayed in Figure 3.4. It is defined by setting the characteristic length as the fill level ($L_c = h$) and the thermal field as the temperature difference between the liquid and vapour reference states ($\Delta T = T_{\mathrm{ref},L} - T_{\mathrm{ref},U}$). Thus, one can conclude that the $\mathbf{Gr}/\mathbf{Re}_L^2$ ratio has the same order of magnitude between facilities and, as such

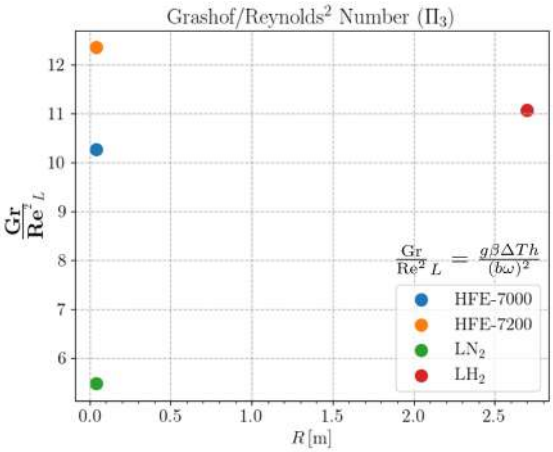

Figure 3.4: Π_3 similarity versus tank radius.

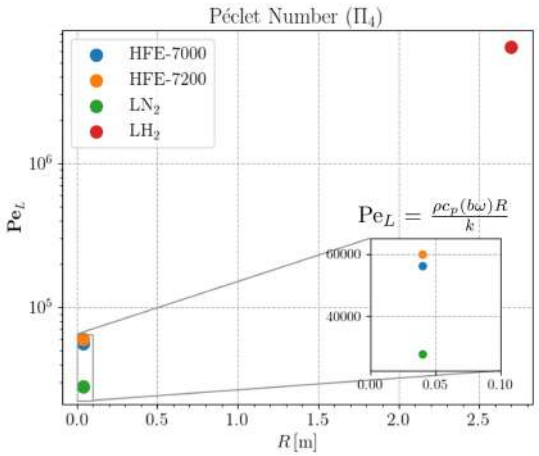

Figure 3.5: Π_4 similarity versus tank radius.

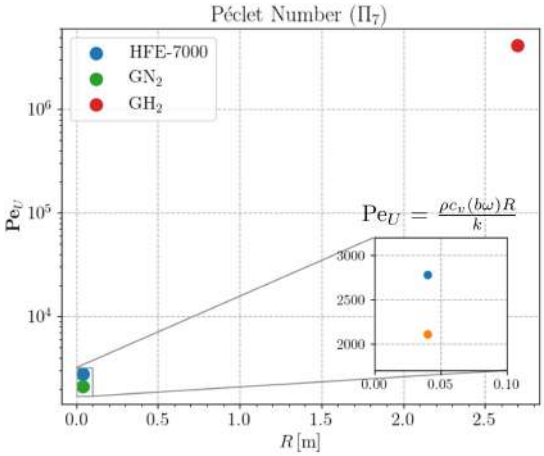

Figure 3.6: Π_7 similarity versus tank radius.

analogous buoyancy to inertia forces.

On the other hand, Figures 3.5 and 3.6 display the Péclet number (**Pe**) scaling for the liquid and gas, respectively. In both cases, thermal diffusivity dominates in the small-scale model compared to the heat transport by advection. Once again, properties diffuse due to gradients, and through diffusion the small-scale system tends to thermal homogeneity faster than the full-size facility.

For the Π_{10} and Π_{11} dimensionless numbers, the mass flux J was computed through the Hertz-Knudsen equation 2.33, considering the pressure drop corresponds to the pressure difference between the vapour and liquid reference states. The scaling in Figures 3.7 and 3.8 showcases that the order of magnitude between facilities is identical. Therefore, in both cases, the diffusive mass transport rate dominates the problem in both facilities.

The liquid evaporation number (Figure 3.9) showcases a difference that ranges over two

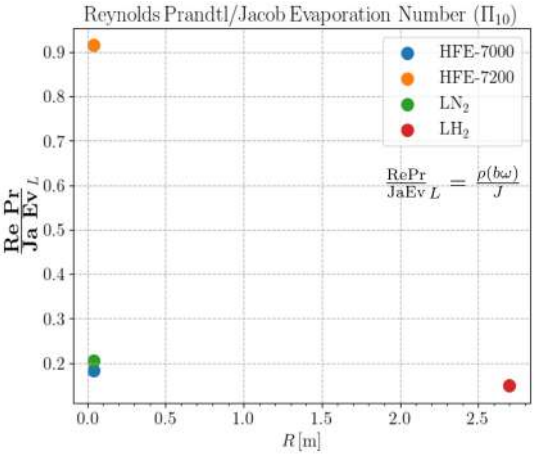

Figure 3.7: Π_{10} similarity versus tank radius.

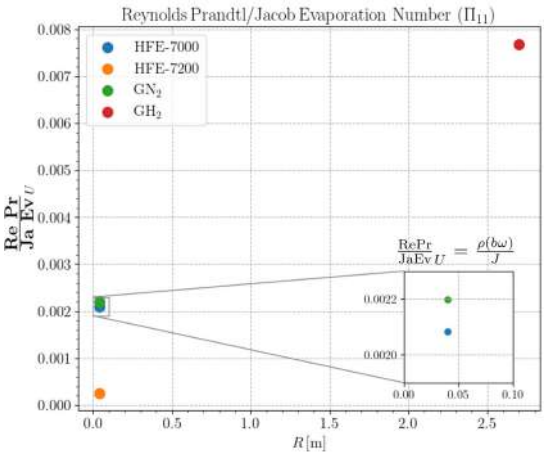

Figure 3.8: Π_{11} similarity versus tank radius.

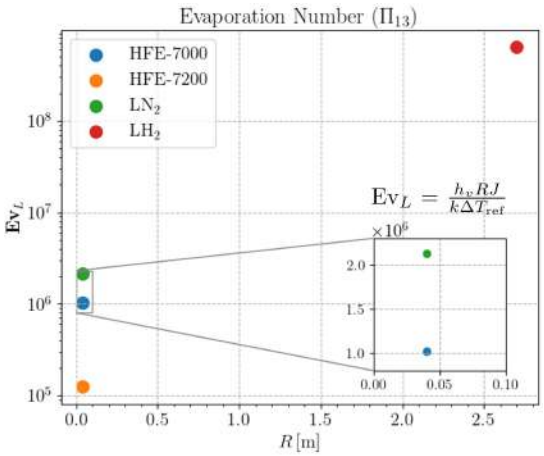

Figure 3.9: Π_{13} similarity versus tank radius.

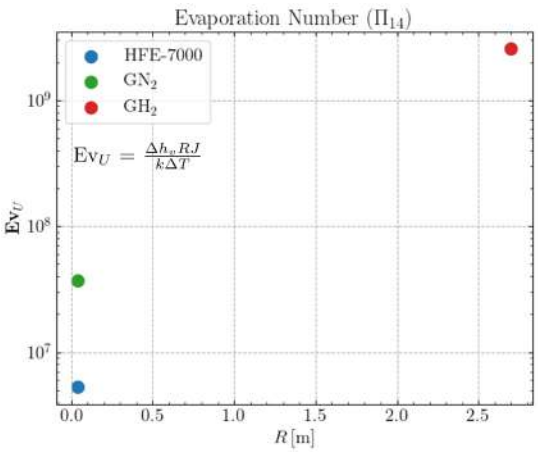

Figure 3.10: Π_{14} similarity versus tank radius.

orders of magnitude between the experiment and the full-size application, and off three decades for the gas (Figure 3.10). Here the characteristic length was set as the radius ($L_c = R$) since it best describes the mass transfer phenomenon at the interface. Evidently, it scales the magnitude of released/absorbed energy where its relative importance is superior in a larger tank. Lastly, the scaling analysis for the fluid-solid interaction regarding the liquid Nusselt number (**Nu**) and the walls Fourier number (**Fo**) is displayed in Figures 3.11 and 3.12, respectively. Here, the Nusselt number was computed according to the forced convection empirical correlation detailed in section 2.3. The Π_{18} parameter showcases that for the full-size facility, convective heat transfer has a predominant role, a consequence of less viscous dissipation, which enhances the thermal mixing phenomenon.

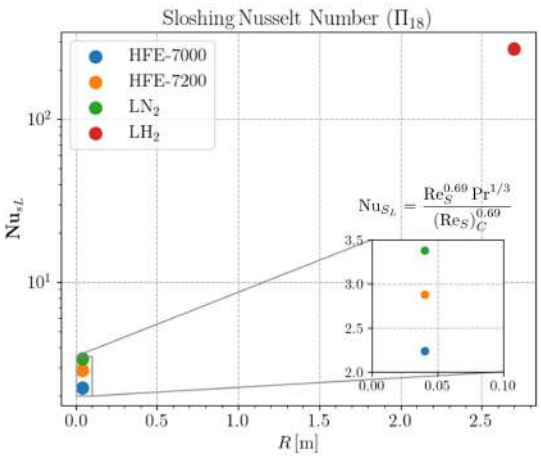

Figure 3.11: Π_{18} similarity versus tank radius.

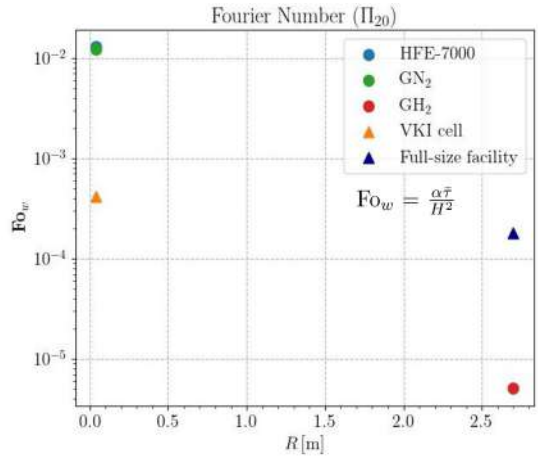

Figure 3.12: Π_{20} similarity versus tank radius.

On the other hand, the walls Fourier number was computed with the plexiglass thermal diffusivity [56] for the experimental facility and aluminium 2219 alloy for the actual tank [53]. The time scales are defined accordingly to the pressurisation cycles ($\bar{\tau} = \Delta t_{press}$)

and the characteristic length as the vertical tank height H. For both facilities, the ratio of the wall heat transport to storage matches, which is a critical factor considering the initial thermal stratified layer at the liquid surface, discussed in section 2.2. Additionally, for completeness, the Fourier number for the gas phase is rendered for the different working fluids.

Chapter 4

Experimental setup and methods

This chapter overviews the fundamentals of the measurement techniques and main characteristics of the experimental facilities employed throughout this master's thesis to investigate non-isothermal sloshing. The sloshing apparatus (section 4.1), includes an active pressurisation system (section 4.1.1) responsible for pressurising the sloshing cell (section 4.1.2) from an external reservoir (section 4.1.3). The harmonic motion that stimulates sloshing is induced through the VKI SHAKESPEARE sloshing table (section 4.1.4). Likewise, throughout section 4.2, the measurement system implemented to acquire the essential output data, including tank pressure, temperature distributions, table displacement and optical devices that implement the suggested measuring methodologies, are described.

4.1 Experimental apparatus

Under the current research framework, a state-of-the-art small-scale experimental setup was developed. Aware of the initially proposed objectives, a set of high-level requirements to reach the project's overall goal was defined to drive the design. Notwithstanding, these constraints hereafter revealed arise particularly from the final target of employing this experimental apparatus in the 80th ESA parabolic flight test campaign.

1. **Compact setup** due to the size limitation imposed by the transportation box for the parabolic flight test campaign and the SHAKESPEARE sloshing table attaching plate, with dimensions of 1500 mm x 1500 mm (section 4.1.4). Such dimensional constraints lead to using non-cryogenic replacement fluids such as HFE-7200 and HFE-7000, avoiding the burdens and risks of operating cryogenic nature liquids, such as liquid nitrogen (LN_2). Therefore, the maximum allowed length for the overall setup is parametrically evaluated between 500 mm and 1500 mm. Moreover, it must allow for an agile mounting and dismounting process to quickly troubleshoot

and reverse engineer the facility, leading to the added value of resorting to threaded connections.

2. **Rapid initialisation**, since the timescales for each pressurisation cycle should be short enough to allow multiple experiments under distinct initial conditions. Consequently, this constraints the apparatus to an active pressurisation system where gaseous HFE from an external pressurant reservoir is fed under pressure into the sloshing cell, achieving the desired sharp thermal gradient near the interface (section 2.4). Such setup must resort to a connecting pipeline meeting the maximum allowed dimension, where valves are used to control the flow.

3. A **single-species** system must be assured. Such a requirement eases an accurate comparison between experimental and modelled results for non-isothermal sloshing. Therefore, vacuum ports must be added, through which the air is evacuated to a residual absolute pressure.

4. **Non-intrusive measurement techniques** capability, where optical access to the sloshing cell must be provided, allowing optical techniques usage during the experiment's pressurisation, thermal stratification and sloshing phases. This constraint enables the investigation of the non-isothermal sloshing problem through tracer-based laser techniques, such as Particle Image Velocimetry (PIV). Likewise, it allows for characterising sloshing conditions and coupling between the free surface/liquid dynamics to the thermodynamic evolution of the system. Thus, the centreline in the sloshing cell must be cleared of any internal instrumentation such as thermocouples mitigating any scatter of the laser sheet.

5. **Redundant measures** must be employed to meet safety constraints under overpressure operation. Therefore, depressurisation capability must be ensured. Additionally, heating elements must be adequately identified and duly insulated.

Figure 4.1 depicts the final small-scale setup developed and employed in this project.

4.1.1 Active-pressurisation system design and modelling

The experimental apparatus development started from the active-pressurisation system definition, as this is the heart of the setup and constraints the overall project. As such,

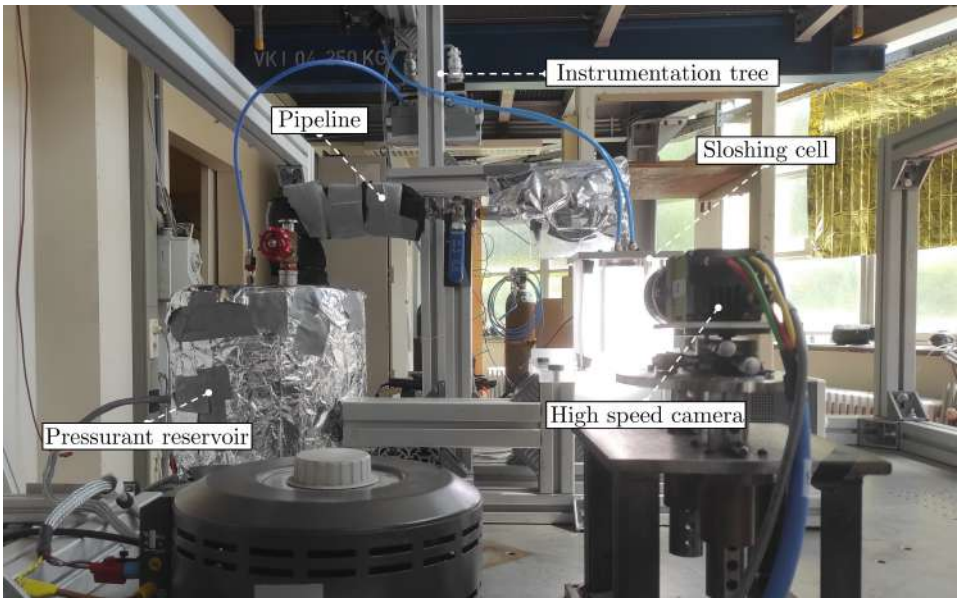

Figure 4.1: Test setup with the insulated pressurant reservoir, insulated pressurisation line with ball and swing-check valve, and backlight illuminated sloshing cell.

a reduced order model (ROM) was developed so that a quick trade-off of the dominant effects can be performed in order to capture the behaviour of its source sub-systems.

A zero-dimensional (0D) thermodynamic model employing a control-volume analysis was chosen, and the Reynolds transport theorem was applied to derive the fundamental laws of mass, momentum and energy conservation [39, 44]. 0D models have no spatial dependency and are only time-dependent, meaning each sub-system may be described with an ordinary differential equation (ODE) that can be integrated in time to calculate the transients, having specified initial conditions.

Hence, the 0D model, defined by the schematic representation in Figure 4.2, is described in this section. Overall, it targets the description of the thermodynamic states in the pressurant reservoir and sloshing cell, as well as the velocity within the connecting pipeline shedding light on possible layouts for the reservoir-line-cell system. Likewise, it answers to the sloshing cell pressurisation timescales, the number of pressurisation cycles for an initial vapour mass, and operating conditions in the external reservoir to achieve a predefined final state in the sloshing cell.

Applying the principle of mass and momentum conservation to a control volume (CV), with a number of one-dimensional inlets and outlets for unsteady flow it yields [44],

$$\frac{d}{dt}\int_{\mathrm{CV}} \rho d\mathrm{V} + \sum_i (\dot{m}_i)_{\mathrm{out}} - \sum_i (\dot{m}_i)_{\mathrm{in}} = 0 \tag{4.1}$$

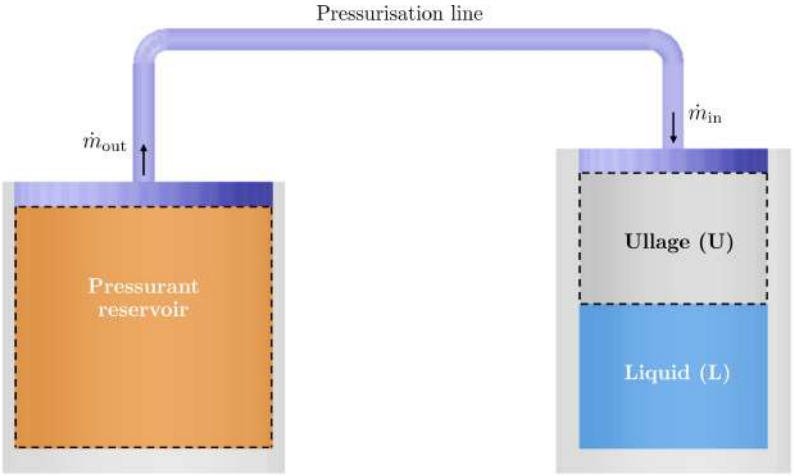

Figure 4.2: Schematic 0D representation of the active pressurisation system with the control volumes defined by dashed contours. The system's thermodynamic properties are represented with index 1 and 2 for the pressurant reservoir and sloshing cell, respectively.

$$\sum \mathbf{F} = \frac{d}{dt}\int_{\text{CV}} \rho U d\text{V} + \sum_i (\dot{m}_i U_i)_{\text{out}} - \sum_i (\dot{m}_i U_i)_{\text{in}} \tag{4.2}$$

where $\dot{m}_i = \rho A U$ stands for the mass flux across the CV boundaries with a transversal area A_i and an average velocity U_i. On the other hand, employing the Reynolds transport theorem to the first law of thermodynamics [39] leads to equation 4.3 for energy conservation.

$$\begin{aligned}\dot{Q}_w - \dot{W}_s - \dot{W}_v = \frac{d}{dt}\int_{\text{CV}} \left(\hat{u} + \frac{1}{2}U^2 + gz\right)\rho d\text{V} + \\ \sum_i \dot{m}_{\text{out}} \left(\hat{h}_i + \frac{1}{2}U_i^2 + gz_i\right)_{\text{out}} - \sum_i \dot{m}_{\text{in}} \left(\hat{h}_i + \frac{1}{2}U_i^2 + gz_i\right)_{\text{in}}\end{aligned} \tag{4.3}$$

The work term $\dot{W}$ consists of three parts. Shaft work ($\dot{W}_s$) deliberately done by external machines, shear work due to viscous stresses ($\dot{W}_v$) and flow or pressure work ($\dot{W}_p$) done at the inlet and outlet which combined with the energy flux is represented by the specific enthalpy $\hat{h}$ term. Moreover, the terms $\frac{\dot{m}U^2}{2}$ and $\dot{m}gz$ describe the changes to the kinetic and potential energy by incoming and exiting flow.

Considering equations 4.1 to 4.3 the following set of simplifying assumptions is introduced to derive the active-pressurisation system model:

- Neglect heat and mass transfer with the liquid phase;

- Fluid properties within the line are constant and equal to those of the pressurant

reservoir;

- Fixed volume system;
- Adiabatic walls across the system ($\dot{Q}_w = 0$);
- Constant local loss factors (ξ);
- Neglect shaft work ($\dot{W}_s = 0$) and viscous stress work ($\dot{W}_v = 0$) ;
- Neglect kinetic energy and potential energy effects;
- Neglect gravity forces across the pressurisation line.

Adopting the above-mentioned assumptions and using the conservation of mass (equation 4.1) and energy (equation 4.3) to represent the pressurant reservoir (index 1), one arrives to the following equations:

$$\frac{d\rho_1}{dt} = -\frac{\rho_1 AU}{V_1} \tag{4.4}$$

$$\frac{d\hat{u_1}}{dt} = \frac{AU}{V_1}\left(-\hat{h}_1 + \hat{u}_1\right). \tag{4.5}$$

Similarly, the same procedure to describe the principles of mass and energy conservation is applied to model the sloshing cell ullage (index 2), leading to equations 4.6 and 4.7:

$$\frac{d\rho_2}{dt} = \frac{\rho_1 AU}{V_2} \tag{4.6}$$

$$\frac{d\hat{u}_2}{dt} = \frac{\rho_1 AU}{\rho_2 V_2}\left(\hat{h}_1 - \hat{u}_2\right). \tag{4.7}$$

Frequently, it is impractical to assess the behaviour of a gaseous system through real gas properties. Hereupon, the ideal gas law simplification is introduced to equations 4.5 and 4.7, where $d\hat{u} \approx c_v dT$ and $\hat{h} = \hat{u} + R_s T$, to model energy conservation, yielding:

$$\frac{dT_1}{dt} = -\frac{AU}{c_v V_1} R_s T_1 \tag{4.8}$$

$$\frac{dT_2}{dt} = \frac{\rho_1 AU}{\rho_2 c_v V_2}\left[c_v(T_1 - T_2) + R_s T_1\right]. \tag{4.9}$$

Lastly, to describe the dynamics within the pressurisation line, the momentum conservation law (equation 4.2) is used accounting for applied forces due to pressure and shear

stress τ_w, per represented by equation 4.10, leading to equation 4.11 which models the velocity U evolution in the pressurisation line.

$$\sum \mathbf{F} = \underbrace{\Delta p \pi \frac{D^2}{4}}_{\text{pressure force}} - \underbrace{\tau_w \pi D L}_{\text{shear stress}} \tag{4.10}$$

$$\rho_1 \frac{dU}{dt} + U \frac{d\rho_1}{dt} + \left(\sum \xi + f \frac{L}{D} \right) \frac{U^2}{2} \frac{\rho_1}{L} + \frac{p_2 - p_1}{L} = 0 \tag{4.11}$$

The friction factor f, commonly quoted as Darcy friction factor, is computed as a function of the Reynolds number, and correlates τ_w with the flow conditions through equation 4.12 where the design value for pipe-flow transition is taken to be $\mathbf{Re}_{\text{crit}} = 2300$ [44]. In addition to the friction loss along the length of the pressurant line, there are local minor losses (ξ) due to inlets and outlets, fittings and valves, hereafter summarised in Table 4.1. A complete collection of local resistance coefficients may be found in Idelchik's *Handbook of Hydraulic Resistance* [57].

$$f = \begin{cases} 64/\text{Re}, & \text{if Re} < 2300 \\ 0.32/\text{Re}^{0.25}, & \text{if Re} \geq 2300 \end{cases} \tag{4.12}$$

Table 4.1: Summary of resistance coefficients for inlets and outlets, elbows and open valves [44, 58].

Component	Inlet	Outlet	90° Elbow	60° Ball valve	Swing-check valve
Local loss (ξ)	0.5	1.0	2.0	3.2	5.1

Therefore, this gives a total of five coupled ODEs to model the system. The numerical model is implemented via a Python script and solved as an initial value problem (IVP) using the Scipy implementation *scipy.integrate.odeint*. All thermodynamic properties are computed using CoolProp [59] which is a Python wrapper for the NIST REFPROP database [60] or resorting to the ideal gas simplification.

System's design

The sloshing cell dimensions are fixed, as the cell to use is a plexiglass rectangular cuboid already employed in previous sloshing experimental campaigns at VKI (section 4.1.2). Ad-

ditionally, the fill level parameter impact on non-isothermal sloshing is not considered under the current research framework. Consequently, it is established at $h/R = 1.44$, ensuring deep-water conditions are met, minimising the tank's bottom geometry impact. Hereupon, the sloshing cell ullage volume is approximately $V_2 = 370 \pm 5$ mL.

The pressurant reservoir (section 4.1.3) consists of a cylindrical brass tank wrapped with a 2700 W heater along the lateral walls, designed to withstanding pressures up to 700 KPa overpressure. Overall, it possesses an approximate internal volume of $V_1 \approx 2400$ mL.

The pressurant line must connect both top-overs and allow enough space to place control valves along the line. As such, it must be U-shaped which introduces two local losses from the $90°$ elbows. Regarding the line length, this parameter is settled by assembling and bolting the pressurant reservoir and sloshing cell into the SHAKESPEARE's upper plate. Here the table's left and central M6 threaded holes assemblies are used, freeing the right assembly to place optical equipment used during PIV testing (section 4.2.4). Hereupon, the total pressurant pipe length is $L = 635$ mm. Regarding the pipe's diameter, a parametric study between $[3 - 6]$ mm is developed. As one might expect, the mass flux increases with the diameter, and thus the pressurisation time decreases. Moreover, even though the model assumes an adiabatic system, such feature is unfeasible to reach in real practical systems. Therefore, in reality, a larger diameter increases the pipe's volume to surface area ratio, minimising heat losses across the pipeline. Thus, the inner diameter is fixed at $D = 6$ mm. Table 4.2 summarises the 0D model geometrical inputs.

Table 4.2: Model geometrical input parameters.

L [mm]	D [mm]	V_1 [mL]	V_2 [mL]
635.0	6.0	2400.0	370.0

Lastly, to fully control the pressurisation procedure, adding valves along the pipe is critical. For the current project, only one controlling valve is added to minimise costs and complexity. Consequently, a ball valve is chosen. Such design allows to fully open the valve via rotating the handle by $45°$, which concedes a quick initialisation with minimal effort, ideal for manual operations. Additionally, the current setup is driven by pressure gradients, meaning backflow could take place, but must be avoided to maintain high safety standards ensuring a properly defined flow direction. Hence, a swing-check valve was added.

System's proof of concept

Plotting the transients of the relevant quantities (Figure 4.3) for HFE-7200 it is possible to assess the system's behaviour for the initial sloshing cell reference state defined in section 4.5. Here the external pressurant saturated vapour is considered to be at $T_{\text{sat}} = 343.15$ K, corresponding to a pressure of 85 kPa.

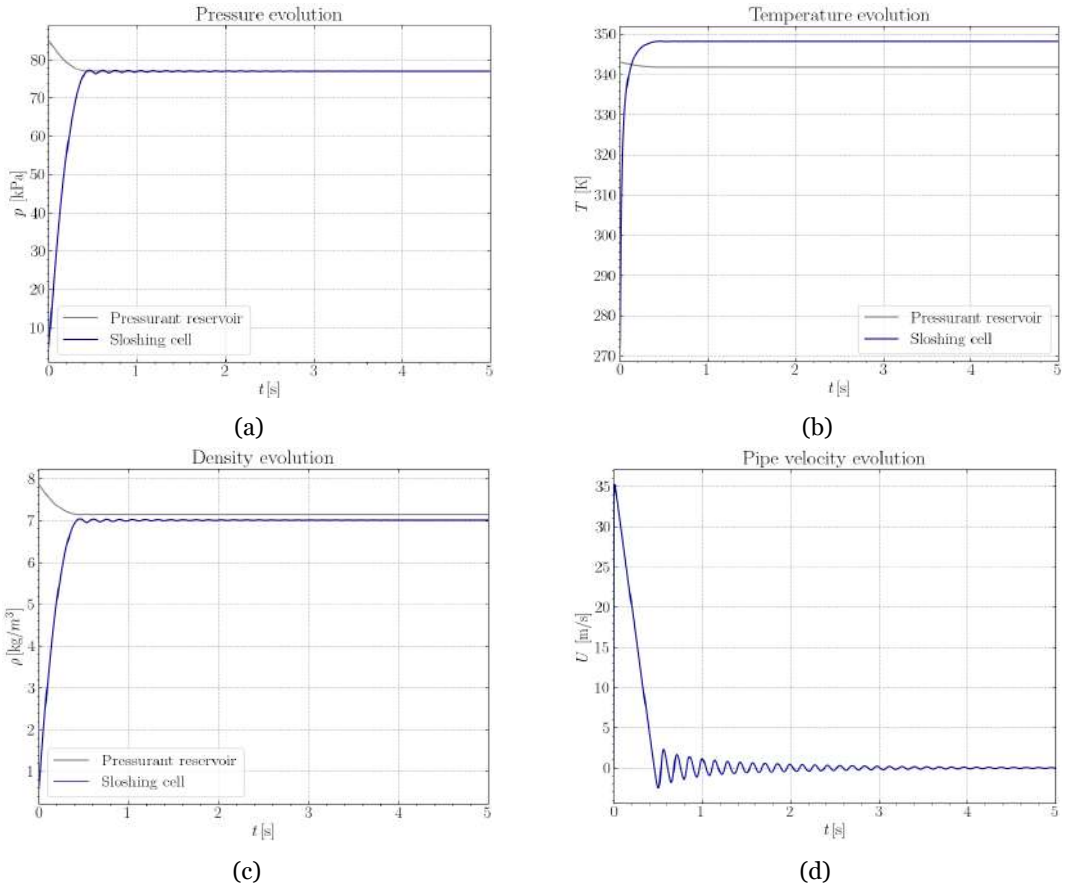

Figure 4.3: Baseline case for HFE-7200 using the ideal gas formulation for the sloshing cell and pressurant reservoir. Pipeline's minor losses (ξ) are retrieved from Table 4.1.

The system's evolution demonstrates its feasibility, fulfilling the rapid initialisation requirement and showcasing its operational patterns. The pressure in both tanks equalises in less than one second, with the external reservoir undergoing a quasi-isothermal decompression. Moreover, the pipe's mean velocity U spikes up to 35 m/s before reaching the final quasi-steady state where pressure oscillations hint the possibility of backflow.

4.1.2 Sloshing cell

The sloshing cell employed in this project is a plexiglass rectangular cuboid with dimen-

sions 120 mm × 120 mm × 151 mm in which a cylindrical hole with diameter $D = 81$ mm was drilled down to a depth of 130 mm, as showcased in Figure 4.4. However, the top cover employed reduces the tank inner height to $H = 120$ mm. Amid use, care must be taken to ensure the cell maintains the highest quality standard regarding optical access for image capturing, as plexiglass material is easily scratched, leading to lasting marks that could distort the captured images across the walls and bottom. Table 4.3 summarises the cell's dimensions and operating fill height.

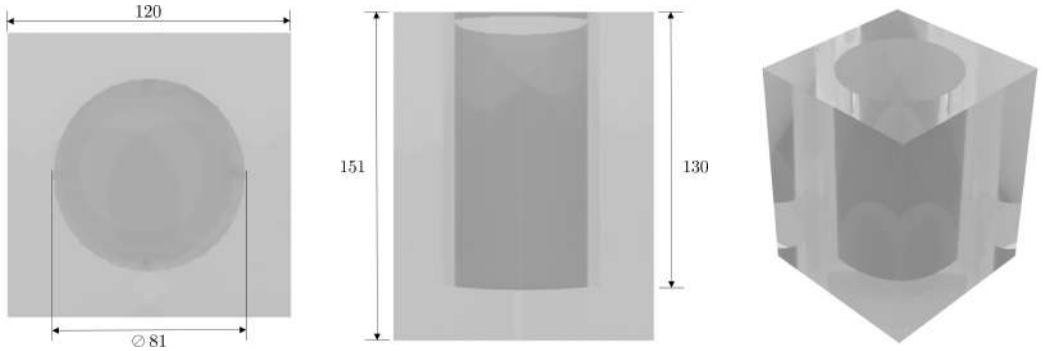

(a) Top-view. (b) Lateral view. (c) Isometric view.

Figure 4.4: Plexiglass sloshing cell renderings with all dimensions in mm.

Table 4.3: Sloshing cell inner dimensions and fill height for the initial liquid volume of 300 mL.

	Radius R (mm)	Height H (mm)	Fill height h (mm)
Plexiglass sloshing cell	40.5	120	58.2

A new top cover was manufactured for the sloshing cell to perform the non-isothermal sloshing experiments. This is a vital part of the current small-scale setup since it must withstand pressure cycles ranging from under-pressure to overpressure. Consequently, the whole assembly linking the cell-cover must ensure high levels of pressure tightness. In other words, no pressure leaks can occur along the facility, otherwise, the experiment's feasibility is at risk.

Such strict requirements drove the top-cover design, and the decision not to use thermocouples was made due to the fact that no threaded connection, which should ensure sealing tightness, was available. Consequently, the thermocouple's placement across the cover would have to resort to high-temperature sealing glue, which does not guarantee leak tightness. Hereupon, the characterisation of the thermodynamic system was made possible by placing a pressure tap in the upper part of the cell. Understandably, since no thermal information inside the cell is retrieved during the stratification and destratification stages, it is beyond this project's scope to fully characterise the thermodynamic evolution of the system. However, this offers an advantage. Since no instrumentation is

placed in the cell's interior, the intrusiveness level is minimised, increasing the accuracy and veracity of up-scaling the pressure drop data and correlating the sloshing dynamics against literature results.

The top cover (Figure 4.5), which was manufactured for this project, consists of a 10 mm aluminium plate with a cylindrical extrusion in the centre with a thickness of 10 mm and a diameter of 79.9 mm. In the extruded section, one milled groove was added to place an O-ring in contact with the sloshing cell inner walls. Additionally, a second groove was performed to add an O-ring in touch with the cell's upper face. Both combined allowed for a leak-tight system used throughout the test campaign. Furthermore, the cover is fastened to the upper sloshing cell face using six M4 holes, which bolt into the added inserts. Lastly, the pressurisation line and filling/vacuum port are screwed into the aluminium cover through two G 1/8" threaded holes, while the pressure tap is screwed utilising an M5 threaded hole.

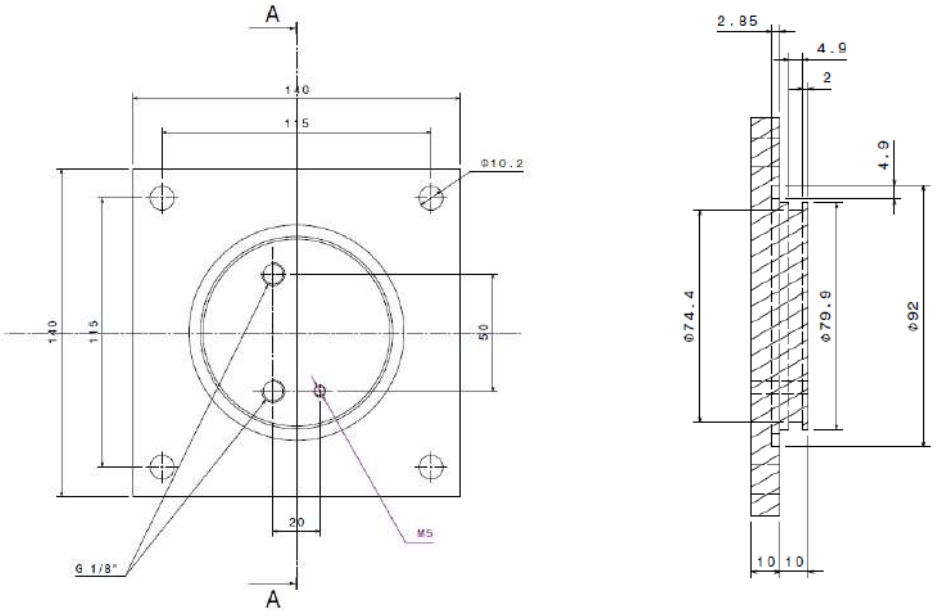

(a) Bottom-view. (b) Lateral view.

Figure 4.5: Technical drawing of the sloshing cell top cover made in aluminium with all dimensions in mm.

4.1.3 External pressurant reservoir

The external pressurant reservoir, represented in Figure 4.6a with an inner height of 230 mm and a radius of 61 mm, is a brass cylinder with a conical extrusion at the top for the cover M6 threaded connections. The aluminium top cover with 20 mm thickness has three 4.30 mm radius holes that connect the pressurisation line, a pressure tap and the

filling/vacuum port. A heater was mounted in the outer surface of the side-walls with a maximum admissible power of 2700 W granting the required heating capability to vaporise the operating liquid before pressuring the sloshing cell.

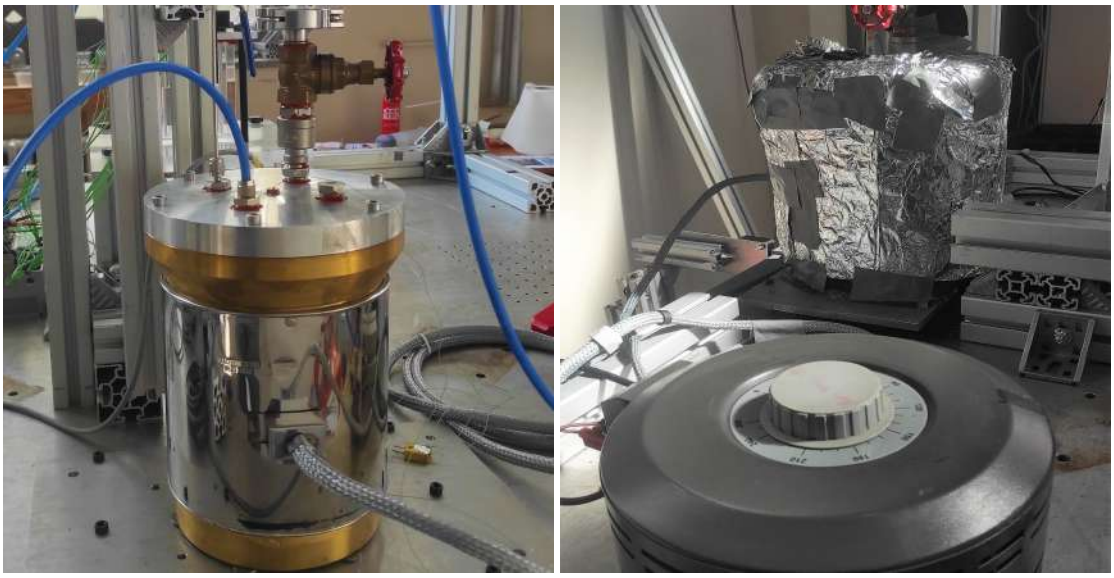

(a) Non-insulated reservoir and cover connections. (b) Insulated reservoir and power supply.

Figure 4.6: External pressurant reservoir where the blue pipe connects to the Validyne pressure transducer and the red gate valve controls the filling and vacuum port.

The primary concern of operating this sub-system lies in the fact that to achieve the desired stratification at the cell, the vapour and, inherently, the reservoir's wall temperature will be well above safe operational conditions. Hence, it must be properly insulated. Therefore, as represented per Figure 4.6b, rock wool protected by reflective foil was added along the walls to avoid any incident during its operation. Moreover, the tank's large thermal inertia does not allow to dissipate the heat quickly, meaning care must be taken to avoid overshooting the desired vapour condition, which could lead to gaskets and blue pipes melting.

Regarding the heater, it is connected to an external power supply (Figure 4.6b), which operates at a steady 13 A and has a top knob to control the voltage input up to 230 V. It is operated below the maximum heater permissible power of 2700 W and duly grounded via the sloshing table.

4.1.4 SHAKESPEARE sloshing table

SHAKESPEARE stands for SHaking Apparatus for Kinetic Experiments of Sloshing Projects with EArthquake REproduction. The table is moved by a hydraulic cylinder system, which

is the most capable in terms of excitation frequency and amplitude. It can simulate realistic seismic waves with amplitudes ranging from $[1 - 30]$ mm and frequencies ranging from $[1 - 10]$ Hz. The main table surface, on which the small-scale experimental setup is placed, has a square shape with 1.5 m length and is perforated with five M6 threaded holes assemblies to provide for customisation in the attachment of various experimental facilities. This sloshing table has three sliding modules, one for each axis, that allow for the replication of sloshing excitations with controllable amplitudes and frequencies in all three directions.

Figure 4.7: SHAKESPEARE sloshing table of the von Karman Institute with the experimental setup assembled.

Here the motion described by a sinusoid excitation in the x direction, given by equation 3.12, is introduced via a control panel to study lateral sloshing. To do so, a .csv file is imported where for each time-step the respective x position is followed by the table's sliding upper module.

4.2 Instrumentation

The pressure measurements at the sloshing cell and pressurant reservoir are performed through a top-cover pressure tap connected to Valydine transducer, and the setup de-

scribed in section 4.2.1. Thermocouples along the cell's external walls were placed to capture residual changes within the ullage and liquid without compromising the overall system leak tightness, as detailed in section 4.2.2. An optical displacement sensor (section 4.2.3) was added to connect the retrieved free surface displacement through the optical measurement setup (4.2.4), under sloshing, with the imposed excitation. Lastly, to minimise heat losses along the pressurant line, a heating element was combined (section 4.2.5).

The instrumentation is connected to a NI cDAQ-9174 [61], which supplies the retrieved measurements to the LabVIEW script from six thermocouples, two pressure transducers, the optical displacement sensor (ODS) and the camera trigger signal.

4.2.1 Pressure measurement

The pressure within the sloshing cell was monitored using a top-mounted pressure tap linked to a Validyne with an M44 diaphragm diameter and a maximum permissible pressure of 220 KPa. On the other hand, the pressure inside the pressurant reservoir was extracted using a top-mounted pressure tap linked to a Validyne with an M46 diaphragm diameter and a maximum permissible pressure of 350 KPa [62]. Both Validynes are placed high in the instrumentation tree (Figure 4.8b) ensuring that no condensed liquid gets trapped within the blue pipes.

A Validyne CD15 carrier demodulator [63] was used to convert the analogue pressure measurements into output voltages between ± 10 V. This transducer reads the differential pressure between its positive and negative terminals. The positive terminal was connected to the pressure tap within the sloshing cell or pressurant reservoir, and the negative one was left open to ambient conditions. The open terminal was connected to a tube placed inside the assembly bosh profiles (Figure 4.8b). This was done to minimise the effect of the surroundings on the ambient pressure measurements and to get more stable readings.

A DPI 610 Druck pressure calibrator was used to calibrate the Validynes. The calibration procedure involved pumping pressure from the calibrator device while leaving the negative side of the Validyne exposed to the atmosphere (Figure 4.8a). The signal demodulator voltage span was adjusted for the diaphragm permissible limits, and the pressure-voltage relation was retrieved via the LabVIEW readings.

The calibration laws for the sloshing cell and pressurant reservoir transducers were deter-

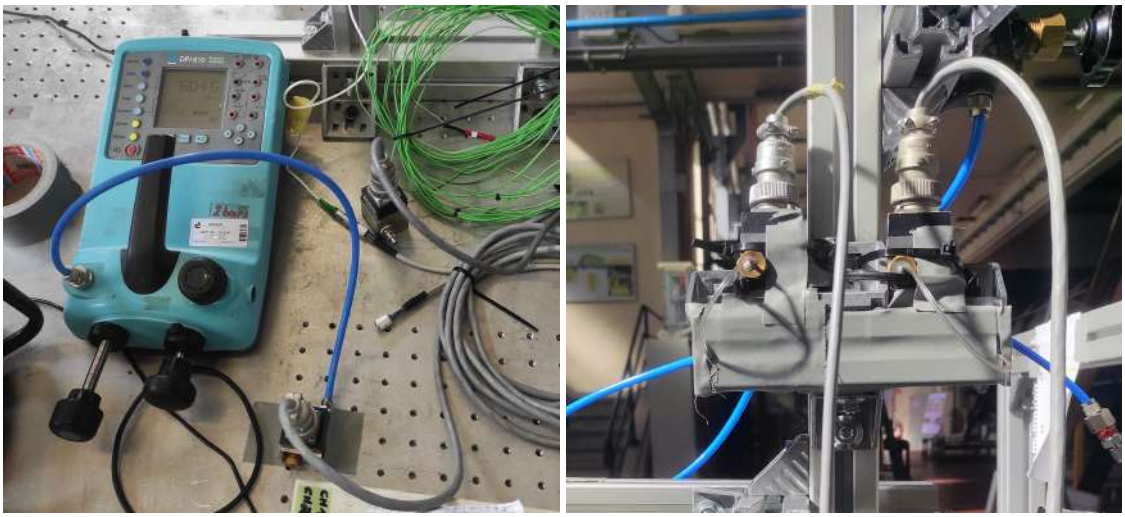

(a) Pressure calibration setup. (b) Instrumentation tree.

Figure 4.8: Pressure measurements calibration setup and Validynes pressure transducers in the instrumentation tree.

mined to be linear, and from the collected points were defined by the following relations:

$$\Delta p_{\text{cell}}\,[\text{Pa}] = 22050.69\mathcal{V}\,[\text{Volts}] + 1791.46 \tag{4.13}$$

$$\Delta p_{\text{reservoir}}\,[\text{Pa}] = 35390.39\mathcal{V}\,[\text{Volts}] - 465.18. \tag{4.14}$$

The sloshing cell calibration law standard error (equation 4.13) is $S_{\text{cell}} = 286.39$ Pa, while the pressurant reservoir's standard error from equation 4.14 is $S_{\text{reservoir}} = 496.59$ Pa. Lastly, the differential pressures are converted to absolute values by summing the ambient pressure reading retrieved from a fixed sensor at VKI.

4.2.2 Temperature measurement

The temperature measurements were performed using 0.25 mm grounded mineral insulated type K thermocouples from TC Direct [64]. Uncertainty from the calibration is considered to be ± 0.5 K. The thermocouples were connected to the data acquisition system (DAQ) via a NI-9211 card [65] with four channels and a NI-9213 card [66] with sixteen channels.

A thermocouple was added upstream of the pressurant line ball valve to control the pressurant vapour temperature during the pressurisation stage. Thus, allowing to appraise

the energy losses along the pipeline by coupling the measurements with the reservoir saturation pressure. Its placement was performed by drilling a threaded hole into the line, where a small pipe insert was added with the high-temperature sealing glue to prevent any leakage.

Regarding the cell thermocouples, as substantiated in section 4.1.2, only external temperature was retrieved. Two thermocouples were placed at $z = 30$ mm and $z = 90$ mm, to capture any thermal wall change in the liquid and ullage region, respectively. On the other hand, a thermocouple was fixed to the top cover ($z = 140$ mm) to complete the vertical thermal profile, as well as to evaluate if the pipeline heating element and superheated injected vapour impact the system. The origin is at the cell's bottom ($z = 0$ mm). Lastly, one more external thermocouple was utilised to measure the liquid's temperature before filling the cell.

4.2.3 Table displacement measurement

The sloshing table's displacement was determined using an optical displacement sensor (ODS30) as represented in Figure 4.9. This sensor generates voltages ranging from $[1 - 9]$ V, which correspond to the lowest and largest distances that may be recorded, while monitoring displacements across $[28 - 32]$ mm range. To precisely define the start and stop positions for the shaking excitation, the table displacement was combined with the outputs from the thermocouple and pressure transducer. The ODS was positioned on a platform made of bosch profiles, such that it faced the sloshing table's x-axis.

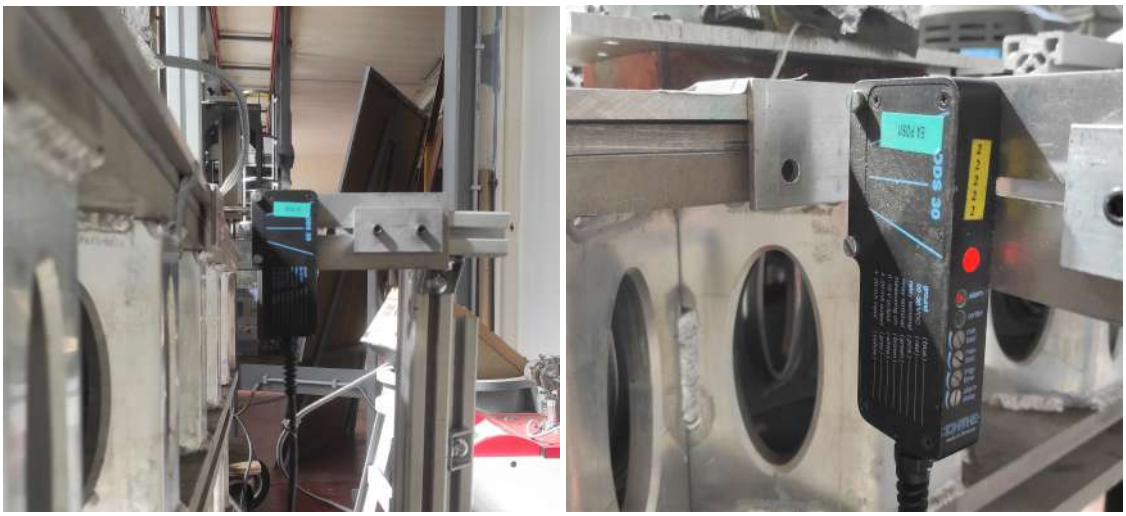

Figure 4.9: Optical displacement sensor to measure the sloshing table's motion along the x direction.

4.2.4 Optical measurement setup

The optical measurements were performed using the high-speed camera JAI SP-12000M-CXP4 with a 60 mm objective [67]. The camera was mounted on the sloshing table at the central threaded assembly through two fixing supports. A stiff support allowed for fine-tuning its height and a 3-axis support where yaw, pitch and roll were adjusted to level the image. The recording software used was the Norpix Streampix [68], where the frame rate, exposure, and region of interest (ROI) were adequately adjusted. Moreover, the external module FG pulse generator was enabled and the pulse frequency locked at the recording rate to synchronise the acquired images with the thermocouple and pressure data (Figure 4.10a).

Throughout the experimental campaign, backlighting was performed to retrieve the free surface displacement. Engineering paper was glued to the cell's lateral as well as back faces and around the bosh profiles supporting the cell on the shaking table. The lighting was achieved through two LED lights behind the sloshing cell, as represented in Figure 4.10b.

(a) Camera setup. (b) Backlight technique setup.

Figure 4.10: Optical measurement setup to retrieve the free surface displacement with backlighting.

PIV experimental setup

Particle Image Velocimetry (PIV) is a non-intrusive measurement technique used to determine the instantaneous and mean velocity field of particles dispersed in a liquid flow.

Here the particles used are fluorescent polymer microspheres with $\rho = 1.3\,\mathrm{g/cm^3}$ and a diameter ranging from $[1-5]$ μm. These particles are chosen to behave like tracers, so their velocity will correspond to the fluid's velocity [69]. The acquisition system takes images of the particle flow, illuminated by a laser sheet at two consecutive time steps. The velocity field is then calculated by analysing particle motion caused by flow and relating pixel displacements to the physical dimensions of the region of interest (ROI). The images are decomposed into interrogation windows during the processing algorithm. These windows are cross-correlated for each pair of images to determine the most likely displacement of the seeding particles.

Over the course of the test campaign, only one PIV measurement was performed (section 4.4) with the sole purpose of evaluating the velocity fields in the liquid HFE-7200 prior to sloshing. Moreover, the planar dynamics were briefly captured to appraise the sloshing-induced mixing capability under such a stable mode (section 2.1.2).

Figure 4.11a introduces the employed PIV experimental setup. Here the continuous laser beam was focused through the spherical lens (SL) and turned into a sheet with a cylindrical lens (CL). This sheet was deflected through the prism underneath the sloshing cell, thus illuminating its mid-plane. Such assembly minimises the interface/light interaction creating the liquid central plane represented in Figure 4.11b. The camera frame rate was fixed at 30 fps, the focal length at $f/2.8$, minimising the laser sheet thickness, while the exposure time was settled in the StreamPix recording software at 1500 μs.

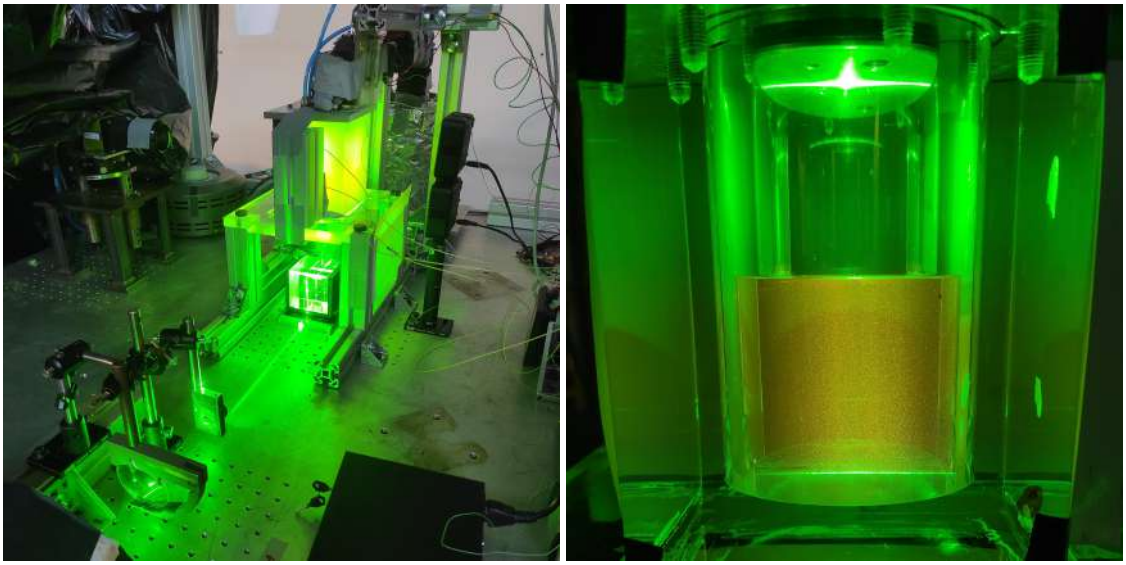

(a) PIV setup. (b) Laser illuminated liquid central plane.

Figure 4.11: Particle image velocimetry experimental setup using fluorescent polymer microspheres.

The PIV analysis, divided in three processing steps, has been conducted through the PIVlab tool [70] in a time-resolved mode, following the sequencing style "[A+B], [B+C]".

The image pre-processing starts by isolating the region of interest (ROI). Since the objective under sloshing is to retrieve the liquid bulk motion responsible for the destratification and no enhancement processing algorithms to capture the moving interface are applied [69], the ROI is defined sufficiently away from the interface. However, such a region is expanded without losing accuracy for the stationary phases. Afterwards, a high pass filter is enabled with a kernel size of 32 px, as well as the auto contrast stretch function, enhancing the image quality. Figure 4.12 shows an example of PIV pre-processing.

The PIV processing has been done using the parameters listed in Table 4.4.

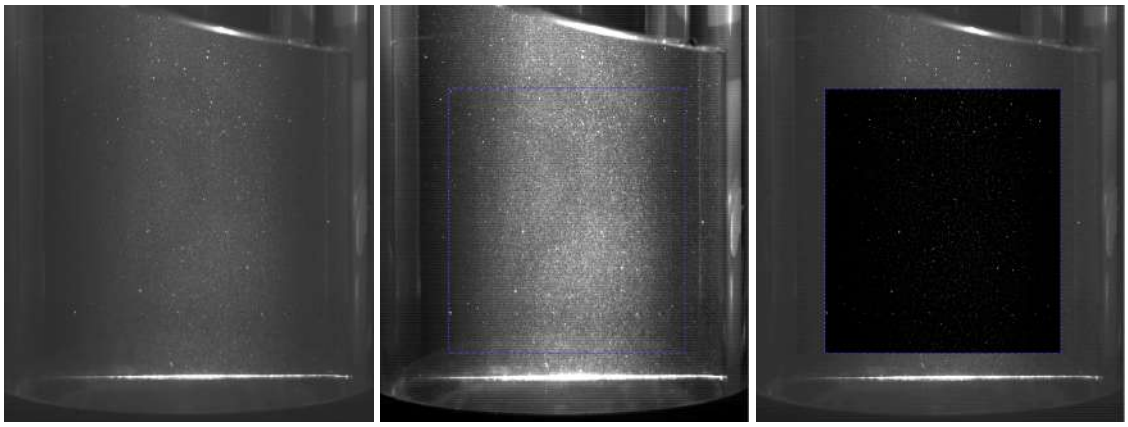

(a) Raw image. (b) Region of interest. (c) Filtered region of interest.

Figure 4.12: Example of PIV pre-processing under planar sloshing.

Table 4.4: Vector calculation parameters.

Parameter	Value/Option
PIV algorithm	FFT window deformation
Scaling factor	0.0561 mm/pixel
Initial window size	128 pixels
Final window size	32 pixels
Initial overlap	50%
Final overlap	50%
Number of passes	3
Sub-pixel estimator	2D Gauss

Lastly, PIV post-processing aims to eliminate nonphysical values of the velocities. Thus, two filtering techniques were employed: (a) velocity vector range filtering, restricting the vectors to a user-specified range in the x and z directions, and (b) a standard deviation

and local median filter where the median velocity vector is computed and compared to the velocity fields.

4.2.5 Heating elements

Two Minco Polyimide Thermofoil HK6907 Heaters [71] were added downstream of the valves in contact with the pressurant line. These heaters serve the purpose of minimising the vapour's energy losses along the pipeline by imposing a fixed temperature condition at the heater surface. The heaters have dimensions of $25.4\,\mathrm{mm} \times 50.8\,\mathrm{mm} \times 1.14\,\mathrm{mm}$, maximum working temperatures of $100°\mathrm{C}$, and maximum power output of $16.4\,\mathrm{W}$. Using thermal paste, a thermocouple was attached to these components to measure their temperature as the experiment's heating process progressed. This thermocouple was then coupled to a Tempatron PID330 controller [72], which controlled the TENMA $72-8700$'s power supply [73] ensuring the temperature limit was never crossed. Figures 4.13a and 4.13b, show the non-insulated heater in contact with the pipeline and the power supply connected to the PID controller, respectively.

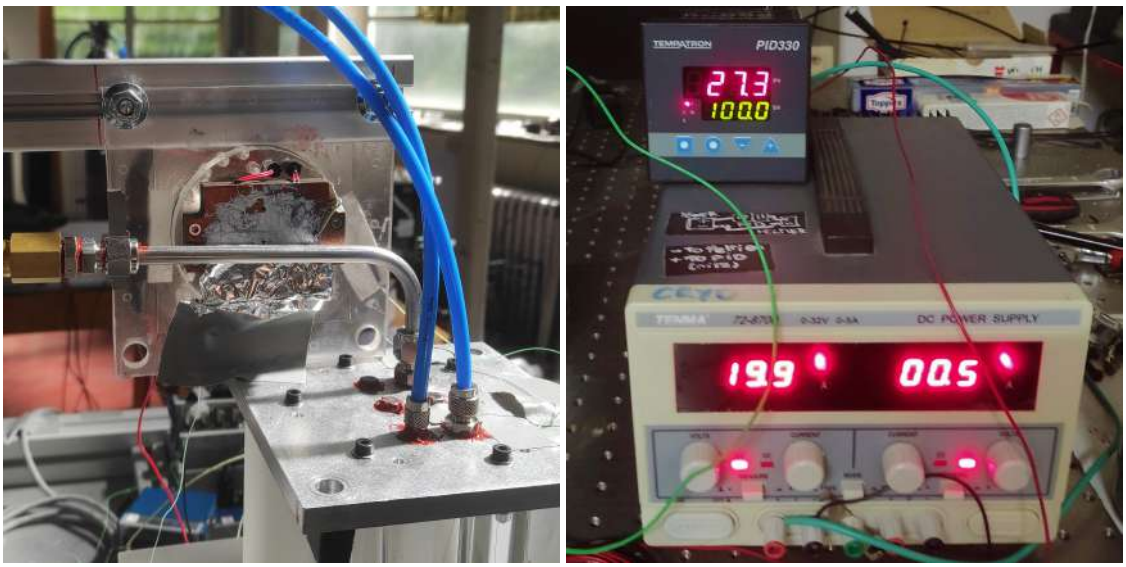

(a) Foil heaters in contact with the pipeline. (b) Power supply and PID controller.

Figure 4.13: Heating elements setup to minimise the vapour's heat losses along the pressurant line.

4.3 Experimental procedure

For this master's thesis project, only experimental tests with HFE-7200 were performed. The general experimental procedure employed across the campaign may be divided into

two phases. The first phase, the most time-consuming and only repeated at the start of a test day, consists of preparing the pressurant reservoir for the pressurisation cycles. At the same time, the pipeline is heated, and the working liquid is cooled. Following is a description of the first phase's overall process:

1. Prepare a set of plastic bottles filled with HFE-7200 at ambient conditions, and place them in the freezer. This freezer, located on VKI's main building's upper floor, is defined to hold a steady condition of approximately $-40°$C, which should ensure the liquid is in a subcooled state by the time it is used to fill up the cell. Here the bottles are left for at least one hour prior to starting the experiment itself ($\Delta t_{\text{freezer}} \gg 1$ h);

2. Fill the pressurant reservoir with HFE-7200 at ambient conditions through the filling/vacuum port. This was accomplished by carefully extracting 300 mL of the solution from its original container with a 500 ± 5 mL syringe, to which a transparent rubber pipe with a KF fitting is attached, allowing to perform the filling procedure;

3. Clean the filling/vacuum port and connect the vacuum pump. Plug the pump to the 16 A grid connection and enable the safety switch. Then open the pump's ceiling valve and rotate the power switch to enable vacuuming. Simultaneously start the LabVIEW acquisition and control the pressurant reservoir's pressure evolution until a steady state is reached. Once such condition is attained, close the port gate valve, disconnect the pump and fit a blockage KF connection. This step is crucial, and if not done correctly, it can result in significant pressure leaks. Lastly, monitor the pressure evolution and verify if the saturation data corresponds to the recorded pressure assuring the fraction of air in the tank is residual. Otherwise, the procedure must be re-done;

4. Connect the reservoir's heater power supply to the grid and turn it on. Start by setting the voltage knob to 90 ± 5 V for a quick initialisation. Once the threshold of 0.70 bar is within range, reduce the input voltage to 30 ± 5 V until a steady state is reached. Permanently control the pressure evolution from the LabVIEW acquisition and adjust the power supply voltage. This is a highly delicate step, where one should continuously monitor the reservoir's state to avoid overshooting the desired condition leading to an over-heated reservoir;

5. Turn on the pipeline power supply with a constant voltage supply of 20 ± 0.1 V. First, the heater supplies a continuous heat flux as it warms up until the maximum

operating temperature of $100°$C. Then, the PID controller is activated, enforcing that the temperature at the surface of the heater remains constant. Thus, after this point, the system is gradually warmed with a steady temperature boundary condition in the pipeline between the ball valve and cell inlet.

Once the pressure threshold in the pressurant reservoir is reached, and the liquid has spent enough time in the freezer to attain a considerable subcooled state, the second phase may commence. This phase is extremely intensive and contemplates the experiment itself. Therefore, time periods and thresholds are defined to maximise repeatability. Following is a description of the second phase's process:

1. Prepare the StreamPix high-speed digital video recording software by guaranteeing that the trigger function is activated and the signal is synchronised with the LabVIEW system. Likewise, ensure the image sequence is acquired at 100 fps and the trigger signal at a sampling rate of 100 Hz. Here, turn on the two LED lights and verify the captured image's quality and region of interest;

2. Enable the sloshing table hydraulic pump and logics in the control panel. Besides that, certify the correct file with the desired test point is uploaded and correctly loaded;

3. Vacuum the sloshing cell previous to the filling procedure. Such is possible by connecting the pump pipe to the cell filling/vacuum port KF connector. The overall goal rests upon allowing a quick filling as no backflow air will come through the filling line as a trade with the filled liquid. This minimises the subcooled liquid exposure time to ambient conditions, maximising the thermal stratification degree;

4. Take an HFE-7200 bottle from the freezer and transport it to the SHAKESPEARE within a freezer bag to minimise heat losses. Open the bottle and measure the temperature with a thermocouple, followed by filling the syringe with 300 ± 5 mL. Plug it into the filling port and fill the cell for a given loading time interval ($\Delta t_{\text{filling}}$) by controlling the needle valve in the port;

5. After the filling procedure is finished, the vacuum process is re-done. This step ensures no air is left trapped within the liquid and eradicates any air that seeped in once the line valve was re-opened to fill the cell. The pump is kept vacuuming until a steady state is reached, which takes approximately 45 seconds ($\Delta t_{\text{vacuum}} \approx 45$ s);

6. Once the vacuum line is duly disconnected from the cell and closed with a blockage KF, any loose items in the SHAKESPEARE must be removed, and the recording and trigger function on StreamPix software started. This allows acquiring image footage from the initial thermal stratification, pressurisation, relaxation and sloshing phases;

7. The pressurisation is started by manually opening the ball valve, which transports the superheated vapour from the pressurant reservoir to the sloshing cell. To ensure repeatability the target is to achieve 0.30 bar in approximately 60 seconds ($\Delta t_{\text{press}} \approx 60$ s). Here, the valve is slowly opened to minimise impinging the liquid's free surface, maximising the stratification intensity;

8. With the cell pressurised, a relaxation phase follows for a given allowed time interval (Δt_{relax}) before starting sloshing;

9. Lastly, the sloshing table home function is enabled, and the sloshing motion is initialised for a period of 120 seconds ($\Delta t_{\text{slosh}} \approx 120$ s);

10. Once the sloshing excitation finishes, turn off the LabVIEW acquisition, turn off the hydraulic system of the shaking table, turn on the vacuum pump to bleed the system and prepare everything for the next experiment.

The steps outlined above are the general procedure which was carried in all of the experiments performed during this project. However, some slight modifications were employed for particular experimental conditions where distinct time intervals were tested to evaluate the thermodynamic evolution under sloshing. All in all, the performed experiments may be divided into four distinct procedures, with their respective time intervals showcased in Table 4.5.

Table 4.5: Procedure definition accordingly to the specified time intervals.

Procedure	$\Delta t_{\text{filling}}$ [s]	Δt_{vacuum} [s]	Δt_{relax} [s]	Δt_{slosh} [s]
I	≈ 180	≈ 45	≈ 30	≈ 120
II	≈ 30	≈ 45	-	≈ 120
Baseline I	≈ 30	≈ 45	≈ 480	≈ 120
Baseline II	≈ 30	≈ 45	≈ 300	≈ 120

Procedure I was defined with a filling period of approximately 180 seconds ($\Delta t_{\text{filling}} \approx 180$ s). For such, the needle valve is operated in a nearly closed state. Such slow filling in-

creases the subcooled liquid's exposure time to ambient conditions leading to a considerable temperature rise. Therefore, once the cell reaches the desired fill level and a thermal stratification settles in, the difference in temperature between the bulk and the liquid's free surface will be lower than for a quicker filling procedure. This is expected to translate into a less pronounced pressure drop once sloshing is initiated.

Procedure II was set to evaluate the system's evolution once no relaxation phase was allowed. Consequently, the two pressure drops visualised in the acquired data would collapse into one. Under this procedure, the most violent pressure drops are expected, especially after minimising the filling time that maximises the liquid's subcooled condition once settled in the cell.

Lastly, baseline procedures I and II arise from evaluating the system's behaviour without sloshing, so a baseline case would counteract procedures I and II. However, once the system settled for long enough, sloshing was imposed to establish a comparison between both baseline procedures and extend the pressure drop retrieved database.

4.4 Experimental matrix

It is critical to define the excitation parameters to perform the experimental characterisation of the tank's thermodynamic behaviour under sloshing conditions. For the large liquid depth to radius ratio, appearing in the presented experiments, the natural frequency ω_{11} of the first asymmetric mode was $\omega_{11} = \sqrt{\xi_{11} g/R} = \sqrt{1.841 g/R} = 21.117$ rad/s (with $\xi_{11} = 1.841$ as the eigenvalue of the first asymmetric mode). Therefore, resorting to Miles' weakly nonlinear theory (section 2.1.2), three sloshing points were settled, as represented in Figure 4.14. Experimental point P_1 chosen with a forcing amplitude $A_f = 1.0$ mm and frequency $f_e = 3.00$ Hz belongs to the stable planar waves regimes defined by the linear theory. Experimental point P_2 with $A_f = 1.0$ mm and frequency $f_e = 3.10$ Hz belongs to the unstable chaotic regime. Point P_3 with a chosen frequency above the first mode ($\omega/\omega_{11} = 1.041$), located near the boundary β_4 where the motion bifurcates, is outlined by a rotational non-planar free surface displacement. Table 4.6 summarises the sloshing points excitation characteristics.

Table 4.7 showcases the experimental matrix for the tests reported in Chapter 5. Cases ID $1 - 8$, except ID 3, were performed using the testing procedure I characterised by a long

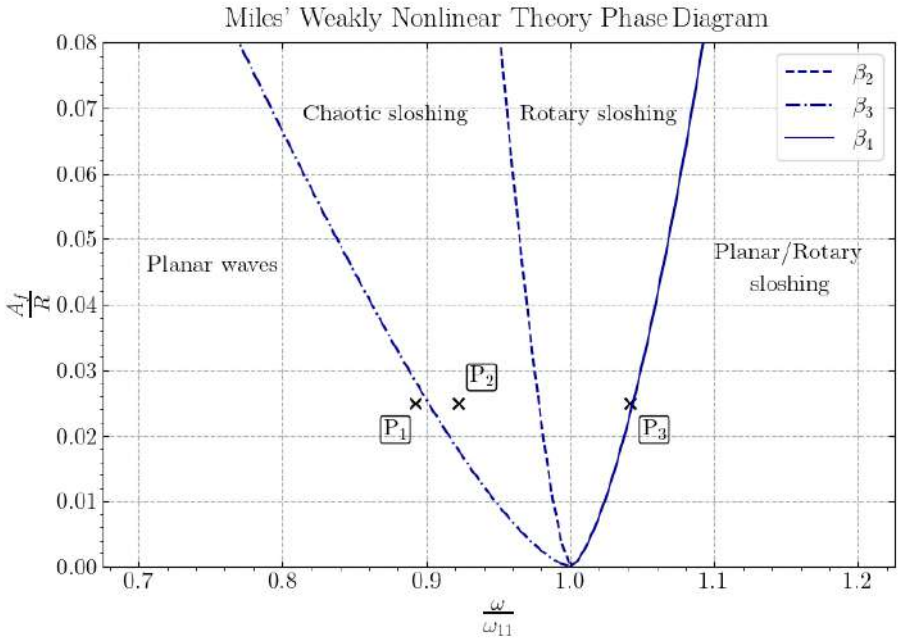

Figure 4.14: Dimensionless forcing amplitude-phase diagram as a function of frequency ratio with tested sloshing points.

Table 4.6: Investigated excitation cases.

Sloshing point	Regime	A_f/R	ω/ω_{11}	A_f [mm]	f_e [Hz]
1	Planar	0.025	0.893	1.0	3.00
2	Chaotic	0.025	0.922	1.0	3.10
3	Swirl	0.025	1.041	1.0	3.50

filling period and an allowed interval of relaxation after the pressurisation in the order of 30 seconds. With this methodology, three tests were performed under the planar regime, two swirl and two chaotic. Cases ID 9–11 were performed through procedure II, where sloshing is initiated once the pressurisation phase ends. Lastly, Cases ID 12–15 employ the baseline procedures, and ID 15 is characterised through the application of the PIV technique. Throughout the experiments, the initial temperatures T_0 were retrieved before the filling procedure, and once the experiment was finished, the final liquid's volume V_f was extracted and measured.

4.5 Fluid properties

The non-cryogenic sloshing tests for this master's thesis are performed with liquid HFE-7200. This serves as a reasonable substitute for liquid hydrogen [34] and is often used in

Table 4.7: Experimental matrix for the tested measurement conditions.

Test ID	Slosh point	Regime	PIV	T_0 [°C]	Procedure	V_f [mL]
1	P_1	Planar	-	-	I	-
2	P_1	Planar	-	-	I	310
3	P_1	Planar	-	-	-	-
4	P_3	Swirl	-	-	I	350
5	P_2	Chaotic	-	-	I	330
6	P_1	Planar	-	-	I	350
7	P_3	Swirl	-	-31.15	I	340
8	P_2	Chaotic	-	-32.55	I	350
9	P_1	Planar	-	-38.15	II	315
10	P_3	Swirl	-	-38.05	II	325
11	P_2	Chaotic	-	-30.15	II	360
12	P_3	Swirl	-	-34.15	Baseline I	350
13	P_3	Swirl	-	-34.65	Baseline II	350
14	P_3	Swirl	-	-	-	-
15	P_1	Planar	Yes	-36.65	Baseline I	350

terms of dynamics, especially in compensated gravity conditions [74]. Table 4.8 represents the 4th order polynomial fits for HFE-7200 properties extracted from experimental data [75, 76]. Lastly, Table 4.9 provides information on the reference properties of hydrogen, nitrogen, HFE-7000, and HFE-7200 used for the similarity analysis.

Table 4.8: Coefficients for the 4th order polynomial fits for temperature-dependent HFE-7200 properties [75, 76].

$f(T) = a + b_1T + b_2T^2 + b_3T^3 + b_4T^4$					
Fluid property	b_4	b_3	b_2	b_1	a
ρ_L [kg/m^3]	-1.17E-9	-1.24E-5	9.64E-3	-4.58	2.27E3
ρ_U [kg/m^3]	7.46E-8	-7.95E-5	3.25E-2	-6.01	4.23E2
μ_L [Pa s]	1.04E-11	-1.41E-8	7.18E-6	-1.63E-3	1.41E-1
μ_U [Pa s]	-2.04E-15	2.30E-12	-9.34E-10	1.95E-7	-9.85E-6
σ [N/m]	6.06E-11	-7.91E-8	3.86E-5	-8.44E-3	7.16E-1
k_L [W/m K]	4.79E-10	-6.27E-7	3.08E-4	-6.76E-2	5.65

Table 4.9: Fluid properties corresponding to the reference temperature and pressure given by the saturation condition for hydrogen, nitrogen, HFE-7000 and HFE-7200 [59, 75, 76].

	T_{ref} [K]	p_{ref} [kPa]	ρ [kg/m^3]	ν [m^2/s]	c_p [J/kg K]	c_v [J/kg K]	k [W/m K]	Δh_v [J/kg]	β [1/K]	σ [N/m]	**Pr**
LH_2	30.37	101.32	70.85	1.90E-7	9772.46	5660.94	0.10	4.49E5	1.67E-2	1.91E-3	1.27
LN_2	77.36	101.32	806.08	1.99E-7	2041.49	1084.07	0.14	1.99E5	5.67E-3	8.88E-3	2.27
HFE-7000	293.15	58.62	1418.30	3.61E-7	1218.70	929.97	0.08	1.40E5	1.94E-3	1.23E-2	8.24
HFE-7200	273.15	5.18	1478.07	6.62E-7	1214.17	-	0.07	1.26E5	1.47E-3	1.60E-2	16.08
GH_2	24.68	300	3.64	3.44E-7	1.49E4	6727.98	0.02	-	0.07	-	0.79
GN_2	83.63	200	8.66	6.86E-7	1180.12	786.89	7.96E-3	-	0.01	-	0.88
GHFE-7000	327.53	200	16.17	7.46E-7	988.25	918.34	0.01	-	4.38E-3	-	0.91
GHFE-7200	313.20	30	3.16	1.08E-5	-	856.3	-	-	-	-	-

Chapter 5

Results and discussion

This chapter showcases the findings of the experimental campaign using 3M Novec 7200 Engineered Fluid. The measurements were conducted in the flat-bottom cylindrical plexiglass cell, displayed in Figure 4.4, which was pressurised through the active-pressurisation system developed for this campaign and detailed in section 4.1.1. The experimental tests were performed under different procedures and sloshing conditions (section 4.4).

This chapter starts with an overview of the experimental procedure through the results extracted for the test case ID 15. Here the characteristic thermal effects are discussed, with the impact of each phase preceding sloshing assessed via the velocity fields extracted by the PIV technique. Afterwards, the main conclusions of the performed experiments are reviewed in two sections.

Section 5.1 discusses and overviews the system's evolution before, during and after active-pressurisation. Therefore, the thermal stratification, pressurisation and relaxation phases are analysed to evaluate the pressure changes in the pressurant reservoir and sloshing cell. Lastly, section 5.2 introduces the sloshing measurements, where the pressure change in the partly filled cell subjected to lateral forcing is assessed. The interface's thermodynamic state is appraised based on the liquid's bulk motion and free surface displacement for a given sloshing regime. Additionally, the pressure and temperature evolution results are interpreted for a specific experimental procedure for each sloshing point. Here, in section 5.2.4 the initially proposed objectives and research questions are outlined, shedding light on them through the side-by-side comparison of the characteristic pressure drop under sloshing for the baseline test cases.

Figure 5.1 depicts the absolute ullage pressure evolution in the sloshing cell for test case ID 15, with the smoothed signal extracted through the Savitzky-Golay filter. This measurement was conducted under procedure baseline I and is the perfect example to showcase the philosophy behind the defined experimental procedures. Here the most prevalent stages may be outlined: (a) the initial thermal stratification, (b) the pressurisation phase, (c) the relaxation phase for Δt_{relax}, and (d) sloshing initialisation at $t = 0$ s.

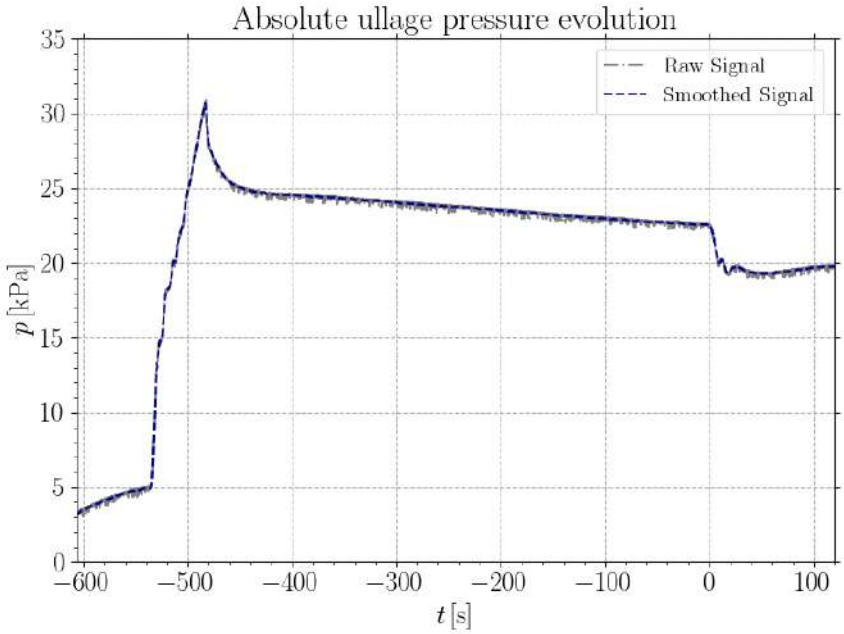

Figure 5.1: Typical sloshing cell pressure evolution as a function of time. The values are here for experiment case ID 15. Time has been set to zero at slosh initiation.

The initial thermal stratification stage starts after closing the vacuum port valve of the sloshing cell. This is outlined in Figure 5.1 between $-607 < t < -534$ seconds. As such, this leads to an initial settling of the system of approximately $\Delta t_{\text{strat}} \approx 73$ s. Here, the system rises in pressure due to external heat fluxes, reaching a pressure of $p = 5.30$ kPa, corresponding to an interface temperature of $T_i = 273.75$ K before the pressurisation phase ($t = -534$ s). Afterwards the pressurisation commences, up until $t = -482$ s leading to a final pressure of $p = 30.52$ kPa for a cycle of approximately $\Delta t_{\text{press}} \approx 52$ s. At this point, the ball valve closes, and the pressurant mass flow stops, which brings the system to a relaxation phase characterised by an exponential pressure decay. At $t = 0$ s, the sloshing motion is initiated, leading to a violent pressure drop within the initial 20 seconds. For this specific case, a planar wave sloshing excitation (section 4.4) was selected. The excitation endures a total of 120 s. Still, for application purposes, only time scales $t < 20$ s are important since the pressure fluctuations due to sloshing-induced mixing are more significant here. Hence, one can conclude that in the current experiment, the cell's thermodynamic evolution under sloshing, is a function of the previous experimental stages.

To evaluate the system's overall behaviour throughout the different experimental phases, one can resort to the averaged PIV velocity fields extracted from test case ID 15. Such analysis is exceptionally pertinent, as more than withdrawing quantitative information

regarding the velocity magnitude, it is possible to assess the liquid's bulk motion.

As stated in section 2.2, a thermal stratification must arise to appraise sloshing's impact on the ullage pressure. This is the primary phenomenon behind the characteristic pressure drops. Such might derive from natural convection and/or conduction mechanisms within the cell. For such reason, as the cell fills with liquid HFE-7200 at an average measured temperature of $T_0 \approx 239$ K across all the test cases, natural convection is expected to occur along the distinct stages. Specifically, because the cell walls are significantly warmer, which drives these convective flows. Moreover, some disturbances near the interface might arise as hot vapour is injected into the cell to reach the desired pressure threshold. This analysis is displayed in Figure 5.2 for each experimental phase, where the liquid yields distinct dynamic behaviours.

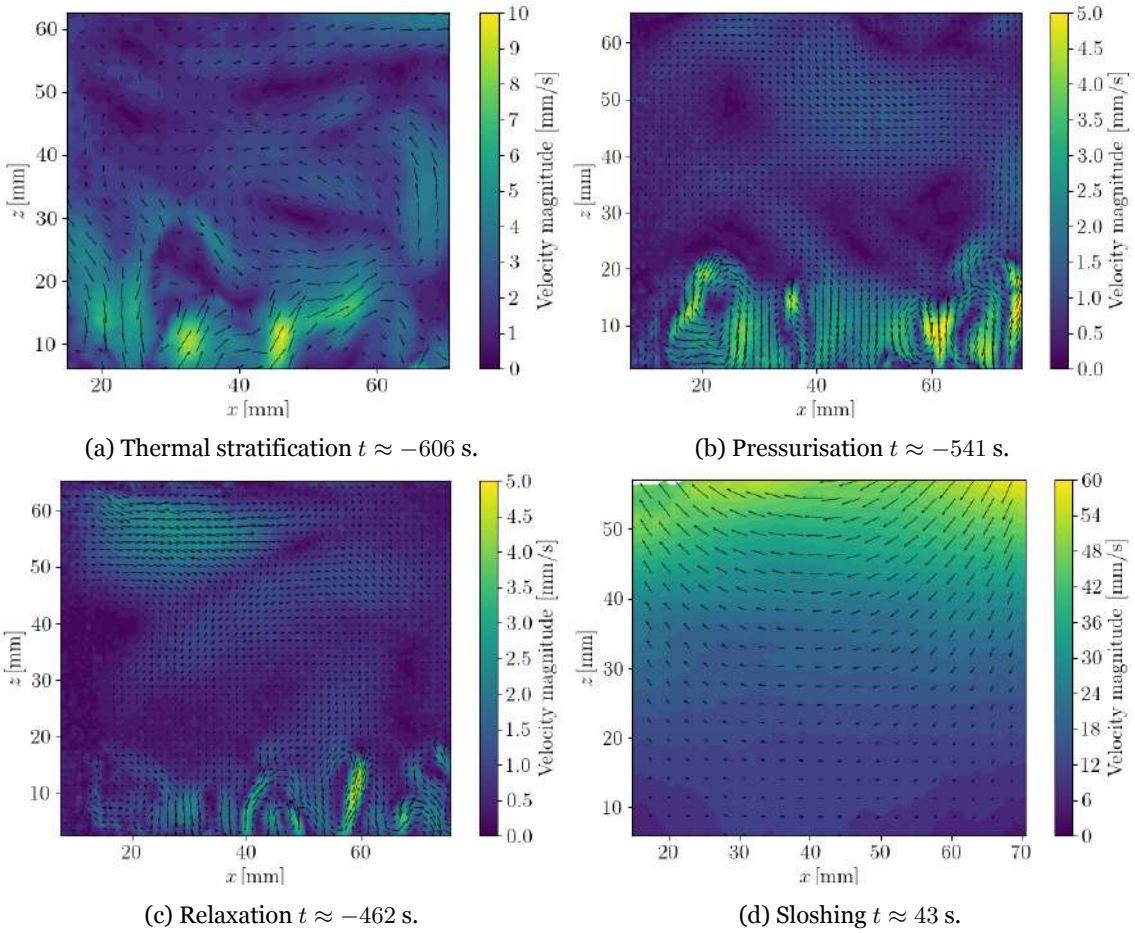

(a) Thermal stratification $t \approx -606$ s.

(b) Pressurisation $t \approx -541$ s.

(c) Relaxation $t \approx -462$ s.

(d) Sloshing $t \approx 43$ s.

Figure 5.2: Moving average of the velocity magnitude and vector fields for test case ID 15. Each computed over thirty consecutive frames, except for the sloshing phase (d) determined from five consecutive frames within half wave period.

Figure 5.2a displays the thermal stratification phase, where convective flows dominate the liquid region, especially near the bottom, where the velocity peaks at approximately 9.6

mm/s. These convective flows are also found at the pressurisation stage, in Figure 5.2b. Still, for this case, the maximum velocity magnitude is 5.0 mm/s, and a uniform field of convective flows arises near the bottom comparably to the previous phase. Additionally, an ascent motion is visible near the right wall, transporting liquid along the border to the interface. In Figure 5.2c, the bottom fluxes lose strength while a considerable velocity field arises near the interface introducing a mixing effect in the liquid's upper layers. The possible reasons emerge from surface disturbances due to the pressurisation jet impinging the free surface or condensation droplets falling from the pressurisation line and top cover. Lastly, in Figure 5.2d, the planar wave's mean velocity field is displayed, showcasing the sloshing-induced mixing capability.

Table 5.1 summarises the conditions of the performed experiments through the extracted periods of each phase. The maximum pressure at the pressurisation end is also displayed.

Table 5.1: Summary of the experimental time and tank pressure at the pressurisation end (p_{max}) for the performed experiments.

Test ID	Slosh point	Procedure	Δt_{vacuum} [s]	Δt_{strat} [s]	Δt_{press} [s]	Δt_{relax} [s]	Δt_{slosh} [s]	p_{max} [kPa]
1	P_1	I	35	107	2	30	120	31.14
2	P_1	I	45	97	49	32	120	25.62
3	P_1	-						
4	P_3	I	47	88	57	39	120	35.14
5	P_2	I	35	53	46	30	120	28.41
6	P_1	I	32	57	52	33	120	25.89
7	P_3	I	44	87	48	36	120	29.99
8	P_2	I	43	81	52	13	120	27.51
9	P_1	II	31	85	30	5	120	30.54
10	P_3	II	42	72	35	0	120	30.31
11	P_2	II	39	67	69	0	120	29.90
12	P_3	Baseline I	35	68	55	504	120	30.60
13	P_3	Baseline II	47	68	66	299	120	30.52
14	P_3	-						
15	P_1	Baseline I	45	73	52	482	120	30.52

5.1 Pressurisation and relaxation measurements

Figure 5.3 displays the system's time-wise evolution for the baseline experimental case ID 15 throughout the pressurisation and relaxation phases. Here the absolute ullage pressure evolution for the sloshing cell is shown in Figure 5.3a, while the pressurant reservoir pressure is indicated in Figure 5.3c. Regarding the temperature acquired from the thermocouples displaced across the experimental setup, it is possible to verify the thermal evolution of the cell's cover and walls in Figure 5.3b. At last, Figure 5.3d outlines the temperature measured in the pipeline at the ball valve inlet and the heater surface, which is in direct contact with the line downstream of the valve.

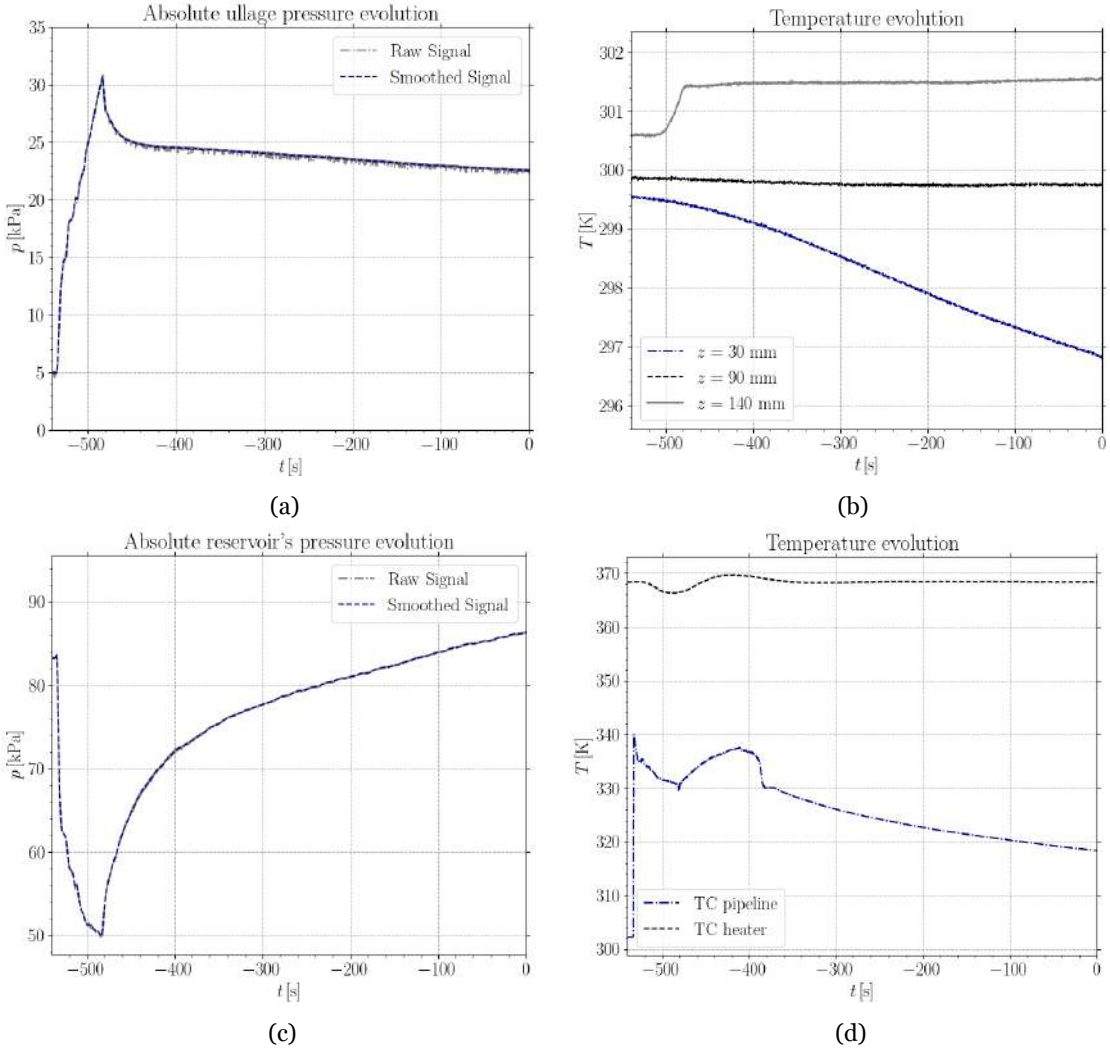

Figure 5.3: Experiment case ID 15: sloshing cell absolute pressure (a) and temperature (b), pressurant reservoir absolute pressure (c) and pressurisation line and heater temperature (d) during pressurisation and relaxation phases.

The absolute ullage pressure evolution during the pressurisation stage displays an approximately linear trend and, for this specific test case, was achieved at a rate of 0.485

kPa/s. For this experimental campaign, consistent pressurisation is critical to minimise the jet impingement of the free surface (Figure 5.4a-5.4b). To do so, the valve must be operated carefully. During this phase, condensation occurs since the superheated HFE-7200 vapour from the high temperature and pressure reservoir is injected into the cell's low-temperature environment. Beyond that, a considerable part of the vapour heat goes into the tank walls and does not contribute to the pressure increase (Figure 5.4c-5.4d). Remarkably, the high liquid volumes extracted and measured at the end of each experiment and depicted in Table 4.7 are verified to arise mainly from this stage. Such a phenomenon is highly undesirable because the droplets pierce the free surface and mix it down to multiple depth levels. Consequently, even prior to sloshing, the liquid's interface already suffered some degree of induced mixing, leading to premature destratification. Which evidently, dampens the sloshing-induced mixing capability. This undesirable phenomenon was already highlighted in the velocity maps for case ID 15 (Figure 5.2c), where the near interface velocity field arises from these disturbances.

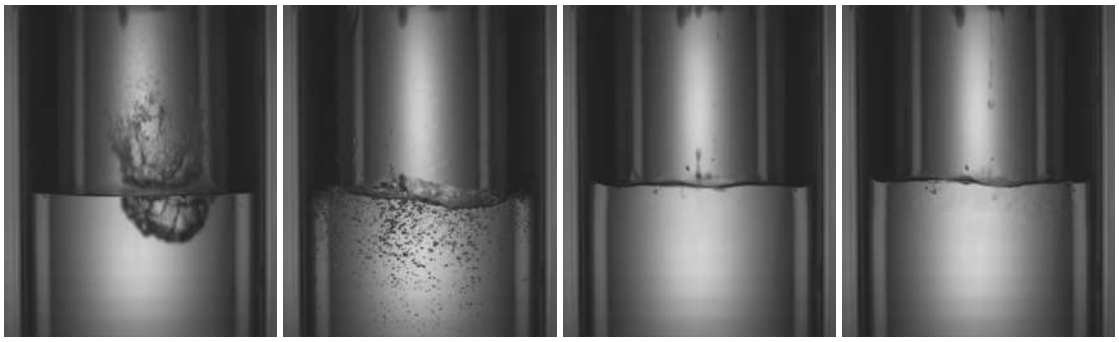

(a) (b) (c) (d)

Figure 5.4: Jet impingement of the free-surface (a), (b) and condensation droplets (c), (d) throughout the pressurisation phase for test case ID 1. The significant pressurisation rate ($\Delta t_{\text{press}} \approx 2.0$ s) for this experiment leads to a substantial impingement of the jet on the free surface.

Evaluating the pressurisation in terms of energy exchange is the clearest way to understand the pressure drop at the pressurisation end. The cell is pressurised due to the specific enthalpy and mass of the injected pressurant vapour, which enters the control volume of the cell's ullage. However, at the same time, energy leaves due to heat transfer to the tank wall and cover and phase change in the form of condensation. Ergo, once the inflow is stopped, the energy of the vapour system decreases further due to the ongoing heat transfer and phase change.

Regarding the thermal evolution of the cell's cover, Figure 5.3b outlines a meaningful increase of approximately 1 K during the pressurisation stage. This arises from the large pressurisation line surface area in direct contact with the cover at the threaded inlet con-

nection and the heat transported from the ullage to the cover. Consequently, once the superheated vapour flows to the cell, a temperature rise occurs. Additionally, at $z = 30$ mm, a drop rate in temperature is showcased, mainly due to the fact that the filled liquid has an initial temperature of $T_0 \approx 237$ K. On the other hand, the thermocouple at $z = 90$ mm remains at a constant temperature of 299.8 K and does not capture the hot ullage vapour or the cold liquid.

The pressurant reservoir during the experimental campaign remains approximately at a saturated steady state. For this specific case, it attains an initial vapour pressure of $p = 83.0$ kPa, corresponding to a saturated temperature of $T = 342.4$ K. Once the pressurisation stage starts, a steep drop takes place, and the reservoir's pressure reaches a minimum of $p = 50.5$ kPa. Afterwards, since the power supply remains at a fixed power condition, the pressure rises exponentially to the previous state. This means that there is still enough liquid mass inside the reservoir to vaporise and reach the desired threshold. Interestingly, the measured temperature in the pipeline during the initial pressurisation stage is 340.0 K, which agrees reasonably well with the theoretical saturation vapour temperature at the reservoir. Along this same stage, it measures a minimum temperature of 329.7 K, corresponding to a pressure of 54.36 kPa. Since the measured line temperature during the pressurisation stage is identical to the reservoir's saturation temperature, it can be concluded that the efforts to insulate the pipe upstream of the ball valve were fruitful.

5.1.1 Pressurisation model results

Resorting to the 0D model, it is possible to develop a comparison for a pressurisation cycle with the results extracted from the experiment itself. Since there is no access to the real gas properties for HFE-7200, the ideal gas model and the respective derived set of the modelling equations are applied.

The pressurisation procedure relied upon the manual operation of a ball valve located on the pressurisation line. To avoid the liquid's surface impingement from the vapour jet, a pressure of approximately $p = 30.00$ kPa was reached at the end of 60 seconds. Therefore, during this stage, the ball opening angle would change, increasing over time to meet the procedural constraints. Evidently, the valve opening angle is not recorded during the experiment, and moreover, to be able to model partially opened valves, it is mandatory to have access to the exact pressure loss coefficient for each angle, which is

not the case. Hereupon, from the cell's pressure at pressurisation end ($t \approx -483$ s) and the pressurisation cycle of $\Delta t_{\text{press}} \approx 52$ s, the ball valve minor loss rate (ξ) was fixed at a constant value that yields the desired absolute ullage pressure evolution.

Figure 5.5 compares the measurements from case ID 15 with the 0D model prediction. According to the simplified model, the sloshing cell would attain a final pressure of approximately $p \approx 30.52$ kPa starting from a saturated condition of $p \approx 5.70$ kPa. To answer this constraint, the ball valve minor loss coefficient would need to be in the order of 4×10^6, which is four orders of magnitude larger than the usually measured coefficients for small opening angles of ball valves [58].

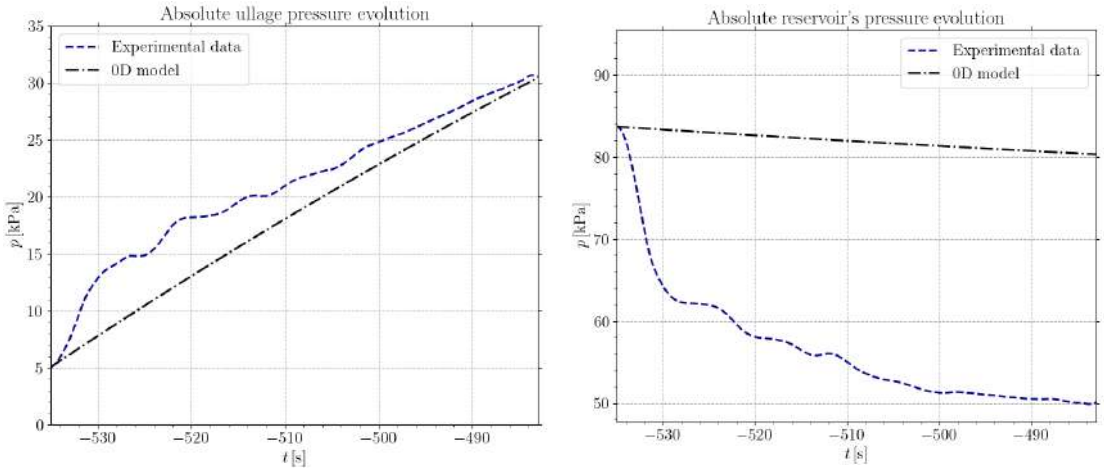

(a) (b)

Figure 5.5: Comparison between the experimental case ID 15 measurements and the pressurisation 0D model prediction for the pressure evolution within the sloshing cell (a) and the pressurant reservoir (b).

5.2 Non-isothermal sloshing measurements

The non-isothermal sloshing measurements discussed here are the vital results that describe the characteristic pressure drops in tanks under dynamic conditions. Such phenomena that arise from the abnormal thermodynamics within a pressurised vessel have a focal point in the interaction of sloshing dynamics with heat and mass transfer processes [14, 19].

Therefore, to evaluate this thermodynamic evolution, it is crucial to ensure that the closed tank is adequately pressurised. This condition was already discussed in section 5.1, and the experimental results here are built from it. In contrast, free surface motion, labelled sloshing [24], is the other vital requirement to visualise the phenomenon under study.

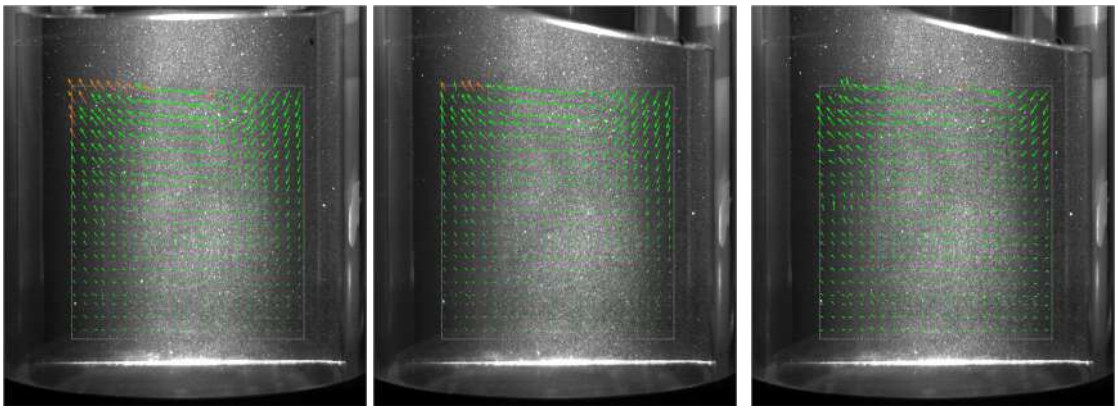

(a) Flat free surface. (b) Initial displacement. (c) Peak wave amplitude.

Figure 5.6: Instantaneous velocity vector fields for the test case ID 15, calculated over three consecutive frames, where stable planar sloshing is visible.

This liquid's dynamic behaviour is responsible for transporting the liquid at the bulk to the interface. Consequently, it is crucial to start by analysing its mixing capability.

Figure 5.6 displays the instantaneous velocity vector fields in the liquid's bulk region with the captured background image for the test case ID 15 when the liquid's motion has already developed into stable planar waves. The results are extracted for a region of interest located sufficiently far from the walls and interface to minimise their effects that may lead to erroneous velocities [69]. Figure 5.6a introduces the frame at which the free surface is flat and gaining momentum. Here it is clear that the liquid's velocity field follows a pendulum-like behaviour, characterised by large velocities near the free surface, which are damped out as we move towards the bulk. Nevertheless, one can appreciate that the vertical velocity component is substantial even at half the fill height, especially towards the walls. Subsequently, in Figure 5.6b, the liquid loses momentum, while Figure 5.6c showcases the peak wave amplitude instant where the velocity field reaches a plateau condition before regaining momentum in the opposite direction.

This analysis (Figure 5.6) can be further expanded by plotting the corresponding velocity magnitude maps for each of the instantaneous snapshots, as displayed in Figure 5.7. These colourmaps, where the coordinate system originates at the sloshing cell's left bottom corner, indicate precisely the extent to which the motion disrupts the stationary bulk liquid.

Figure 5.7a illustrates a velocity threshold of approximately 78 mm/s reached above $z \approx 50$ mm. It is clear that near the centreline ($x \approx 40.5$ mm), the motion is dominated by a horizontal component transporting the liquid towards the wall, which then is carried up to

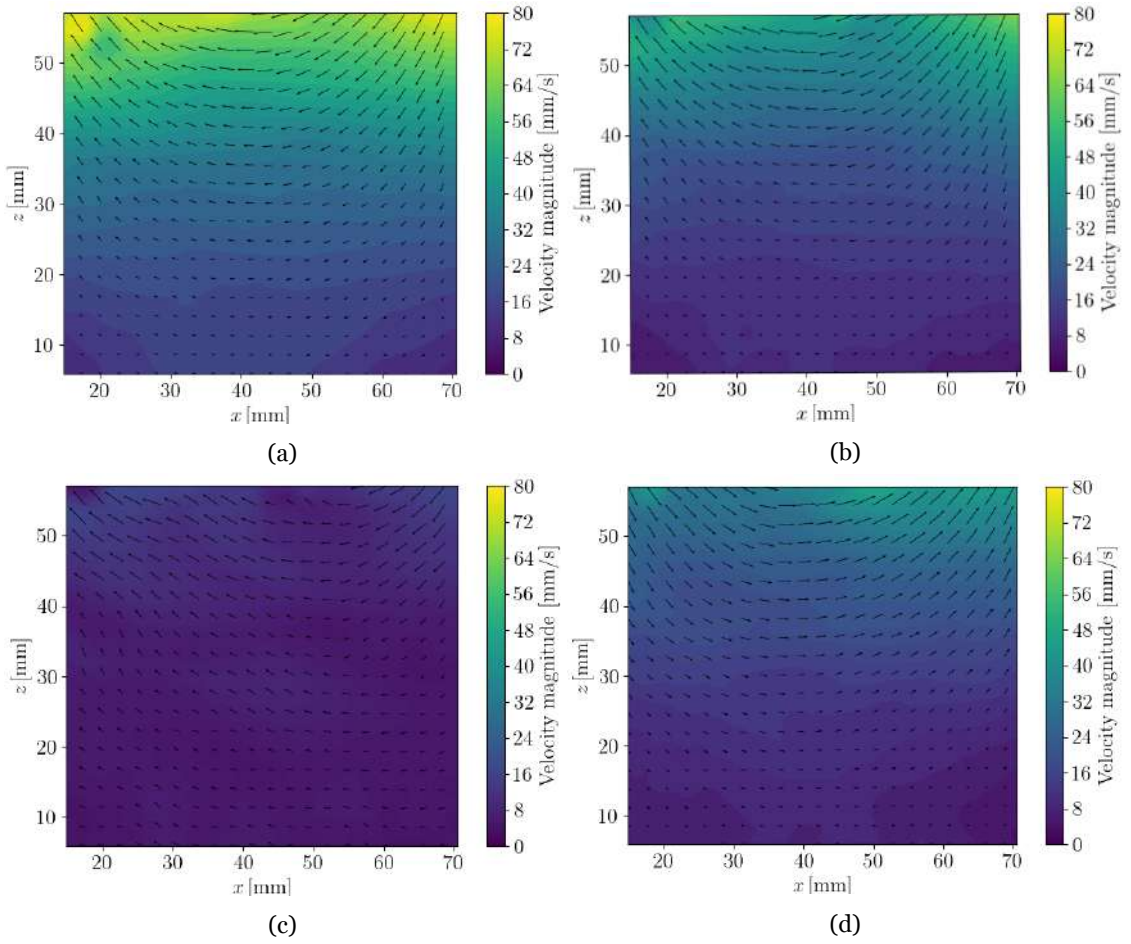

Figure 5.7: Instantaneous velocity magnitude and vector fields for the test case ID 15, calculated over four consecutive frames, for stable planar sloshing.

the interface by a prevailing vertical component at $x \approx 30$ mm. Moreover, even at $z \approx 30$ mm, the velocity magnitude is roughly 38 mm/s, which is considerable for a region far from the interface. Afterwards, in Figures 5.7b and 5.7c there is a deceleration trend since the wave reaches its maximum amplitude, quite visible at Figure 5.7c with a prevailing velocity in the order of 7 mm/s. Lastly, a subsequent frame (Figure 5.7d) where the liquid regains momentum in the opposite direction is showcased for completeness.

Figure 5.8 displays test case ID 6 in which both liquid and ullage were recorded to qualitatively assess the free surface displacement under sloshing point P_1. This perspective reinforces the previous analysis and concludes that under this point ($A_f/R = 0.025$, $\omega/\omega_{11} = 0.893$), a motion with instabilities and wave-breaking conditions should not arise, where the sloshing-induced mixing is controlled by the velocity fields showcased by Figure 5.7. Unfortunately, this is not the case for all planar experiments and is further analysed in section 5.2.1. For this sloshing point, the angular amplitude of surface inclination should become constant with a maximum theoretical wave amplitude $b \approx 7.87$ mm, determined

by equation 2.6.

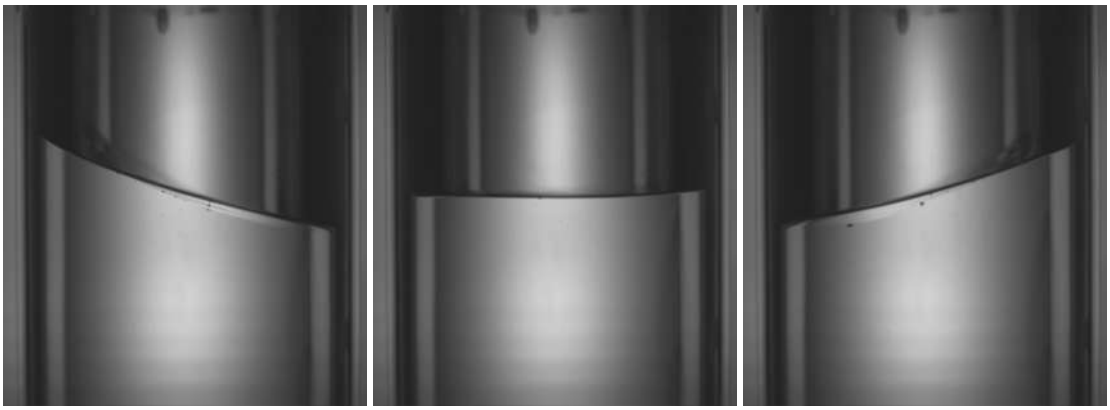

(a) (b) (c)

Figure 5.8: Free surface displacements for the test case ID 6 under planar sloshing.

This analysis must be performed for the other sloshing points (section 4.4) particularly because as soon as the motion frequency rises to near resonance conditions, surface instabilities emerge [33]. This means that besides the velocity fields that transport properties within the liquid, droplets, jets and splashing could ensue and amplify the sloshing induced-mixing. Unfortunately, for points P_2 and P_3 the velocity fields were not characterised resorting to the PIV technique, as they are outlined as unstable motions where tridimensional effects are important and would not be captured under the 2D method employed in this project. Therefore, only a qualitative analysis can and must be performed.

Figure 5.9 displays test case ID 5 under the sloshing point P_2 ($A_f/R = 0.025$, $\omega/\omega_{11} = 0.922$). Here a chaotic regime is present, characterised by an unstable motion. A dynamic behaviour defined by a concoction between high amplitude planar waves and rotational motion about the normal axis could be seen throughout the experiment. Occasionally,

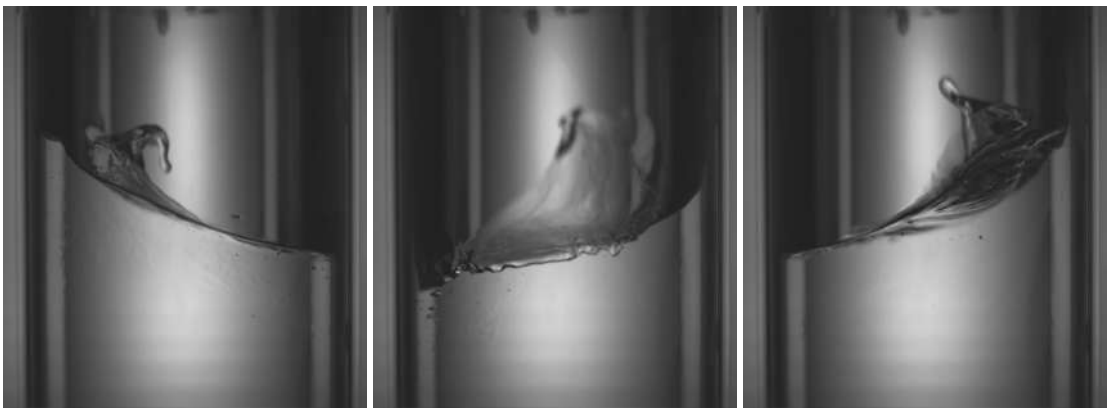

(a) (b) (c)

Figure 5.9: Free surface displacements for the test case ID 5 under chaotic sloshing.

the wave amplitude would be such that breaking would take place where droplets and jets would arise from the free surface, as displayed in Figures 5.9a and 5.9c.

Lastly, Figure 5.10 introduces the rotational motion present during sloshing point P_3 ($A_f/R = 0.025$, $\omega/\omega_{11} = 1.041$) for test case ID 13. Here the stable swirling motion is already established after gaining angular momentum, with a theoretical average swirl wave amplitude $b \approx 28.35$ mm, according to section 2.1.2.

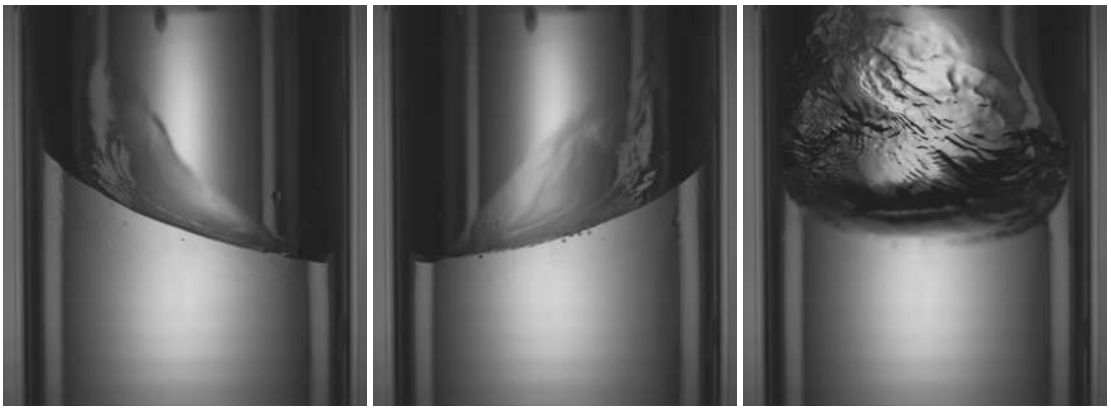

(a) (b) (c)

Figure 5.10: Free surface displacements for the test case ID 13 under rotary sloshing.

Clearly, over Figures 5.6-5.10 sloshing's power is duly outlined, and no doubts rest upon its capability of efficiently mixing the liquid within the pressurised vessel. Although the velocity fields of sloshing points P_2 and P_3 were not defined, through the qualitative analysis, it is possible to assess their violent nature and superior mixing degree when compared with stable waves. Therefore, the following sections will evaluate a specific test case for each sloshing point.

5.2.1 Planar waves sloshing regime

Figure 5.11, refers to a measurement conducted in sloshing point P_1 ($A_f/R = 0.025$, $\omega/\omega_{11} = 0.893$) corresponding to test case ID 9. For this specific experiment, procedure II is employed, with no relaxation period after reaching the pressure threshold of approximately $p \approx 30$ kPa. Consequently, once this value is satisfied, the ball valve is closed, ending the pressurisation phase, and the shaking table is turned on. The liquid's temperature before filling the cell was measured at $T_0 \approx 235$ K.

From Figure 5.11a it is possible to determine that at the end of the pressurisation phase $t \approx -5.0$ s the achieved pressure is $p = 30.54$ kPa. Likewise, one can conclude that slosh-

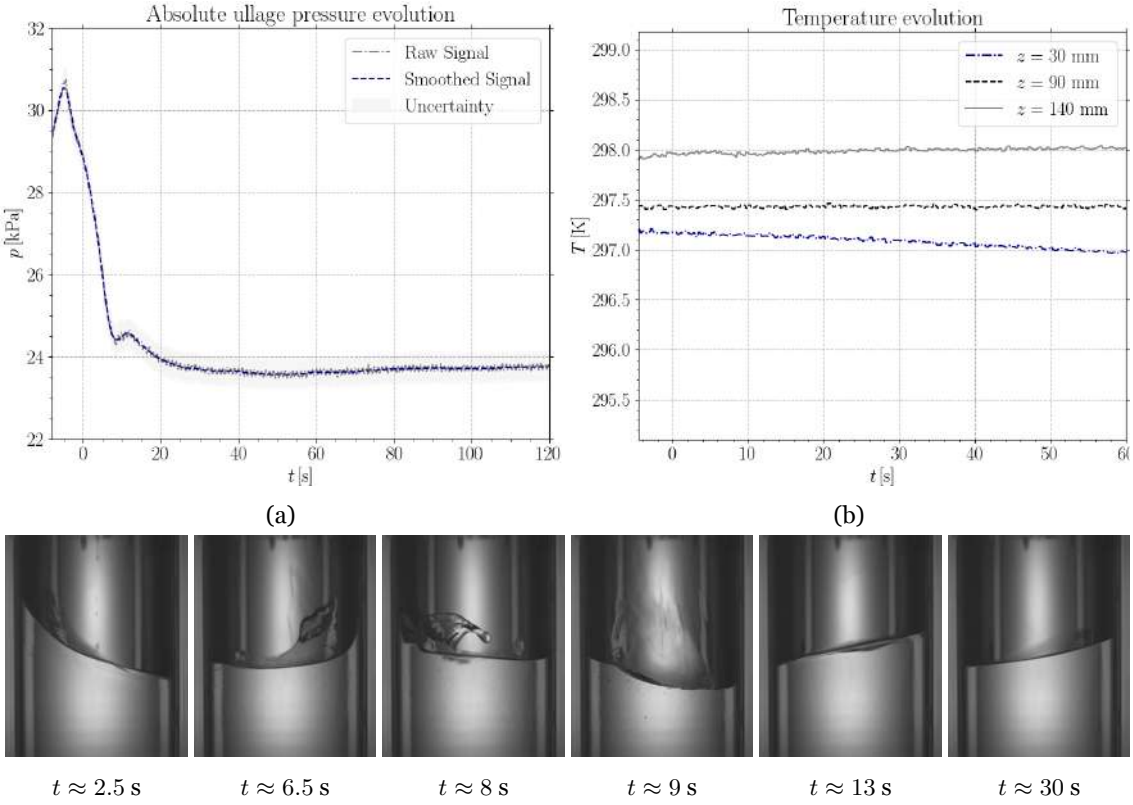

Figure 5.11: Test case ID 9: ullage pressure evolution (a) and temperature evolution at the sloshing cell walls and top-cover (b) as a function of time. Time has been set to zero at slosh initiation.

ing was not properly started at this stage since the pressure peak does not coincide with $t = 0$ s. This showcases the most challenging factor of this procedure which must be performed in pairs, or the displayed delay will be unavoidable for the current experimental setup configuration. Nevertheless, a consistent pressure drop was achieved, meaning this mishap did not significantly affect the results and the pressure drops from relaxation and sloshing-induced mixing collapse together. The minimum pressure of $p = 23.57$ kPa is reached at $t = 53.60$ s, yet after the initial 30 s, the pressure drop rate collapses to nearly zero even if sloshing proceeds for a total of 120 s. Remarkably, roughly at $t = 6$ s, the pressure evolution yields a decrease in the drop rate, followed by an increase in the absolute pressure value. Hereupon, as one might foresee, it is critical to perform a footage evaluation of this specific drop which yields a peculiar behaviour for a planar wave regime. The pictures show that once sloshing unfolds, the initial motion is characterised by small amplitude planar waves, but throughout the first periods, condensation droplets fall from the pressurisation inlet ($t \approx 2.5$ s). As these droplets impinge on the free surface, it is possible to assess that instabilities develop, and the smooth planar behaviour is lost, from which a chaotic motion arises ($t \approx 6.5$ s). At this stage, a positive pressure drop rate rises, likely because now the free-surface dynamics are characterised by an intermediate amplitude

swirl wave ($t \approx 9.0$ s) rotating along the ullage walls, which are warmer compared to the liquid region. Therefore, evaporation must be taking place, leading to the pressure build up due to the disruption in the planar motion. This positive drop rate subsides at $t \approx 13.0$ s since, at this point, the highly chaotic motion collapses, losing energy. After collapsing, the displacement tends again towards planar waves. Still, due to the induced rotational velocity from the surface break up, until the end of the excitation the dynamics are outlined by planar waves with rotational velocity along the tank's normal axis ($t \approx 30$ s). All in all, in this experiment, the pressure decays a total of 22.82%. Regarding the thermal evolution at the cell's wall and cover represented in Figure 5.11b one can conclude that the outside is virtually insensitive to the thermal evolution within the tank, and only the bottom thermocouple ($z = 30$ mm), in contact with the bulk liquid, slightly varies in time with a linear decay of approximately 0.00391 K/s.

5.2.2 Chaotic sloshing regime

Figure 5.12 displays the results for sloshing point P_2 ($A_f/R = 0.025$, $\omega/\omega_{11} = 0.922$) corresponding to test case ID 5. In this experiment, procedure I is employed, with a filling time interval of approximately $\Delta t_{\text{filling}} \approx 300$ s and a relaxation period of $\Delta t_{\text{relax}} \approx 30$ s after the end of the pressurisation phase.

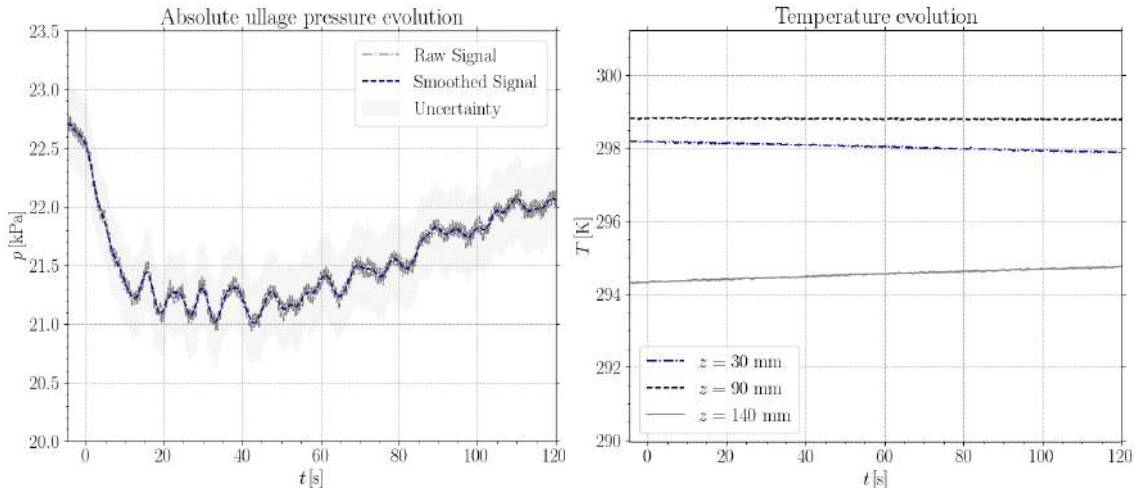

(a) (b)

Figure 5.12: Test case ID 5: ullage pressure evolution (a) and temperature evolution at the sloshing cell walls and top-cover (b) as a function of time. Time has been set to zero at slosh initiation.

Figure 5.12a represents the absolute ullage pressure evolution from where it is possible to verify that preemptively to commence sloshing ($t < 0$ s), the pressure continuously de-

creased and did not reach a quasi-steady equilibrium state. Such arises from unavoidable heat losses, where the superheated ullage vapour exchanges heat with the walls, cover and liquid, leading to condensation and a decrease in temperature. Here at $t = 0$ s the pressure is $p = 22.53$ kPa reaching a minimum of $p = 21.09$ kPa at $t = 42.8$ s, meaning the total pressure decay is 6.39%. Interestingly, first, the chaotic motion slightly disrupts the initial thermal stratification for the first 10 seconds, after which it loses effectiveness, and the pressure rises, indicating that evaporation might occur as the wave climbs the wall. Subsequently, an approximately periodic pressure behaviour settles in the cell for the remainder of the sloshing excitation. Critically, this periodicity hints that a connection must exist with the free surface dynamics, which can be connected to this analysis by resorting to the recorded footage. Regarding the thermal evolution at the cell's wall and cover shown in Figure 5.12b, it is important to emphasise the temperature measured by the top-cover thermocouple ($z = 140$ mm), which is below the temperature of the walls. This occurs since the slow filling procedure increases the exposure time of the aluminium cover to the highly subcooled liquid. Throughout sloshing, it showcases an increasing linear trend of approximately 0.00383 K/s, meaning the outside heat flux through the cell cover increases over time, amplifying the pressure build-up within the cell.

Figure 5.13 demonstrates the rate at which the ullage pressure drops between 10 and 20 seconds, which is when the periodic pressure shift occurs. The drop rate is calculated through a central difference scheme, where the smoothed pressure signal is used. It is possible to correlate such phenomena with sloshing through the experimental footage. From the moment sloshing unfolds to $t \approx 10$ s, moderate amplitude waves develop coupled with angular momentum where instabilities at the surface arise, leading to enhanced surface layer mixing. At this moment, the free surface collapses to small amplitude and irregular motions, after which it regains momentum leading to high amplitude waves with rotational speed between $11 < t < 15$ seconds. From the footage, it is clear that the waves travel along the ullage walls and touch the cell's cover, which corresponds to a pressure increase by the extracted measurement. Therefore, it could mean the cold liquid evaporates as it mixes and comes into contact with the warmer ullage wall reaching a maximum pressure drop rate of approximately 0.09 kPa/s. Next, the motion collapses and between $16 < t < 18$ seconds showcases an extremely asymmetrical nature with surface breaking leading to plunging jets and droplets that perforate the interface. At this stage, a negative drop rate is established possibly due to the jet's capability of mixing the interface properties up to moderate depths.

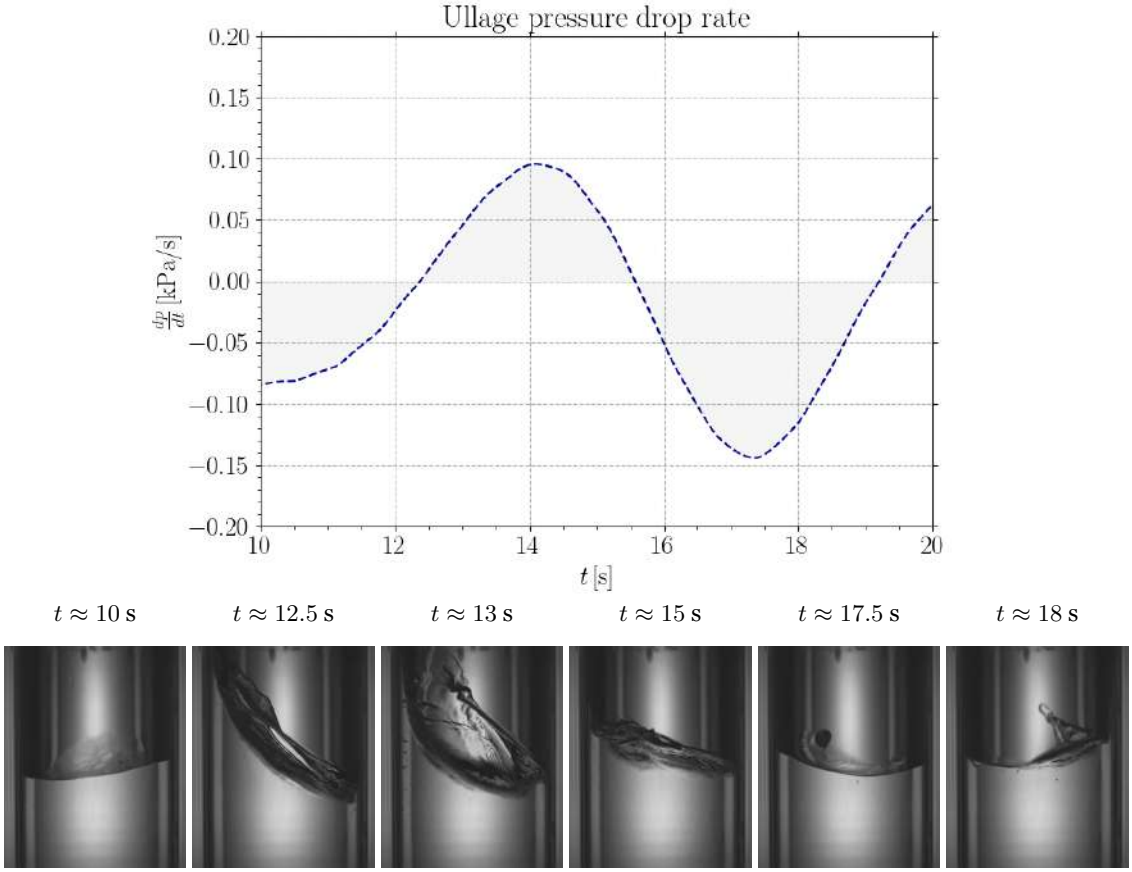

Figure 5.13: Rate of pressure change for case ID 5 in between $10 - 20$ s after slosh initiation. The free surface displacement is correlated to the ullage maximum pressure drop rate by sampling the captured footage.

5.2.3 Swirl sloshing regime

Figure 5.14 represents the measurement conducted in sloshing point P_3 ($A_f/R = 0.025$, $\omega/\omega_{11} = 1.041$) corresponding to test case ID 13. For this specific experiment, procedure baseline II is employed, where a relaxation period of approximately 300 s is used. At the beginning of the filling process, which takes approximately 30 seconds, the liquid's temperature is measured to be $T_0 \approx 239$ K.

Figure 5.14a outlines the absolute ullage pressure evolution in the sloshing cell between $-5 < t < 120$ seconds, where the time is set to zero at slosh initiation, below $t < 0$ s, the pressure displays a nearly stable behaviour defined by a value of approximately $p = 22.40$ kPa at $t = 0$ s. Hereupon, in contrast with the results of Figure 5.12 in which the relaxation period does not allow to arrive at a stable state, for this specific case, the relaxation period of 300 seconds is enough to reach a quasi-thermodynamic equilibrium before sloshing the tank. Once sloshing starts, a violent pressure drop arises within the first 20 seconds, specifically at $t = 12$ s. Resorting to the recorded footage, it can be

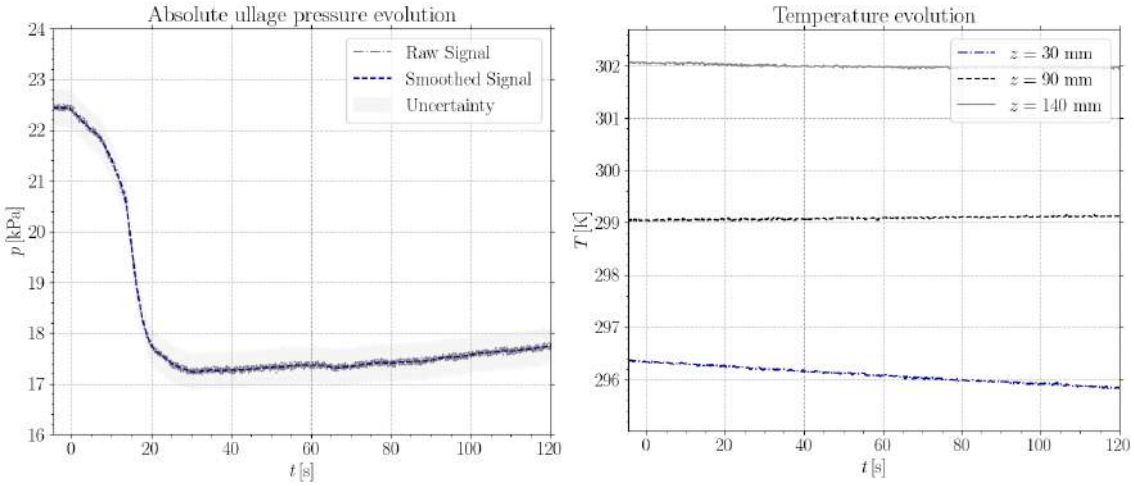

(a) (b)

Figure 5.14: Test case ID 13: ullage pressure evolution (a) and temperature evolution at the sloshing cell walls and top-cover (b) as a function of time. Time has been set to zero at slosh initiation.

seen at this precise instant that a high amplitude and angular momentum stable swirl wave grows with a peak close to reaching the top cover of the sloshing cell (Figure 5.15). Moreover, wave-breaking happened near the crest. This wave gains momentum at $t \approx 11$ s before arriving at this stable condition after 42 sloshing periods ($42T_\omega$). Although this liquid's swirl wave lasts after the initial violent drop, pressure reaches a minimum of $p = 17.23$ kPa at $t = 31.1$ s, which translates into an overall ullage pressure change of 23.08%. After this point, the liquid has already converged to a uniform temperature, and a new thermodynamic equilibrium is reached. Seemingly, this state is not held constant for long since unavoidable heat leaks occur. Therefore after $t > 65$ s, a pressure rise within the ullage can be tracked where the most likely cause arises from the evaporation of the liquid at the cell's warm walls. Such can be extrapolated from Figure 5.11b where the thermocouple at $z = 90$ mm holds a temperature close to 299 K, with a minor increasing trend. On the other hand, the liquid's region wall thermocouple at $z = 30$ mm displays a modest linear decay of approximately 0.0041 K/s. Despite all that, once again, one can draw the conclusion that the outside is almost unaffected by the heat exchange inside the tank, meaning our time scales are too narrow and the tank wall's thermal inertia too high to retrieve meaningful results with this configuration.

Figure 5.15 highlights the ullage pressure drop rate from the filtered pressure evolution, through a central differences scheme, between $10 < t < 20$ seconds where the most violent pressure change develops. The characteristic swirl motion arises at $t \approx 12$ s, enhancing the sloshing-induced mixing, which develops into a maximum averaged pressure drop

rate of approximately -0.65 kPa/s.

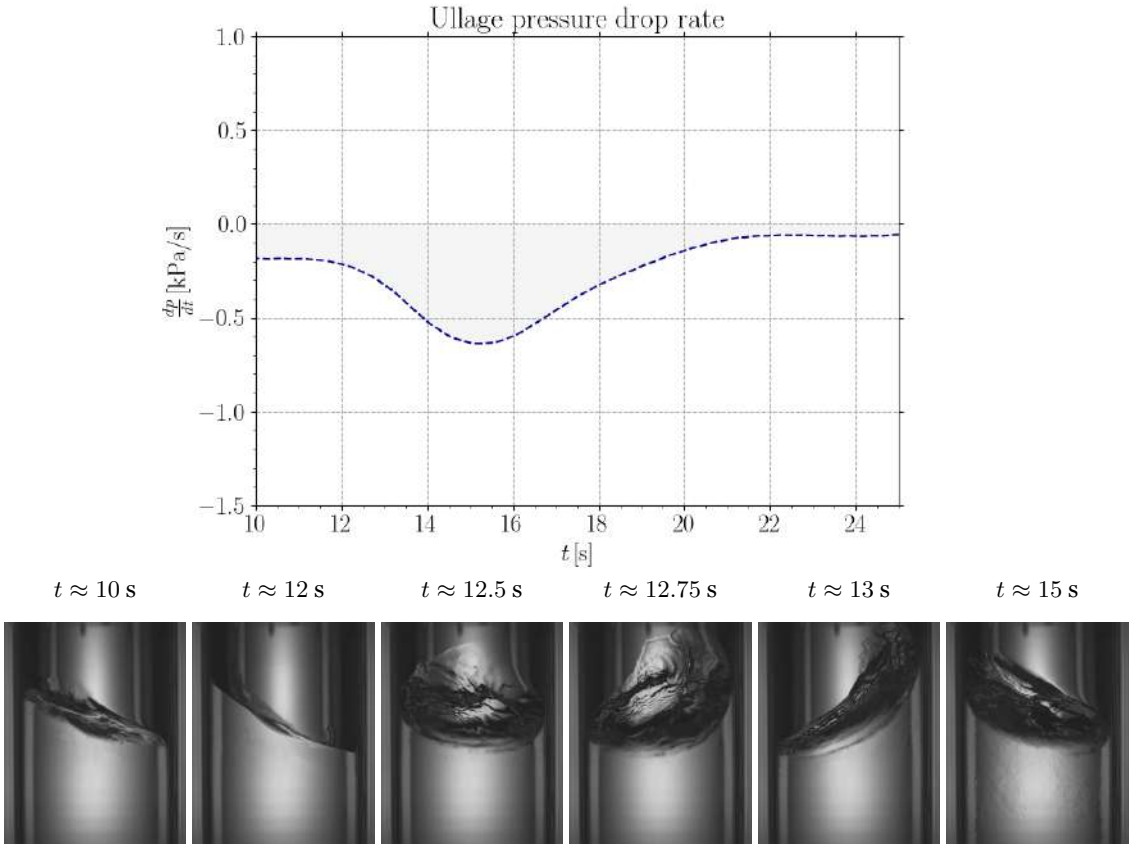

Figure 5.15: Rate of pressure change for case ID 13 in between $10 - 25$ s after slosh initiation. The free surface displacement is correlated to the ullage maximum pressure drop rate through the captured footage.

5.2.4 Characteristic pressure drop

Figure 5.16 shows the non-dimensional pressure evolution for test cases ID 12, 13 and 15. Test case ID 12 was performed under the swirl sloshing regime point P_3 ($A_f/R = 0.025$, $\omega/\omega_{11} = 1.041$) through procedure baseline I. As such, the relaxation period is equal to $\Delta t_{\text{relax}} \approx 480$ s. The same procedure was applied to test case ID 15, which was previously characterised through the PIV technique (Figure 5.7) under point P_1 for planar waves. Lastly, case ID 13 employing baseline II procedure for sloshing point P_3 with a relaxation of $\Delta t_{\text{relax}} \approx 300$ s was deeply analysed in section 5.2.3. In this analysis, the pressure is normalised by taking the ratio between the instantaneous pressure p in the cell and its initial value at $t = 0$ s, defined as p_0 and in Table 5.2. The objective is to assess the pressure change in the ullage due to sloshing and compare its evolution between the particular plotted cases. This way, the outcomes from different procedures and sloshing conditions

are easily comparable.

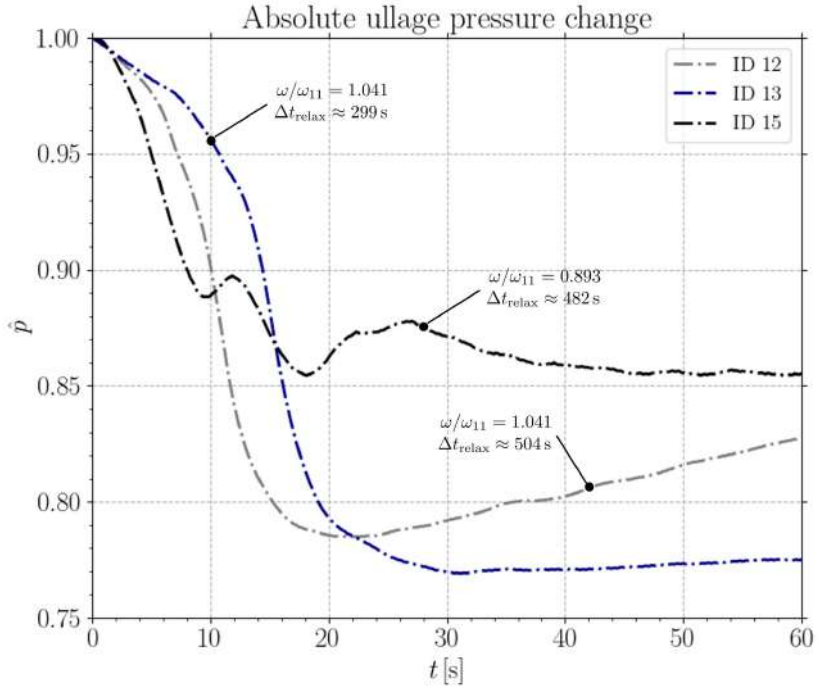

Figure 5.16: Non-dimensional absolute ullage pressure evolution for the test cases ID 12, 13 and 15. Time has been set to zero at slosh initiation.

Table 5.2: Absolute ullage pressure at sloshing initialisation ($t = 0$ s).

	Case ID 12	Case ID 13	Case ID 15
p_0 [kPa]	21.59	22.40	22.53

The initially proposed research question **RQ1** (section 1.1) sought to understand how the system would evolve under distinct sloshing excitation conditions. Even though no temperature measurements were applied throughout the test campaign, the retrieved gauge pressure data, later converted to absolute pressure, allows us to shed some light on this remark. Notwithstanding the step-by-step analysis done up to now, where the sloshing regimes mixing fortitude was duly outlined, Figure 5.16 introduces the most explicit answer to such a question. Here, test case ID 15, where planar waves arise under a forcing frequency of $\omega = 3.00$ Hz, displays a violent pressure drop within the first 20 s, characterised by a minimum pressure ratio of 85.40%. On the other hand, test case ID 12, also displaying a devastating initial drop, was performed with the same procedure, but for sloshing point P_3 where $\omega = 3.50$ Hz and a stable swirl wave develops. The minimum pressure ratio achieved in this case was 78.50%. Therefore, no doubts rest upon the conclusion that the swirl sloshing regime is the most efficient method to destroy the thermal stratification within a pressurised vessel. However, care must be taken since instabilities might arise, for example, from condensation droplets, which modify the motion charac-

teristics and enhance heat transfer by impinging the free surface (section 5.2.1). As such, under non-isothermal sloshing, it is imperative to perform a visual analysis where a transparent sloshing cell must be employed.

The second proposed research question **RQ2** highlights the impact of different initial non-isothermal sloshing conditions. More precisely, variables such as the initial tank pressure (p_0), the thermal gradients within the vessel, and the stratification degree at the free surface (δ_t) play a pivotal role in our problem. Unfortunately, under the current research framework, the retrieved quantitative results do not allow us to unequivocally extract the desired results as the measured wall temperatures did not translate into meaningful results. Even so, under different procedures, which are time-wise well defined, one can extrapolate how these impactful variables evolve and couple with the absolute ullage pressure change. Here test case ID 12 and case ID 13, reply qualitatively to such question. Both were performed for sloshing point P_3 with an initial measured liquid temperature of approximately $T_0 \approx 239$ K. The critical distinction resides in the relaxation period (Δt_{relax}), which differs in 205 seconds. Case ID 12 settles for 504 seconds after the pressurisation, while case ID 13 has a smaller relaxation period of only 299 seconds. From Figure 5.16, ID 12 displays an initial devastating drop, with a minimum pressure ratio of 78.50%. Conversely, case ID 13 achieves a minimum pressure ratio of 76.9%. Since the interface is assumed to be saturated (section 2.4), the liquid at the free surface must have saturation temperature. However, the liquid temperature beneath the interface increases slower than the tank pressure would allow due to the liquid's thermal inertia (section 2.2). Evidently, under the saturation and single-species system assumption, pressure and temperature are connected (section 2.4). Hereupon, as we allow the tank to rest for longer in case ID 12, the temperature at the free surface propagates towards the bulk, leading to a higher degree of thermal homogenisation and a reduction in temperature at the interface due to constant heat exchange with the surroundings. As such, this translates into a difference in the initial absolute ullage pressure p_0 of approximately 1 kPa, meaning the interface temperature for case ID 12 is $T_i \approx 305$ K, while in case ID 13 is $T_i \approx 306$ K [75]. Hereupon, case ID 13 has a steeper thermal gradient or, in other words, a smaller "pocket" of warm liquid at the free surface. Hence sloshing's ability to homogenise the properties within the cell leads to a larger pressure drop for case ID 13 compared to case ID 12.

Chapter 6

Conclusions and future work

6.1 Summary and conclusions

The research developed and showcased in this dissertation addressed the impact of liquid sloshing dynamics in the thermodynamic evolution of pressurised cryogenic propellant tanks, specifically for orbital space launchers. This was accomplished through an experimental characterisation, where a novel small-scale facility was designed and assembled to operate through an active-pressurisation system resorting to non-cryogenic fluids, particularly 3M Novec 7200. The overall goal rested on experimentally identifying sloshing as the primary trigger behind the characteristic pressure drops within pressure vessels. Furthermore, the impact of different sloshing excitations and initial thermodynamic conditions was also appraised.

The approach to the problem began with the assessment of the preeminent phenomenon. Such was achieved by extracting the dimensionless numbers governing the interaction between the pressurised ullage, liquid phase and tank walls. The derived quantities from a scaling of equations (SE) approach shed light on the relevant fluid parameters as well as the impact of heat and mass transfer at the liquid-vapour interface. The similarity analysis yielded satisfactory outcomes for data up-scaling with the core stage's oxidiser and upper stage's tanks of space launchers. From the kinematics, the sloshing regime concept was formulated by fixing the forcing amplitude A_f/R and the dimensionless forcing frequency ω/ω_{11}. Using thermodynamic reference conditions, dynamic similarity concluded that this problem falls within gravity-dominated sloshing conditions where capillary forces influence the dynamic behaviour only slightly ($\mathbf{We} \gg 1$). Lastly, in the heat and mass transfer analogy, the tank's characteristic length proved to play an essential role in leading to significant discrepancies in the dominant effects. Nonetheless, disregarding the tank dimensions and appraising the same length scales between a cryogenic experimental test employing LN_2 and this project facility, an excellent agreement was found, supporting this simple and economical experimental approach to model full-size cryogenic propellant

tanks.

The first step of the experimental setup design was to identify possible layouts, extract operational requirements and evaluate the future applicability of such a facility. Herein, the long-term goal of studying non-isothermal sloshing under microgravity conditions was settled, and the high-level requirements derived for the implementation of this new small-scale experiment in the 80th ESA parabolic flight test campaign. As such, it led to the architecture of a single-species active-pressurisation system employing a transparent sloshing cell. The experimental methods resorted to pressure probes, thermocouples and particle image velocimetry (PIV) measurements.

In the experimental campaign with subcooled HFE-7200 liquid at an averaged temperature $T_0 \approx 239$ K, and an initial fill liquid ratio $h/R = 1.44$, where lateral sloshing was investigated for the fundamental sloshing mode ($\omega_{11} = \sqrt{\xi_{11} g/R} = \sqrt{1.841 g/R} = 21.117$ rad/s) different experimental procedures and sloshing points were investigated. From the experimental procedure point of view, the baseline methods revealed the most indicated as they allowed a quasi-steady condition prior to sloshing, while minimising the operational hardship.

The particle image velocimetry (PIV) measurements allowed to characterise the liquid velocity fields along the different procedure stages. The results outlined in the thermal stratification, pressurisation and relaxation phases show a clear connection between the convective flows and the interaction of the walls, creating the desired thermal stratification at the free surface from natural convection at the boundaries. Likewise, the upwards velocity distribution throughout planar sloshing explained the destratification phenomenon, where the bulk liquid was transported to the interface.

The sloshing dynamics analysis and coupling with the pressure data showcased the following findings: (a) In sloshing point P_1 ($A_f/R = 0.025$, $\omega/\omega_{11} = 0.893$), where stable planar waves should develop, instabilities led to a collapse of its stable behaviour. The hypothesis that condensation droplets within the pressurant line fuelled such transition were found as the most likely cause; (b) For sloshing point P_2 ($A_f/R = 0.025$, $\omega/\omega_{11} = 0.922$), the chaotic motion displayed periodic pressure fluctuations, where the pressure build-up developed the hypothesis that the ullage walls wetting phenomenon may be sufficient to impact the problem; (c) Sloshing point P_3 ($A_f/R = 0.025$, $\omega/\omega_{11} = 1.041$) exhibited the development of a stable swirl wave, representative of the corresponding rotary regime.

Such motion displayed a pressure drop rate enhancement when the high amplitude swirl wave was established at 42 sloshing periods ($42T_{\omega}$).

Finally, the proposed research question were investigated considering three experimental representative cases: ID 12, ID 13 and ID 15. It was clear that the sloshing dynamics play a preeminent role in non-isothermal sloshing, with the unstable rotary sloshing instigating a more considerable pressure drop, correlated to a powerful mixing capability (**RQ1**). On the other hand, **RQ2** was qualitatively appraised by exploiting the relaxation time interval. Here the time-dependent system evolution showcased a smaller pressure drop for larger holding periods.

6.2 Future work

The experimental facility developed under this project to characterise non-isothermal sloshing proved to be an excellent initial iteration. Overall, it demonstrated its practical potential of being employed in the 80th ESA parabolic flight. Its operational behaviour and performance were duly characterised, and major modifications were identified to improve and reach the desired scientific/experimental outcomes. Consequently, the following considerations can be made on the design of the small-scale experimental setup:

1. In the **pressurant reservoir**, a valve should be added at the outlet, maximising the vapour volume which remains within this tank and increasing the facility redundancy. A second valve could be placed at the tank's bottom, connected to a pipeline, allowing to empty it from below to an external container, enhancing the setup readiness between experiments. Additionally, a visualisation window or a fill level sensor must be combined to keep track of the liquid mass/volume within the reservoir. Lastly, a considerable problem arose throughout the experiments due to the reservoir's wall temperature. When the desired vapour condition was overshot, gaskets and rubber pipes would melt, introducing residuals to the liquid and forcing an experiment restart. Hereupon, this problem must be solved ahead of the next setup iteration;

2. The **pressurant line's** preeminent considerations rely on the heat losses and increasing the experimental repeatability through a new combination of valves. Therefore, the aluminium pipeline could be replaced by a copper pipeline, to which a heat-

ing coil would be wrapped. Such a setup would minimise the pressurant vapour energy losses during pressurisation by ensuring a steady pipe's temperature correspondent to the reservoir's saturation pressure. Moreover, a mass flow controller could be added upstream of the main pressurisation valve, which must be replaced by a solenoid valve. This would allow to autonomously and remotely control the pressurant flow. Lastly, increasing the number of thermocouples along the line is crucial, specifically at the reservoir outlet, valves and sloshing cell inlet;

3. The **sloshing cell** flat bottom shape must be modified for a concave bottom. Moreover, an emptying port and control valve should be placed at the base and duly connected to an external container. Critically, a second heating coil must be wrapped along the cell's ullage walls to minimise the vapour heat losses and achieve the desired thermal stratification at the interface. Such would allow the employment of ambient conditions liquid, avoiding the burden of cooling it through a freezer. Finally, retrieving the thermal evolution within the tank is a vital factor, to which a new cover must be manufactured and an electrical feedthrough connector used. Such setup has proven its tightness in pressurised vessels, so it is expected to solve this facility issue;

4. The **overall setup** must be modified by placing both the pressurant reservoir and sloshing cell in the same bosch profile base. This would increase the facility's portability and compactness. Additionally, the vacuum and filling ports should be separated by a T-connector, minimising the experimental time and operational hardship.

From the experimental campaign, several intriguing results arose, from which two hypotheses were developed and must be further investigated to pinpoint the baseline phenomena clearly. First, it was identified from the camera footage of the planar sloshing regime ($A_f/R = 0.025$, $\omega/\omega_{11} = 0.893$) that this stable motion was disrupted, leading to a characteristic pressure drop with inherent oscillations. Here, the analysis led to the conclusion that such disruption was created by the impingement of condensation droplets at the free surface, which were falling from the pressurant line. As droplets impinge the interface, instabilities develop, enhancing the sloshing regime energy, which would transition to a chaotic motion. Hereupon, this phenomenon of controlling the sloshing regime by means of droplets must be further assessed, by performing isothermal tests. Secondly, it was theorised that the pressure build-up visible in a chaotic sloshing regime was instigated by a wave characterised as a thin film capable of wetting the ullage walls. Such

wetted areas would easily evaporate, increasing the cell pressure. Therefore, this wetting phenomenon's impact on non-isothermal sloshing must be further studied through temperature control within the cell.

Broadly speaking, once this experimental setup is modified to enable the complete characterisation of the pressurised vessel thermodynamic evolution under sloshing conditions, the most obvious step is to perform cryogenic experiments in the cryostat resorting to LN_2. As proven by the scaling analysis for gravity-dominated non-isothermal sloshing, such apparatus would yield a slight improvement in the matching, allowing to better upscale the experimental results to a representative full-size tank for space applications.

Bibliography

[1] "Sputnik 1 (ps-1 #1)," accessed: 2022-08-25. [Online]. Available: https://space.skyrocket.de/doc_sdat/sputnik-1.htm

[2] G. P. Sutton and O. Biblarz, *Rocket Propulsion Elements*, 9th ed. J. Wiley & Sons, 2017.

[3] T. Himeno, D. Sugimori, K. Ishikawa, Y. Umemura, S. Uzawa, C. Inoue, T. Watanabe, S. Nonaka, Y. Naruo, Y. Inatani, K. Kinefuchi, R. Yamashiro, T. Morito, and K. Okita, "Heat exchange and pressure drop enhanced by sloshing," *47th AIAA/ASME/SAE/ASEE Joint Propulsion Conference and Exhibit 2011*, 07 2011.

[4] B. Dunbar, "Cryogenic fluid management," accessed: 2022-07-25. [Online]. Available: https://www.nasa.gov/centers/ames/research/technology-onepagers/cryogenic-fluid-management.html

[5] J. Rainbow, "Ariane 6 launch debut pushed into 2023," Jun 2022, accessed: 2022-06-20. [Online]. Available: https://spacenews.com/ariane-6-launch-debut-pushed-into-2023/

[6] "Ariane 6," accessed: 2022-06-18. [Online]. Available: https://www.esa.int/Enabling_Support/Space_Transportation/Launch_vehicles/Ariane_6

[7] "Ariane 6 caractéristiques techniques," accessed: 2022-06-18. [Online]. Available: https://ariane6.cnes.fr/fr/ariane-6/en-detail/caracteristiques-techniques

[8] Arianespace, "Ariane 6 user's manual issue 2 revision 0," 2021, accessed: 2022-06-19. [Online]. Available: https://www.arianespace.com/wp-content/uploads/2021/03/Mua-6_Issue-2_Revision-0_March-2021.pdf

[9] S. J. Isakowitz, J. P. Hopkins, and J. B. Hopkins, *International Reference Guide to Space Launch Systems*. American Institute of Aeronautics and Astronautics, 2004.

[10] J. Holt and T. Monk, "Propellant mass fraction calculation methodology for launch vehicles and application to ares vehicles," *AIAA SPACE 2009 Conference & Exposition*, 2009.

[11] H. N. Abramson, *The dynamic behavior of liquids in moving containers, with applications to Space Vehicle Technology*. Scientific and Technical Information Division, National Aeronautics and Space Administration, 1966.

[12] M. Dreyer, "Propellant behavior in launcher tanks: an overview of the compere program," *EUCASS Proceedings Series*, vol. 1, pp. 253–266, 09 2009.

[13] C. Ludwig, *Analysis of cryogenic propellant tank pressurization based upon experiments and numerical simulations*. Cuvillier Verlag, 2014.

[14] T. Arndt, *Sloshing of cryogenic liquids in a cylindrical tank under normal gravity conditions*, 1st ed. Cuvillier Verlag, 2012.

[15] P. Behruzi, M. Michaelis, and G. Khimeche, "Behavior of the cryogenic propellant tanks during the first flight of the ariane 5 esc-a upper stage," *42nd AIAA/ASME/SAE/ASEE Joint Propulsion Conference and Exhibit*, 2006.

[16] A. v. Foreest, *Modeling of cryogenic sloshing including heat and Mass Transfer*, 1st ed. Cuvillier Verlag, 2014.

[17] C. Montsarrat, "Fluid motion analysis in the cryogenic tanks of the upper stage of ariane 5 during the ascent phase," Master's thesis, KTH, School of Engineering Sciences (SCI), Aeronautical and Vehicle Engineering, Aerodynamics, 2017.

[18] D. A. Heald, "some development problems with large cryogenic propellant systems," *SAE Technical Paper Series*, 1960.

[19] J. Lacapere, B. Vieille, and B. Legrand, "Experimental and numerical results of sloshing with cryogenic fluids," *Progress in Propulsion Physics*, 2009.

[20] S. Das and E. Hopfinger, "Mass transfer enhancement by gravity waves at a liquid–vapour interface," *International Journal of Heat and Mass Transfer*, vol. 52, no. 5-6, p. 1400–1411, 2009.

[21] "Parabolic flights," accessed: 2022-06-18. [Online]. Available: https://www.esa.int/Science_Exploration/Human_and_Robotic_Exploration/Research/Parabolic_flights

[22] R. A. Ibrahim, *Liquid Sloshing Dynamics: Theory and Applications*, 1st ed. Cambridge University Press, 2005.

[23] T. A. Lance, “Analysis of propellant slosh dynamics and generation of an equivalent mechanical model for use in preliminary voyager autopilot design studies,” NASA, Tech. Rep., 1966.

[24] F. T. Dodge, *The new ”dynamic behavior of liquids in moving containers”.* South-west Research Inst., 2000.

[25] A. Royon-Lebeaud, E. J. Hopfinger, and A. Cartellier, “Liquid sloshing and wave breaking in circular and square-base cylindrical containers,” *Journal of Fluid Mechanics*, vol. 577, p. 467–494, 2007.

[26] M. E. Moran, N. B. McNelis, and M. T. Kudlac, “Experimental results of hydrogen sloshing a 62 cubic foot (1750 liter) tank,” *30th Joint Propulsion Conference and Exhibit*, 1994.

[27] C. Ludwig, M. Dreyer, and E. Hopfinger, “Pressure variations in a cryogenic liquid storage tank subjected to periodic excitations,” *International Journal of Heat and Mass Transfer*, vol. 66, p. 223–234, 2013.

[28] A. Van Foreest, “Modeling of cryogenic sloshing including heat and mass transfer,” *46th AIAA/ASME/SAE/ASEE Joint Propulsion Conference and Exhibit*, 2010.

[29] C. Ludwig and M. Dreyer, “Analyses of cryogenic propellant tank pressurization based upon ground experiments,” *AIAA SPACE 2012 Conference and Exposition*, 2012.

[30] T. Arndt and M. Dreyer, “Damping behavior of sloshing liquid in laterally excited cylindrical propellant vessels,” *Journal of Spacecraft and Rockets*, vol. 45, no. 5, p. 1085–1088, 2008.

[31] M. Konopka, P. Noeding, J. Klatte, P. Behruzi, J. Gerstmann, A. Stark, and N. Darkow, “Analysis of ln2 filling, draining, stratification and sloshing experiments,” *46th AIAA Fluid Dynamics Conference*, 2016.

[32] A. Simonini, D. Fontanarosa, M. De Giorgi, and M. Vetrano, “Mode characterization and damping measurement of liquid sloshing in cylindrical containers by means of reference image topography,” *Experimental Thermal and Fluid Science*, vol. 120, p. 110232, 2021.

[33] J. W. Miles, “Resonantly forced surface waves in a circular cylinder,” *Journal of Fluid Mechanics*, vol. 149, no. -1, p. 15, 1984.

[34] P. A. Marques, "Experimental characterization and modeling of non-isothermal sloshing," Master's thesis, von Karman Institute for Fluid Dynamics, 2021.

[35] E. J. Hopfinger and V. Baumbach, "Liquid sloshing in cylindrical fuel tanks," *Progress in Propulsion Physics*, 2009.

[36] D. Kirk, J. Oliveira, and P. Schallhorn, "Cryogenic propellant stratification in a rotating and reduced gravity environment," *45th AIAA Aerospace Sciences Meeting and Exhibit*, 2007.

[37] Y. A. Cengel, *Heat transfer: A practical approach*, 2nd ed. McGraw-Hill, 2003.

[38] F. P. Incropera, D. P. Dewitt, T. L. Bergman, and A. S. Lavine, *Fundamentals of heat and mass transfer*, 6th ed. J. Wiley & Sons, 2007.

[39] M. J. Moran, H. N. Shapiro, D. D. Boettner, and M. B. Bailey, *Fundamentals of Engineering Thermodynamics*, 8th ed. John Wiley & Sons, 2014.

[40] S. Velasco, F. L. Román, and J. A. White, "On the clausius–clapeyron vapor pressure equation," *Journal of Chemical Education*, vol. 86, no. 1, p. 106, 2009.

[41] Y. Akkus, A. T. Gurer, and K. Bellur, "Drifting mass accommodation coefficients: In situ measurements from a steady state molecular dynamics setup," *Nanoscale and Microscale Thermophysical Engineering*, vol. 25, no. 1, p. 25–45, 2020.

[42] J. H. Agui and J. P. Moder, "Modeling of non-isothermal cryogenic fluid sloshing," *51st AIAA/SAE/ASEE Joint Propulsion Conference*, 2015.

[43] M. Ruzicka, "On dimensionless numbers," *Chemical Engineering Research and Design*, vol. 86, no. 8, p. 835–868, 2008.

[44] F. M. White, *Fluid mechanics*, 4th ed. McGraw-Hill, 1999.

[45] V. D. Brederode, *Fundamentos de Aerodinâmica incompressível*, 1st ed. IST Press, 2014.

[46] K. Masatsuka, *I do like CFD*. K. Masatsuka, 2013.

[47] M. V. Papalexandris, "On the applicability of stokes' hypothesis to low-mach-number flows," *Continuum Mechanics and Thermodynamics*, vol. 32, no. 4, p. 1245–1249, 2019.

[48] G. Carbajal, C. B. Sobhan, and G. P. Peterson, "Dimensionless governing equations for vapor and liquid flow analysis of heat pipes," *Journal of Thermophysics and Heat Transfer*, vol. 20, no. 1, p. 140–144, 2006.

[49] A. Faghri and Y. Zhang, *Transport phenomena in multiphase systems*, 1st ed. Elsevier Academic Press, 2010.

[50] M. E. Dreyer, *Free surface flows under compensated gravity conditions*. Springer, 2007.

[51] B. Weigand and V. Simon, "Laws of similarity in fluid mechanics," *Flow Phenomena in Nature Volume 1*, p. 20–35, 2006.

[52] T. S. Taylor, *Introduction to rocket science and engineering*, 2nd ed. CRC Press, Taylor & Francis Group, 2017.

[53] J. A. Merino, A. Patzelt, A. Steinacher, M. Windisch, G. Heinrich, R. Forster, and C. Bauer, "Ariane 6 – tanks & structures for the new european launcher," *Deutscher Luft- und Raumfahrtkongress*, 2017.

[54] P. A. Marques, "Scaling and numerical analysis of non-isothermal sloshing for space propulsion," Master's thesis, Instituto Superior Técnico, 2020.

[55] J. Jang, "Mechanical slosh models for rocket-propelled spacecrafts," *AIAA Guidance, Navigation, and Control (GNC) Conference*, 2013.

[56] "Materials database - thermal properties," Oct 2022, accessed: 2022-10-18. [Online]. Available: https://thermtest.com/thermal-resources/materials-database

[57] I. E. Idelchik, *Handbook of Hydraulic Resistance*. Hemisphere, 1986.

[58] H. Ramos, "Cfd for hydrodynamic efficiency and design optimization of key elements of shp," *International Journal of Energy and Environment*, vol. 1, 11 2010.

[59] I. H. Bell, J. Wronski, S. Quoilin, and V. Lemort, "Pure and pseudo-pure fluid thermophysical property evaluation and the open-source thermophysical property library coolprop," *Industrial & Engineering Chemistry Research*, vol. 53, no. 6, pp. 2498–2508, 2014.

[60] "Refprop - nist reference fluid thermodynamic and transport properties database," Aug 2022, accessed: 2022-07-14. [Online]. Available: https://www.nist.gov/srd/refprop

[61] "cdaq-9174 specifications," accessed: 2022-09-14. [Online]. Available: https://www.ni.com/docs/en-US/bundle/cdaq-9174-specs/page/specs.html

[62] "Identifying transducer diaphragms - validyne engineering," Mar 2021, accessed: 2022-09-16. [Online]. Available: https://www.validyne.com/blog/tech-brief-identifying-transducer-diaphragms/

[63] "Cd15 general purpose basic carrier demodulator," May 2019, accessed: 2022-09-14. [Online]. Available: https://www.validyne.com/product/cd15_general_purpose_basic_carrier_demodulator/

[64] "Mineral insulated thermocouples," accessed: 2022-09-12. [Online]. Available: https://www.tc.co.uk/downloads/Mineral-Insulated-Thermocouples-Type-12.pdf

[65] "Ni-9211," accessed: 2022-09-16. [Online]. Available: https://www.ni.com/pt-pt/support/model.ni-9211.html

[66] "Ni-9213," accessed: 2022-09-16. [Online]. Available: https://www.ni.com/pt-pt/support/model.ni-9213.html

[67] "Spark series sp-12000m-cxp4 high performance cmos 12-megapixel camera," accessed: 2022-09-22. [Online]. Available: https://www.jai.com/products/sp-12000m-cxp4

[68] NorPix, "Streampix high speed digital video recording software," accessed: 2022-09-16. [Online]. Available: https://www.norpix.com/products/streampix/streampix.php

[69] A. Simonini, M. R. Vetrano, L. Peveroni, and P. Colinet, "Cryogenic sloshing investigation by means of non-intrusive measurement techniques," *18th International Symposium on the Application of Laser and Imaging Techniques to Fluid Mechanics*, 2016.

[70] W. Thielicke and R. Sonntag, "Particle image velocimetry for matlab: Accuracy and enhanced algorithms in pivlab," *Journal of Open Research Software*, vol. 9, 05 2021.

[71] "Cds catalog," Dec 2020. [Online]. Available: https://www.minco.com/catalog/?catalogpage=product&cid=3_1-polyimide-thermofoil-heaters&id=HK6907

[72] "Pid330 pid temperature controllers." [Online]. Available: https://www.tempatron.co.uk/product.php/31/PID330%20PID%20Temperature%20Controllers.html

[73] "72-8700a - power supply," accessed: 2022-09-22. [Online]. Available: https://www.newark.com/tenma/72-8700a/power-supply-2ch-32v-5a-adj-fixed/dp/47X1651

[74] A. Simonini, L. Peveroni, J.-B. Gouriet, and J.-M. Buchlin, "Quantitative characterization of microgravity sloshing: rising wave in water and hfe 7200," *Two-Phase Systems for Space and Ground Applications*, 10 2018.

[75] M. Rausch, L. Kretschmer, S. Will, A. Leipertz, and A. Fröba, "Density, surface tension, and kinematic viscosity of hydrofluoroethers hfe-7000, hfe-7100, hfe-7200, hfe-7300, and hfe-7500," *Journal of Chemical & Engineering Data*, vol. 60, 11 2015.

[76] P. Warrier and A. Teja, "Density, viscosity, and thermal conductivity of mixtures of 1-ethoxy-1,1,2,2,3,3,4,4,4-nonafluorobutane (hfe 7200) with methanol and 1-ethoxybutane," *Journal of Chemical & Engineering Data*, vol. 56, p. 4291–4294, 11 2011.